Characterisation of Block Cave Mining Secondary Fragmentation

by

Yubo Liu

B.Eng, China University of Mining and Technology, 2013

A THESIS SUBMITTED IN PARTIAL FULFILLMENT OF

THE REQUIREMENTS FOR THE DEGREE OF

MASTER OF APPLIED SCIENCE

in

THE FACULTY OF GRADUATE AND POSTDOCTORAL STUDIES

(Mining Engineering)

THE UNIVERSITY OF BRITISH COLUMBIA

(Vancouver)

July, 2016

Abstract

Block cave mining is a widely employed mining method around the world due to its low operating cost. One of the key factors that affects block caving mine's productivity is fragmentation; accordingly, significant efforts have been made and are currently being made to study fragmentation processes, including the use of numerical modelling and remote sensing techniques. It is desirable to develop fragmentation models that could be used to provide reliable estimates of the range and distribution of the sizes of the rock blocks expected to be induced by caving. In the context of block and panel cave mining, fragmentation processes are characterised as:

i) In-situ (natural) Fragmentation: in-situ blocks that are naturally present within the rock mass before any mining activity takes place. They are defined by the pre-existing discontinuities.

ii) Primary Fragmentation: blocks that separates from the cave back as the undercut is mined and caving is initiated.

iii) Secondary Fragmentation: fragmentation that occurs as the blocks move down through the ore column to the drawpoints.

The main goal of this thesis is to attempt to establish a relationship between in-situ fragmentation and secondary fragmentation. This is achieved by:

i) Measuring secondary fragmentation observed at the drawpoints. Digital image processing is employed in this process, using WipFrag (WipWare, 2014) and PortaMetrics (MotionMetrics, 2015).

ii) Using Discrete Fracture Networks (DFN) to generate in-situ fragmentation curves based on data mapped from boreholes and drifts. The code FracMan (Golder, 2014) is used to generate the DFN model and the fragmentation curves. Additionally, the height of draw

data from code PCBC (Systems, 2015) is used to establish a relationship between modelled in-situ fragmentation and measured secondary fragmentation.

iii) This research is considered to benefit the assessment of block caving fragmentation specifically the estimate of oversizes (hang-ups) at draw columns. Also as a part of the on-going project Cave-to-Mill (Nadolski, et al., 2015) conducted at UBC Mining, this research will feed into the further analysis of Cave - to - Mill study.

Preface

The case study used in this thesis is the New Afton mine located near Kamloops. B.C., Canada. Three visits were made to the mine, in particular: i) during the first site visit, The author was responsible for evaluating data received from the New Afton mine and communicate with engineers working on site regarding data questions; ii) during the second visit responsibility was assumed for introducing the use of a DFN approach to characterise in-situ fragmentation; and iii) a third and final visit was dedicated to sampling and supplementary data collection (e.g. capturing images of underground drawpoints using a PortaMetrics tablet). The material presented in Section 2.2 of this thesis was published in 2014 in the Proceedings of the 1st Discrete Fracture Network Engineering Conference (Vancouver, Canada) - Liu, Y., Elmo, D. and Rogers, S. "*Principles of discrete fracture network modelling for geotechnical applications*". The material introduced in Chapter 3 was published in 2015 in the Proceedings of the 49th US Rock Mechanics/Geomechanics Symposium (San Francisco, U.S.) – Liu, Y., Nadolski, S., Elmo, D., Klein, B. and Scoble, M. "*Use of digital image processing techniques to characterise block caving secondary fragmentation and implications for a proposed Cave-to-Mill approach*". Additionally, I have collaborated in the following publication: Nadolski, S., Klein, B., Elmo, D., Scoble, M., Liu, Y. and Scholar, J. "*Investigation into the Implementation of Sensor-based Ore Sorting Systems at a Block Caving Operation"*, to be published in 2016 in the proceedings of the 7th International Conference & Exhibition on Mass Mining, Sydney, Australia.

All the results presented in this thesis are preliminary only. Further statements are required to confirm and solidate the findings. The current results should not be used for design purposes.

Table of contents

List of tables

List of figures

Acknowledgements

Thanks to my parents, they always provide supports to me, moreover, they patiently encourage me when I face barriers.

Thanks particularly to my supervisor Dr. Davide Elmo; he provided me the opportunity to come to Canada to study. During my research, Prof. Elmo had guided me in my studies and provided help whenever possible.

Also thanks to my other committee members: Dr. Malcolm Scoble and Dr. Marek Pawlik, and my colleague, Stefan Nadolski for our interesting discussions about the project and for valuable suggestions that I believe helped me in my research.

Thanks to all my friends, who made my life in Vancouver colourful, the time I spent in UBC will be a great treasure to my future career exploration.

This research was funded by the National Science and Engineering Research Council of Canada, as part of the NSERC Discovery and NSERC CRD 453374-13 held by Dr. Davide Elmo. I would also like to acknowledge SRK Consulting for providing me with the SRK 2015 Canadian Scholarship. In-kind support was provide by i) Golder Associates Ltd. in the form of a free academic license for the DFN code FracMan; ii) MotionMetrics International Corp who provided the PortaMetrics imaging processing tablet and iii) Rocscience Inc. who provided a free copy of their software package (including Dips 7.0, Examine 3D, RocData, Slide, Swedge and Unwedge)

Chapter 1: Outline

In the last decade open-pit mines have been reaching depths that involve significant costs and stability concerns. For these reasons underground mass mining methods are now considered as alternative solutions for the exploitation at depth of low grade ore deposits. Block and panel caving are cost effective underground mining techniques that relies on gravity induced failure to extract the ore. Cave mining has the potential to yield extraction rates on a scale comparable to open pit mining (i.e. in excess of 100,000 tpd). Currently, feasibility and development studies for block and panel cave mines rely on a mix of empirical and numerical approaches. Neither approaches can alone provide a unique answer to one of the most critical elements in pre caving assessment process, which is the determination of the likely distribution of rock mass fragmentation.

This research aims at characterising the relationship between in-situ and secondary fragmentation for an existing cave mine (the New Afton mine, Kamloops, B.C.). Because it is not possible to directly measure the progressive fragmentation processes that result in the fragmented ore that reports at the drawpoints, the objective of this study is to link field observations and measurements of secondary fragmentation to numerical analysis of in-situ fragmentation. Based on the estimated production schedule, rate of draw, and estimated height of draw (HOD), the concept is to trace where within the rock mass the fragmented ore has originated, and relate the observed distribution size to the estimated in-situ blockiness character of the rock mass prior to caving. To achieve this, it is proposed to firstly derive rock size distribution at drawpoints using digital image processing tools and then build a Discrete Fracture Networks (DFN) model to estimate in-situ fragmentation to simulate the region that secondary fragmentation is original from. The scheduling software PCBC (Systems, 2015) is used to trace back the location within the ore column where the materials

observed at the drawpoints has originated from. Note that this approach assumes that the caved material would not be subjected to reeling, i.e. the flow would occur vertically down through the drawpoints.

1.1 The New Afton block caving mine

The New Afton mine is a block caving mine located 10 km west of Kamloops, B.C., Canada. The main deposits of New Afton are copper and gold. Approximately 13,000 tonnes are extracted every day, which makes New Afton a relatively small cave operation in comparison to the existing major cave mines (50,000 tonnes/day) and proposed super caves (>>100,000 tonnes/day). The annual production of the New Afton mine is 85,000 ounces of gold and 75 million pounds of copper.

1.1.1 The New Afton mine geology introduction

The rocks in the New Afton mine are mainly Late Triassic to Early Jurassic Nicola Group island-arc sedimentary rocks and volcanic assemblages and associated intrusive rocks of the Iron Mask batholith. The mining area is controlled by regional-scale fault zones, which are also considered to influence the mineralisation processes. In particular, the east to northeast oriented fault zones are mainly controls for mineralisation.

The deposit of the New Afton mine is mainly porphyry-style. And the deposit is mainly broken into three zones, West Cave, East Cave and C Zone, this research mainly considers West Cave Zone.

1.2 Research background

One of the principal concerns for block cave mining is fragmentation. Block cave fragmentation can be affected by a variety of factors, including joint spacing, joints length, draw schedule, drawpoint design, cave propagation. Accordingly, fragmentation inevitably becomes a variable within the scheme of caving processes, and it is generally not possible to determine the size of the blocks that will be produced as the cave is initiated and propagates upwards. One of the main problems that may occur is hang-ups, which are due to relatively large rock blocks becoming stuck in the drawpoints, thus preventing regular mucking and draw of material. The consequences of hang-ups are not just related to the interruption of the normal production schedule and financial costs, but also a significant impact on the overall flow of the fragmented ore material inducing inhomogeneous draw of the ore column. In this context, the study of fragmentation processes becomes extremely important to the knowledge of block caving productivity.

1.3 Methodology

The research has focused on exploring the relationship between in-situ fragmentation and secondary fragmentation in the context of cave mining methods. The aim was to provide recommendations that could be useful to assist with the estimation of the likely secondary fragmentation size based on an initial estimate of in-situ fragmentation. A Discrete Fracture Network (DFN) approach is used to generate a 3D structural model for the West Cave at the New Afton mine and derive size distribution curves representing in-situ fragmentation for a range of fracture intensity. Secondary fragmentation was measured using digital image processing techniques (WipFrag and PortaMetrics, See Chapter 3). Because it is not possible to track the path that the ore material follows as it moves within the ore column, it becomes extremely difficult to

link the material reporting at the drawpoint to its original location within the in-situ rock mass. In this thesis the relationship between in situ fragmentation and secondary fragmentation measured for a given drawpoint is estimated using the height of drawn (HOD) data resulting from the mine schedule provide by the New Afton mine.

1.4 Thesis structure

This thesis includes 6 chapters, and it is organised as follows:

- Chapter 1 – It serves as introduction to the thesis.
- Chapter 2 – It provides a review of block cave mining, numerical modelling approach, Discrete Fracture Networks and techniques used in mining to measure fragmentation.
- Chapter 3 – It describes the work carried out to measure secondary fragmentation in the field at the New Afton mine.
- Chapter 4 – Reports on in-situ fragmentation modelling using a Discrete Fracture Networks approach.
- Chapter 5 – It describes the process used to link in-situ fragmentation to secondary fragmentation.
- Chapter 6 – Provides a summary of the research and recommendations for future work.

Chapter 2: Literature review

2.1 Introduction to mass mining methods

The last decades have witnessed a high requirement for metal materials throughout the world. As open pit mines are approaching their geotechnical and economical limits, underground mass mining methods are becoming the preferred option to exploit low grade deposits. To date, block caving has been applied to a wide variety of ore-deposits worldwide, Figure 2.1. Block cave mining (Laubscher, Cave mining - the state of the art, 1994) is an underground mining method that is most commonly applied to massive and fractured orebody. In general terms, block cave mining is characterised by caving and extraction of a massive volume of rock which potentially translates into the formation of a surface depression or subsidence zone. The extent of the subsidence zone depends on the characteristics of the mining, the rock mass, and the topography of the ground surface. Figure 2.2 shows an example of a block caving mine (Hamrin, 1982). The actual mine lay-out may differ from that shown in Figure 2.2; for instance, the New Afton mine (Kamloops, BC, Canada) employs an apex level above the undercut to monitor the efficacy of the processes leading to cave initiation.

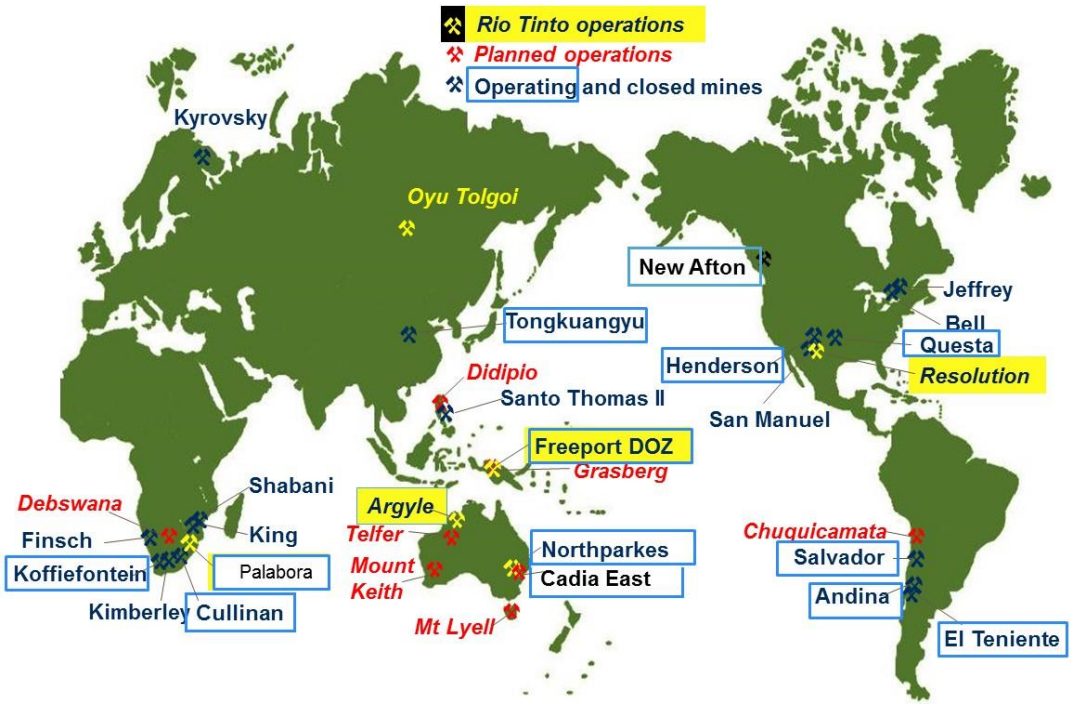

Figure 2.1: Main block caving mines around the world (after Moss, 2016, personal communication)

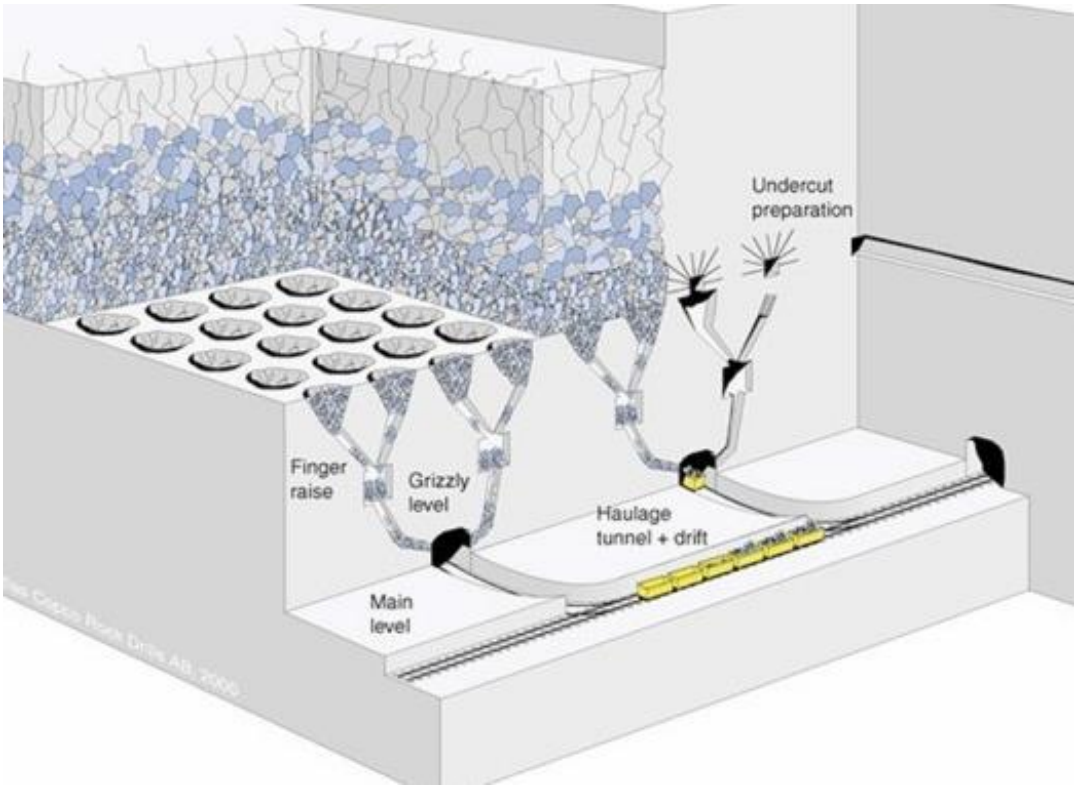

Figure 2.2: Example of a block caving mine (Hamrin, 1982).

2.2 Cave initiation and development

Figure 2.3 shows a schematic diagram of a caving process. Cave is initiated by drilling and blasting an undercut level (either below or within the ore body). Caveability assessment usually involves a predication of the hydraulic radius (area to perimeter ratio of the unsupported area of the cave back) of the undercut at which caving will initiate for a rock mass having given or estimated geotechnical characteristics (Brown, 2003). Several parameters have been found to influence caveability, including discontinuity geometry and strength, rock mass strength, orebody geometry, undercut dimensions and induced stresses. Cavability could be assessed by means of either empirical methods (e.g. Laubscher's caving chart, Laubscher 1990, 1994, 2001) or numerical modelling (e.g. Sainsbury et al., 2008, 2010), which holds the possibility of providing a more fundamental and rigorous assessment of cave initiation and propagation than empirical methods. In particular this approach may have advantages in cases for which current experience is lacking or not well developed.

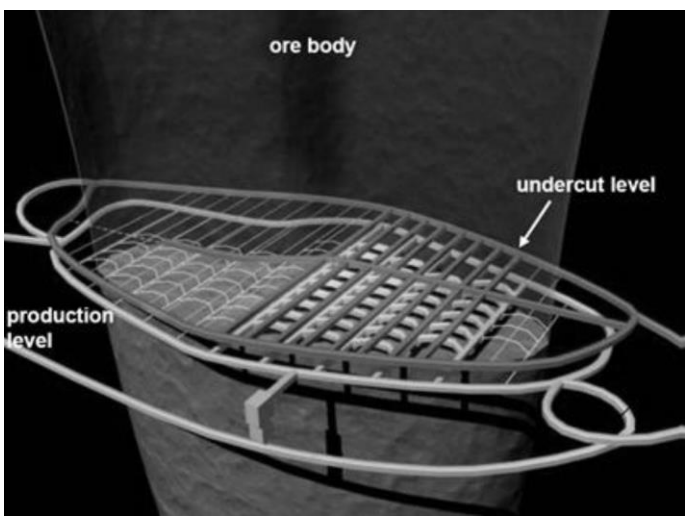

Typical cave mining layout, with two mining levels (production and undercut level) placed within the ore column.

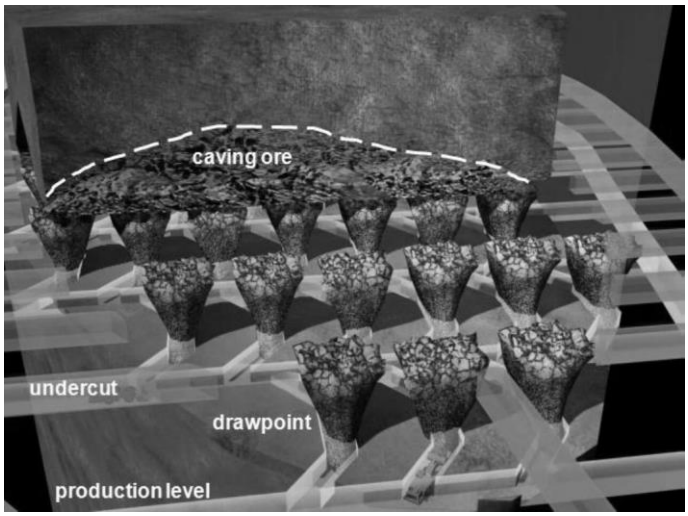

Broken ore falls into the production level through the drawpoints. As the ore is removed, the ore above continues to break and cave in by gravity.

Figure 2.3: Schematic diagram of a block caving process (animation screenshots modified after Sandvik Tamrock Corp). Text modified from Elmo et al. (2014).

Cave Propagation is the process of propagation of an initiated cave by the progressive drawing of broken ore in a planned and controlled manner, which is the ability of the cave to continue to propagate once caving has been initiated (Brown, 2003). Cave propagation depends on a number of factors including the undercut design, the rate of undercutting, the stresses induced on the boundaries and above the cave, the orebody structure and its geotechnical characteristics, and the draw control strategy employed. Because of the capital intensive, non-selective and relatively inflexible nature of caving methods of mining, the inability to initiate or sustain caving is one of the greatest risks faced in cave mining.

2.3 Fragmentation

The fragmentation (Figure 2.4) produced in the orebody during the caving process controls the overall success and profitability of a block caving operation (Brown, 2003).

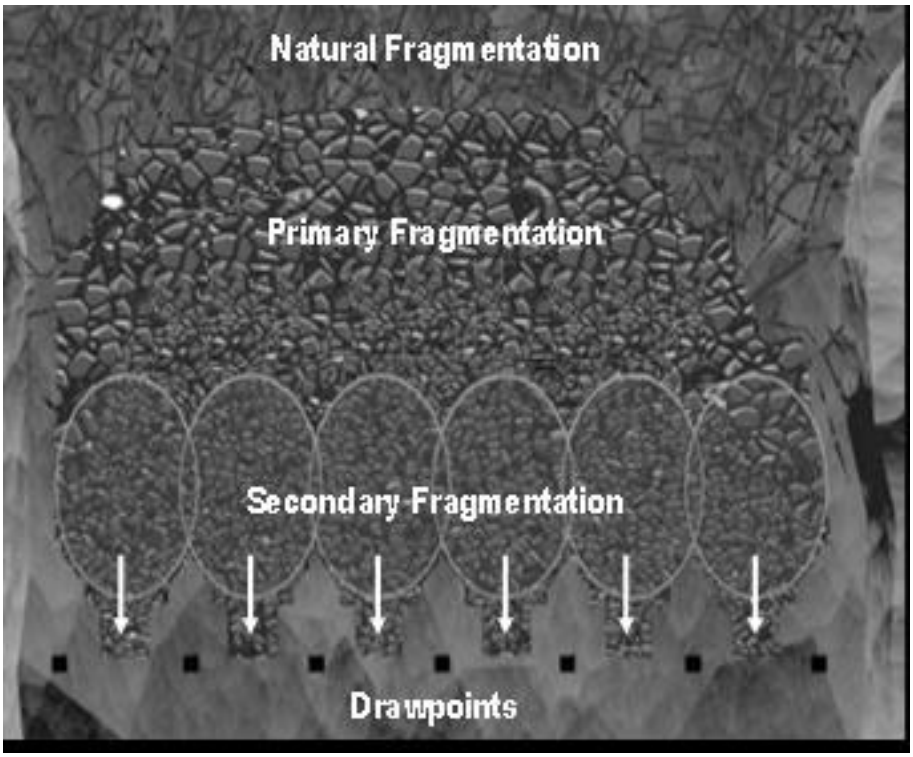

Figure 2.4: Fragmentation during a caving process. Modified from Elmo et al., (2014).

Various parameters are influenced by fragmentation (Laubscher, 1994 and 2000), including drawpoint size and spacing, equipment selection, draw control procedures, production rates and hang-ups and the need for secondary breakage/ blasting. Fragmentation can be characterised in terms of:

- In-situ (or natural) Fragmentation. These are the blocks naturally present within the rock mass be-fore any mining activity takes place. They are defined by pre-existing (open) discontinuities. In situ fragmentation is determined by the network of discontinuities pre-existing in the rock mass. Size and shapes of the in-situ blocks are a direct result of the geometry of the open discontinuities present within the rock mass. Healed discontinuities (e.g. veins) do not form in-situ blocks, but they are still very important as the represent planes of weakness within the rock mass on which separation may occur during primary and secondary stages.

- Primary Fragmentation. Primary fragmentation results from the loading conditions imposed on the rock mass in the vicinity of the cave back. These are the blocks that detach from the cave back as the undercut is mined and caving is initiated, Figure 2.5. Although most failures at this stage can be expected to occur on the existing discontinuities, under high stress or stress caving conditions, fracture of intact rock may also occur.

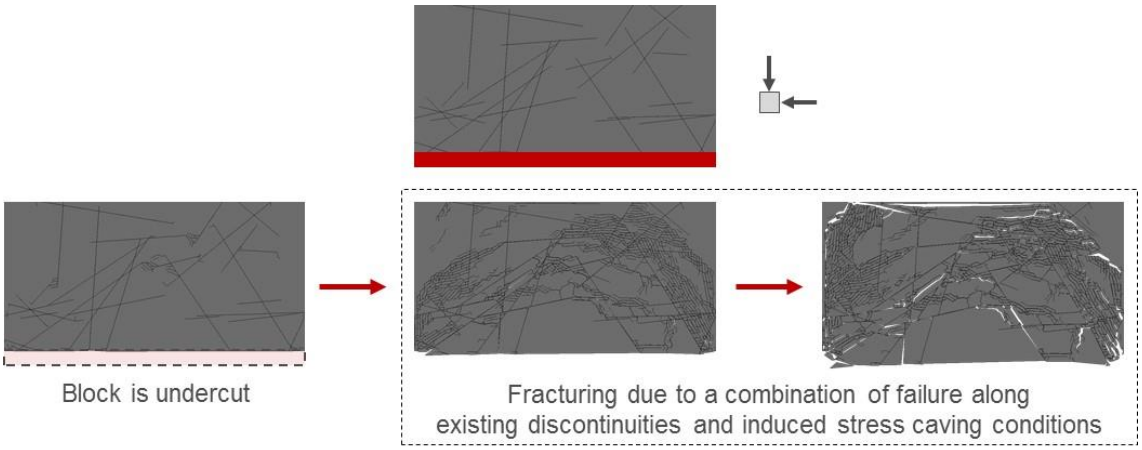

Figure 2.5: Diagram showing primary fragmentation processes, modified from Rogers et al. (2010).

- Secondary Fragmentation (Figure 2.6). These are the blocks that form as primary blocks move down through the ore column to the drawpoints. Secondary fragmentation processes are largely controlled by load breakage, shearing, crushing, and abrasion between rock blocks as they migrate downward into a drawbell, increasing the finer broken ore size distribution with depth.

Figure 2.6: Examples of secondary fragmentation observed at drawpoints (after Brown, 2003).

2.4 Measurement of fragmentation

One of the most critical elements in pre caving assessment process is determining the likely distribution of rock mass fragmentation, with the impact of poor or unexpected fragmentation upon cave operations being significant (Elmo et al, 2014). The process of rock fragmentation during block caving is controlled by the natural fragmentation of the rock mass and the fragmentation processes that take place in the ore column. Natural fragmentation cannot be measured directly, but it can potentially be estimated based on a characterization of the natural fracture network and using DFN models (Elmo et al., 2009; Rogers et al, 2010). Primary fragmentation cannot be measured directly although it may be approximated by measurements made on the broken ore drawn from the drawpoints in the early stages of caving. Secondary fragmentation represents a poorly constrained problem given uncertainties related to block geometry and block-to-block loading conditions. Secondary fragmentation could be measured by means of physical methods (e.g. sieving and boulder counting and image processing techniques). It is reasonable to assume that finer fragment sizes produced following secondary fragmentation would be particularly difficult to measure by methods other than sieving (Brown, 2003). Measurement of fragmentation

related to production blasting provided useful frameworks for the measurement of block caving secondary fragmentation. In this context, the most commonly used approaches for in-situ rock particle size measurement are physical screening and digital image processing. These are described in more detail in the following sections.

2.4.1 Physical screening

Physical screening is a process that involves the separation of rock fragments passing sieves of different sizes. While sieving may be an accurate method to measure fragmentation, it is an impractical method for use for other than the most special purposes, as it causes disruption to production and is also relatively costly (Brown, 2003). A boulder counting techniques (Grant and Dutton, 1983; Bhandari and Tawnar, 1993) could be used to measure the "oversize" fragments. This technique provides a statistically representative measure of the important top size distribution but obviously does not establish the full size distribution. Figure 2.7 shows an example of the fragmentation distribution measured at the Premier Mine, South Africa. (Brown, 2003). The distribution is somewhat irregular and covers a relatively limited range of fragment sizes from 10 m^3 down to about 0.25 m^3.

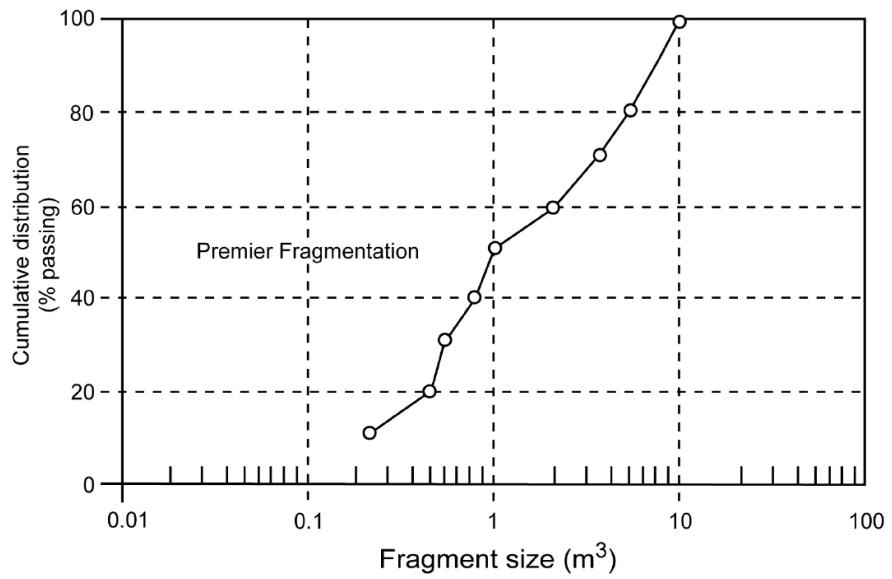

Figure 2.7: Example of the fragmentation distribution measured at the Premier Mine, South Africa. Note that finer sizes of less than about 0.25 m^3 is absent from the distribution. After Brown (2003).

2.4.2 Digital image processing

This method is based on the use of photographs, which are then analysed using computer-based image processing techniques, Figure 2.8. Digital image processing has been developing and applied to blasting measurement since the 1980s. Initial digital image processing techniques include Carlsson and Nyberg (1983) and stereological methods by Hunter et al. (1990). The appearance of automatic edge detection functions has helped to improve the efficiency of digital image processing. Automatic edge detection function is based on analysing pixels at which the brightness changes significantly, i.e. to find the discontinuities of pixels. The biggest challenge of edge detection is to define proper pixel discontinuities, as the problems caused by this issue may lead to inaccurate results.

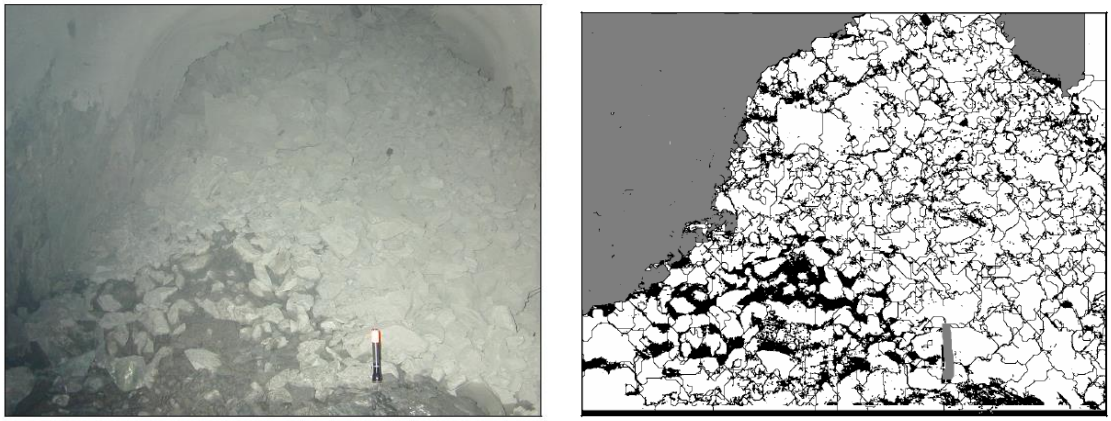

Figure 2.8: Example of digital image processing of secondary fragmentation (modified from Brown, 2003).

Factors that potentially can affect the accuracy of digital image processing include:

- Sampling errors that result from systematic bias in the process of taking an image of the fragmented muck pile: e.g. when camera is pointed at a place in the muck pile where coarse blocks or zones of fines dominate.
- Environment factors such as light and shadow. The change of brightness would define the edge of particles. Uneven lightness and shadow would lead to incorrect edge definitions and result in wrong solutions such as segregation and grouping errors.
- Scale references used for the calculation of particle sizes. Scale references are required to scale particle sizes. For simple cases such as particles are placed flatly on one face and pictures are taken perpendicular to the face of the particles (i.e. rocks fragments have same distances to the camera), one reference is enough to define particle sizes. However, when dealing with a large amount of particles or piled-up particles (i.e. rock fragments have different distances to the camera), multiple references are required.

- Overlapping of rock fragments. As photographic analysis can only capture the visible surface of the rock fragments, all the particles hidden by other fragments would be invisible and they would not be counted towards the final size distribution curve.

Different types of digital image processing software exist, including:

- FRAGSCAN (Schleifer and Tessier, 1996) is an automatic image processing system developed by for assessing fragmentation distributions using images of the visible parts of muck piles.
- WipFrag (Maerz et al., 1996) is an automated image-based granulometry system that uses digital image analysis of photographs and videotape images to determine the size distribution.
- Split (Kemeny et al. 1993) is an image processing program designed to compute the size distribution of rock fragments from grey scale images at various stages of rock breaking in mining and mineral processing.
- PortaMetrics (Motion Metrics Corp., 2016) is a Windows OS based tablets with three external cameras as well as an embedded image analysis code. The three external cameras are able to detect the distance to the muckpile and to define the size of the rock fragments.

Both WipFrag and PortaMetrics were used as part of this research to measure secondary fragmentation at the New Afton mine, further details are given in Chapter 3.

2.5 Introduction to Discrete Fracture Networks[1]

Discrete Fracture Networks (DFN) methods can provide an alternative and effective approach for studying rock mass fragmentation. Rogers et al., (2010 and 2014) used a DFN based approach to simulate in-situ fragmentation and primary fragmentation, while Elmo et al. (2011 and 2014) used DFN integrated with geomechanical models to estimate rock mass property, simulate cave initiation and primary fragmentation.

The DFN method relies on quantifiable field parameters (fracture orientation, intensity, length and terminations). The processed data can be used directly within the same DFN platform (stand alone or direct application) or the fracture network can be exported to a variety of external numerical codes (integrated or indirect application). There also exist numerical codes with embedded limited DFN generation capability, though these codes generally do not offer the same pre-processing and analysis capability as a dedicate DFN platform. The quality of the DFN model depends directly on the quality of the field data, thus is related to factors such as available rock exposures, limits of window/scanline mapping techniques with respect to both trace length biases and effect of cut-off assumptions in the mapping methodology. Fracture size (fracture length) is an important parameter in DFN modelling. However, this parameter is either seldom available at the pre-feasibility stage due to a lack of exposures (man-made or natural), or engineers have access to limited length data collected along exploratory drifts.

[1] This section is based on the paper "Principles of discrete fracture network modelling for geotechnical applications" by Elmo, D. Liu, Y. and Rogers, S. for 1st DFNE 2014.

The International Society of Rock Mechanics (ISRM) guidelines for the quantitative description of discontinuities include most, if not all, of the main parameters required to generate a DFN model. However, there are important differences engineers should be aware of. For instance, the ISRM methods use fracture spacing and frequency (1D sampling), whereas the intensity parameter in the DFN approach could also refer to areal intensity (2D sampling). The fracture radius does not necessarily correspond to fracture persistence or the trace length mapped on an exposed surface. The definition of fracture radius also requires geotechnical engineers to be familiar with truncation and censoring biases (i.e. values below a certain fracture length are omitted - truncation - or relatively larger values cannot be measured because of the limited extent of the rock exposure - censoring). The truncation bias plays also a major role in defining the correct fracture intensity for DFN analysis. Fracture terminations are seldom collected by geotechnical engineers in the field.

The typical process involved in the generation of a DFN model requires the definition of:

- Fracture spatial model
- Fracture intensity
- Fracture orientation
- Fracture size
- Fracture terminations

Validation of the DFN model is achieved by comparing the orientation, intensity and pattern of the simulated fracture traces with those measured in the field. The stochastic nature of the process is such that there are an infinite number of possible realisations of the 3D fracture system based on the mapped data. Indeed, the mapping process is itself random by the nature of how fractures are presented in available windows. With the exception of fully explicit modelling of an individual

fracture or simplified fracture sets, the stochastic approach provides the best option for creating realistic geometric models of fracturing.

2.5.1 Fracture spatial model

The starting point for the generation of a DFN model is the definition of the spatial model that governs the way fractures will be generated within a given 3D volume. The majority of the spatial models involve similar considerations for specific fracture characteristics, such as shape (generally polygons), size and termination at intersections. The main differences lie in the specific distribution laws used to simulate fracture orientation and fracture location (Dershowitz et al., 1998; Staub et al., 2002). The choice of a specific fracture spatial model is typically based on assumptions made from field data and geological observations. Examples of fracture spatial models include a) Enhanced Baecher, b) Nearest-Neighbour and c) Fractal Levy-Lee (Figure 2.9). These are the three spatial models available in the DFN code FracMan (Golder, 2016), which was used in the current study to develop a simple DFN model for the east cave at the New Afton mine.

In the Enhanced Baecher model fracture location may be defined by a regular (deterministic) pattern or a stochastic process. The stochastic approach assumes that the fracture centres are randomly located in space using a Poisson process. The Nearest-Neighbour model is particularly suited to model the tendency of fractures to be clustered around major points and faults by preferentially producing new fractures in proximity of earlier fractures (Dershowitz et al., 1998). The Levy-Lee model is a fractal model whose key features are that fracture centres are created sequentially and the size of a fracture is related to its distance from previous fractures (Staub et al., 2002).

Spatial models can be grouped in stationary and non-stationary models based upon the relationship between different fracture sets. The Enhanced Baecher model is a stationary model, while both the Nearest-Neighbour and the Levy-Lee models are non-stationary models incorporating the option of generating spatial and temporal relations between different set of fractures. Ultimately, the choice of which spatial model to use requires a good knowledge of the structural geological setting of the rock mass under consideration.

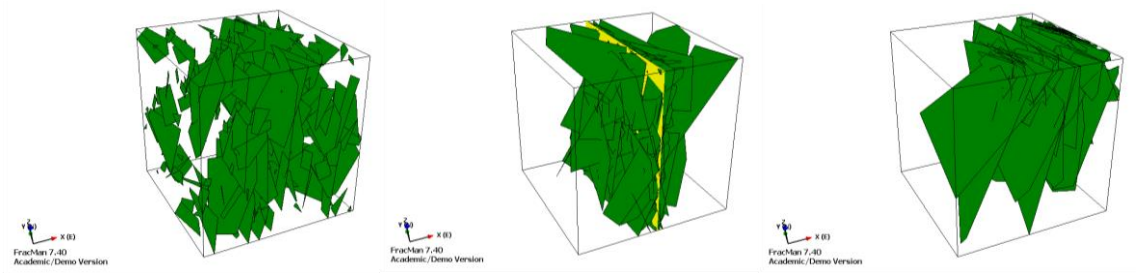

Figure 2.9: Examples of fracture spatial model: Enhanced Baecher (Left). Nearest-Neighbour (Middle). Fractal Levy-Lee (Right).

2.5.2 Fracture intensity

Fracture intensity is generally expressed with reference to a unified system of fracture intensity measures that provide an easy framework to move between differing scales and dimensions (Dershowitz and Herda (1992)). Fracture intensity is referred to as P_{ij} intensity, where the subscript *i* refers to the dimensions of sample, and subscript *j* refers to the dimensions of measurement, Table 2.1.

		Dimension of Measurement (i)				
		0	1	2	3	
Dimension of sample (j)	1	P_{10} No. of fractures per unit length of borehole	P_{11} Length of fractures per unit length			Linear Measures
	2	P_{20} No. of fractures per unit area	P_{21} Length of fractures per unit area	P_{22} Area of fractures per unit area		Areal Measures
	3	P_{30} No. of fractures per unit volume		P_{32} Area of fractures per unit volume	P_{33} Volume of fractures per unit volume	Volumetric Measures
		Density		Intensity	Porosity	

Table 2.1: Fracture intensity P_{ij} system (FracMan manual, Golder, 2016).

Accordingly, the volumetric fracture intensity (P_{32}) is defined as the ratio of total fracture area to unit volume (dimensions of m^2/m^3). P_{32} is an intrinsic rock mass property and whilst it cannot be directly measured, it can be inferred from either 1D or 2D data using a simulated sampling methodology on the basis of a linear correlation (Dershowitz and Herda (1992) with P_{21} (m/m^2), which is the total trace length of fractures per unit area, or with P_{10} (m^{-1}), which represents the total number of fractures along a scanline or borehole (i.e. P_{10} is a measure of fracture frequency).

$$P_{32} = C_{32} P_{21}$$
$$P_{32} = C_{31} P_{10}$$

The constants of proportionality C_{32} and C_{31} depend on the relative orientation of the fractures to the orientation of the sampling panel or scanline/borehole, and the fracture radius distribution. Figure 2.10 shows the process of determining P_{32} by simulation using the equations above. It is important to note that both P_{10} and P_{21} data are heavily influenced by the relative orientation of the predominant fracture sets with respect to the orientation of the boreholes/sampling planes. Furthermore, by definition, the volumetric fracture intensity P_{32} is related to fracture radius, thus truncation biases would play a major role in defining the correct fracture intensity for DFN analysis.

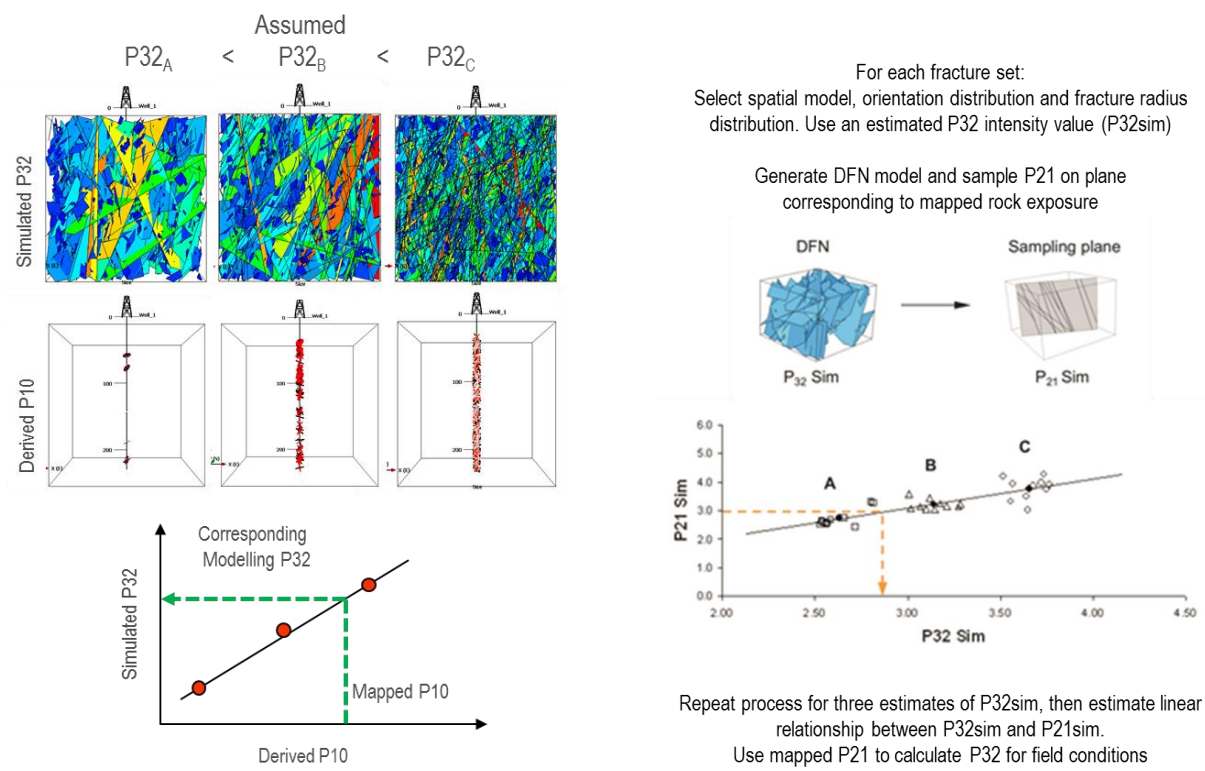

Figure 2.10: General procedure for determining P_{32} using P_{10} (left) or P_{21} (Right)

Alternatively, a DFN model could be generated by conditioning the DFN model to a direct replication of the number of fractures intersected along a scanline/borehole. This process is known as P_{10} conditioning. To account for directional bias, P_{10} intensity properties could be converted to

a non-directional P32 potential property using the method proposed by (Wang, 2005) using stereological relationships between fracture orientation and fracture intensity. The P_{32} potential is independent of scale and orientation, and can therefore be used to directly extrapolate intensities throughout the rock mass volume.

2.5.3 Fracture orientation

DFN models can be generated separately for each fracture set and then combined to obtain the overall representation of the fracture network. The application of separate statistical procedures to define fracture sets and, consequently the separate DFN models for each is known as a disaggregate approach. Distributions such as Fisher, Bingham, bivariate Fisher and bivariate Bingham can be used to represent fracture orientation. Alternatively, field data that do not conform to straight forward statistical methods (i.e. characterised by a highly dispersed scatter), can be analysed using a bootstrap approach, whereby a statistical method based upon multiple random sampling with replacement from an original sample is used to create a pseudo-replicate sample of fracture orientations (Rogers et al., 2009). The orientation distribution for fractures mapped at a given rock exposure or along a borehole depends on the orientation of the sampling geometry relative to the orientation of the fractures, thus mapped data would need to be corrected to account for orientation bias. However, when validating the model, the simulated orientation data would have to be compared to the uncorrected data, since the sampling procedure would automatically introduce an equivalent sampling bias.

2.5.4 Fracture size

The definition of fracture size in the context of DFN modelling requires differentiating between fracture trace length (mapped on rock exposures, also referred to as fracture persistence) and fracture radius, Figure 2.11. Fracture trace length is an explicit measure of the trace that a fracture or fault makes with a geological surface or mining exposure. Fracture radius is the radius of a circle of equivalent area to a polygonal fracture.

Measurements of fracture length can be obtained by mapping 2D rock exposures, using conventional (scanline or window mapping) or remote sensing techniques (e.g. photogrammetry and/or LiDAR). Note that generally remote sensing techniques process fracture length as the diameter of a disc inscribing the mapped feature. It is very important not to confuse the notion of fracture radius used in the DFN model with the apparent radius of the disc inscribing the fracture plane in the processed image or point cloud. Once the distribution of fracture length is known, the distribution of fracture radius can be assessed by analytical methods (Mauldon, 1998; Zhang and Einstein, 1998; Zhang and Einstein, 2000). The process is based on the basic assumptions that: i) fractures are considered to be planar and ii) fractures can be represented by thin polygons with *n* sides (i.e. fracture are assumed to be equidimensional). However, there exists the possibility in some DFN modelling packages to account for not equidimensional fractures. The analytical method is well suited for deriving the distribution of fracture radius using the distribution of trace lengths as the initial input. The method also accounts for censoring bias that may arise when measuring trace lengths in the field. Small scale fractures (joints) and large scale faults could be related according to power laws. The choice of the distribution often depends on the modelling scale. Power laws may better suited to define an overall fracture radius distribution for large scale

DFN models, whether other forms of distributions (e.g. log normal) may apply instead to small scale (e.g. 100m scale) DFN models.

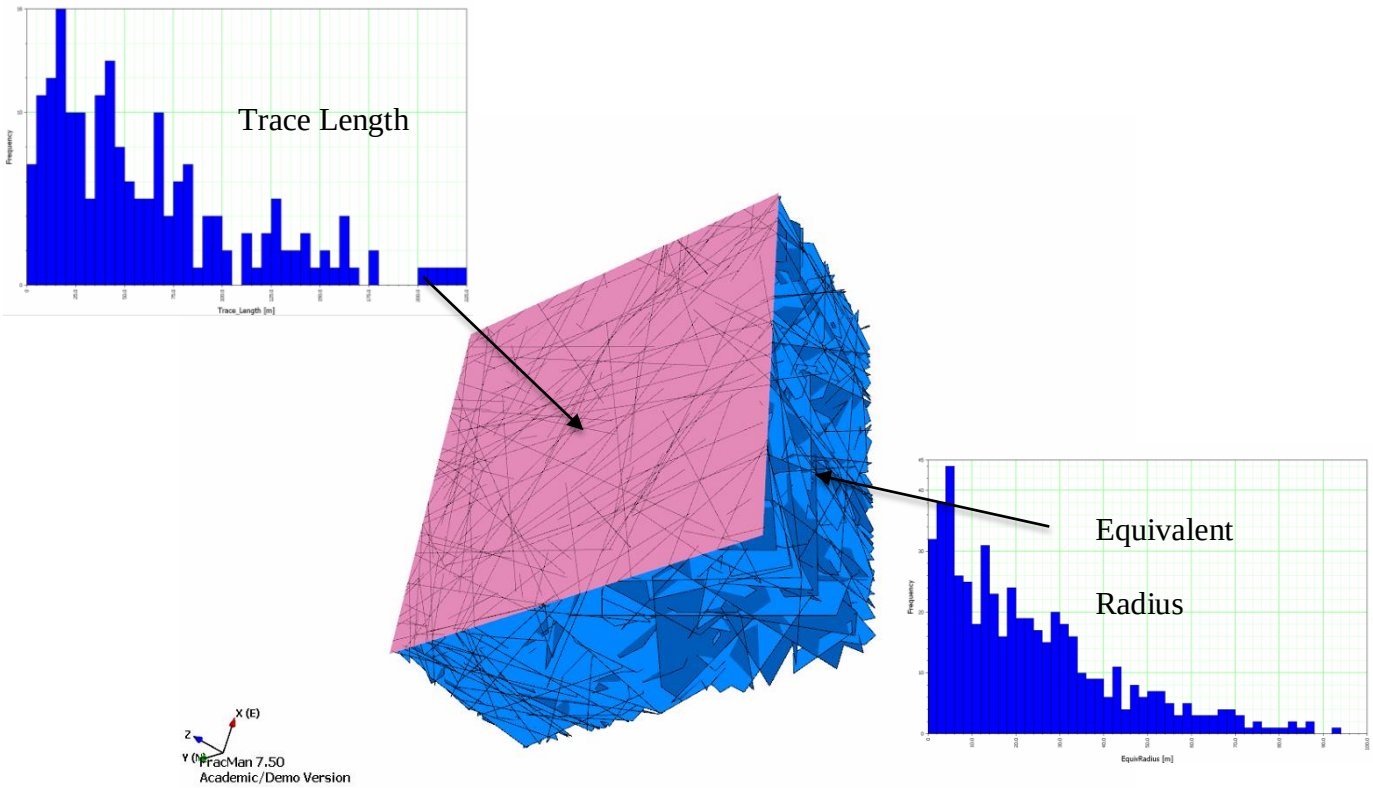

Figure 2.11: Distribution of mapped fracture traces (data source) versus distribution of fracture radius (required DFN input).

2.6 Assessment of primary fragmentation using a DFN method

The code FracMan allows the 3D visualisation of blocks defined by intersecting discontinuities in the DFN model. Two different approaches are available: an implicit fragmentation grid algorithm (Sybil Frac) and a more conventional explicit block search algorithm. Those are described in more details in Elmo et al. (2014), who used the implicit to study block size as a function of the assumed fracture length in the model and provide a preliminary integration between DFN based

fragmentation and rock mass classification systems. Rogers et al. (2007) used the explicit block search in FracMan for characterising the natural fragmentation of a fractured rock mass, while Elmo et al. (2008) used a similar approach combined with a sequential sampling technique for characterising intact rock bridges. Tollenaar (2008) used the explicit block search method to characterise the volume, shape and number formed above an excavation simulating the undercut in a block cave mine.

The implicit fragmentation algorithm is used in this thesis to provide preliminary assessment of natural fragmentation for the West Cave at the New Afton mine. As shown in Figure 2.12, the implicit approach works by initially overlaying a grid of cells onto the initial DFN model, then fractures are mapped onto those cells and stepped blocks are assembled by joining up the connected grid cells (Figure 2.12). Note that the procedure depends on the size of the grid cells, and a grid cell size of approximately 25% of the average fracture spacing should be used to achieve good results.

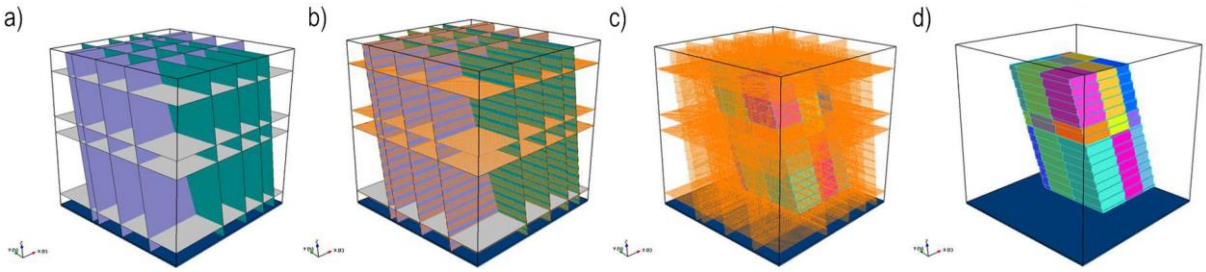

Figure 2.12: FracMan DFN-based cell mapping algorithm: a) Initial DFN, b) fractures being mapped the specified grid, c) blocks being mapped along the grid cells and d) Final block model. Modified from Elmo et al. (2014).

Chapter 3: Digital image processing applied to block caving secondary fragmentation measurement[2]

3.1 Introduction

This chapter discusses the use of two digital image processing tools - WipFrag (WipWare, 2014) and PortaMetrics (MotionMetrics, 2015) - to provide estimates of secondary fragmentation. A preliminary study that compared results obtained from WipFrag and PortaMetrics in a controlled lab environment against physical screening was initially performed to evaluate and compare the two imaging processing techniques. Subsequently, WipFrag and PortaMetrics were used to measure actual secondary fragmentation at underground drawpoints.

3.2 Introduction to WipFrag and PortaMetrics

Digital image processing is used to analyse images of rock fragments and derive size distributions. Digital image processing retains some advantages of over traditional screening, which explains why these techniques are being introduced by the mining companies. Those advantages include: i) the cost required using imaging processing analysis is usually considerably less than the one using physical screening; and ii) moving rock fragments is not required with digital image processing; therefore it has a limited impact on the production schedule.

---

[2] This chapter is based on a paper by Liu, Y et al. published at 2015 ARMA: Paper – 009 Use of digital image processing techniques to characterise block caving secondary fragmentation and implications for a proposed Cave-to-Mill approach.

3.2.1 WipFrag

WipFrag is one of the most employed digital image processing software (Han & Song, 2016) (Ko & Shang, 2011). Figure 3.1 shows an example of a drawpoint photo and the corresponding WipFrag solution (manual processing) and generated PSD result. WipFrag measures the profile area of fragments using a geometric probability (Maerz N. H., 1998) and reconstructs three - dimensional distributions (Maerz N. H., 1996). In WipFrag, an individual rock's size refers to the equivalent diameter of the measured rock's area that appears in the image.

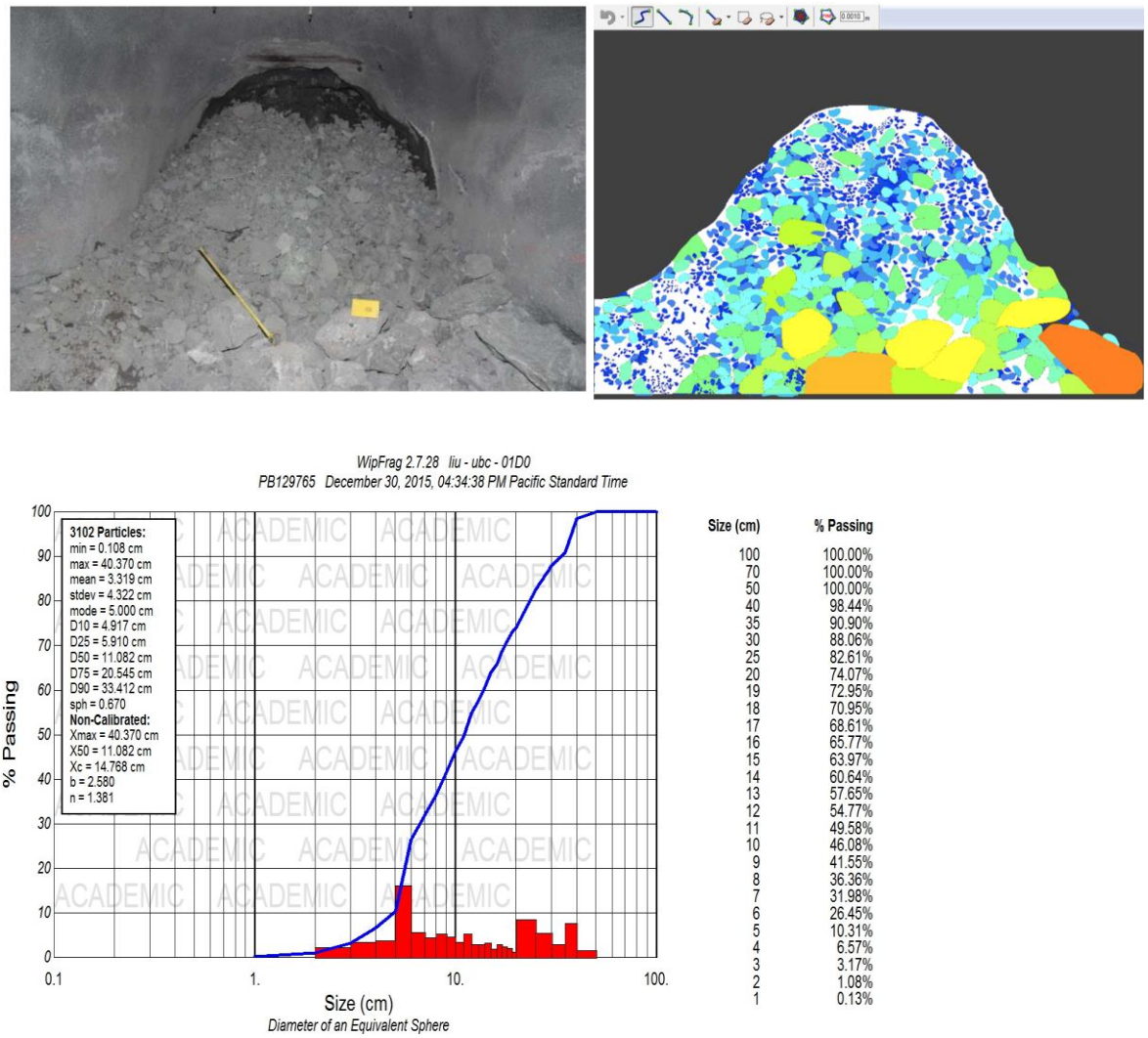

Figure 3.1: Example of drawpoint (upper) and WipFrag results (lower left shows digital solution and lower right shows particle distribution curve).

As mentioned in Chapter 2, the aim of the edge detection system is to ascertain the discontinuities of pixels. WipFrag allows users to adjust searching properties to define pixel discontinuities, through changing such thresholds (shown in Figure 3.2) to discover the best parameters for image analysis. Moreover, if the edge detection system does not provide satisfactory solutions, WipFrag also allows users to manually process images.

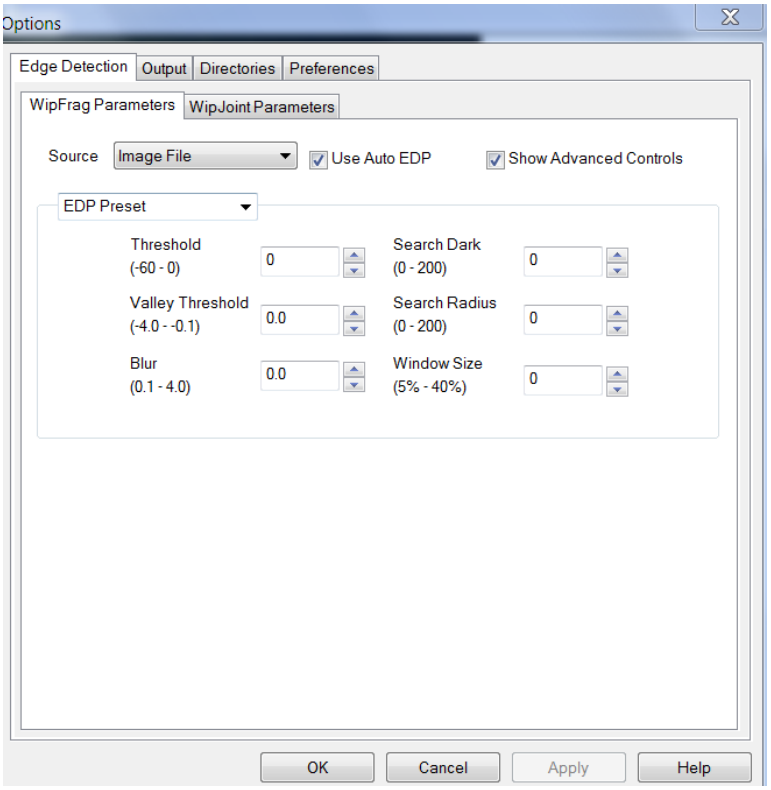

Figure 3.2: WipFrag's searching properties

For WipFrag analysis, at least one reference with proper sizes is required to define the size of rocks. However for drawpoint cases, the use of two references is suggested, as the rocks are piled-up with a certain angle, hence they are at different distances from the camera. When dealing with drawpoint cases, the other problem that should be considered is: since drawpoints are not flatly spread rocks, there inevitably will be fragments covered by other fragments. To account for this, WipFrag

provides the following tools: i) an embedded analytical correction method; ii) a zoom-merge mode that allows for a combination of results from different images; and iii) Calibration through the Rosin-Rammler method (Maerz N. H., 1996; Maerz & Zhou, 1999).

3.2.2 PortaMetrics

PortaMetrics is a Windows OS based tablet with three external cameras, as well as an embedded image analysis code, Figure 3.3. The three external cameras are able to detect the distance of PortaMetrics to measured rocks, whereby to define the size of rocks. Thus references are not required during PortaMetrics analysis. Moreover, the embedded analysis software will analyse environmental conditions and run an automatic analysis function to analyse images immediately after they are taken by PortaMetrics, thus no further office work is required. Like WipFrag, PortaMetrics also provides a manual correction function for the purpose of assisting its automatic analysis function, allowing users to manually merge or split the solution of rocks.

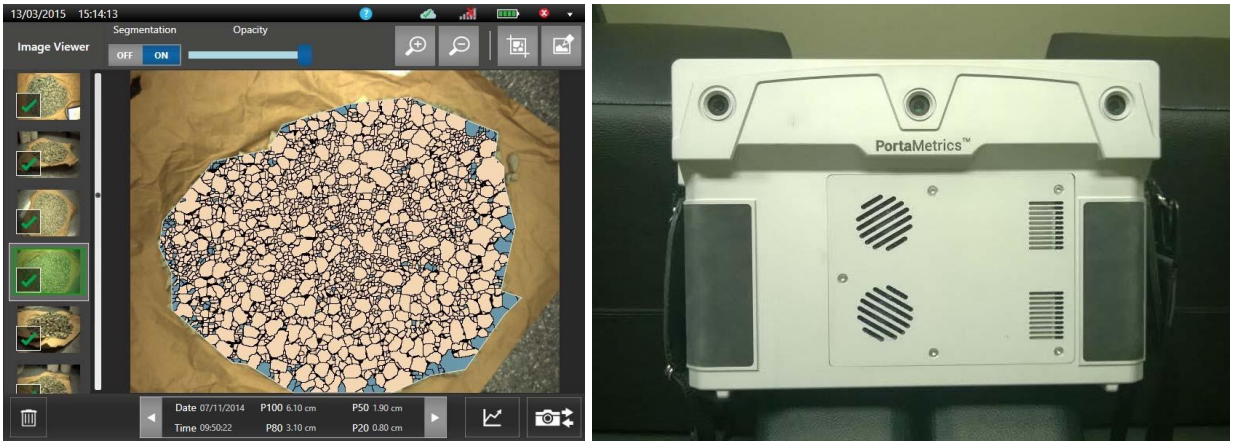

Figure 3.3: Example of PortaMetrics' user's interface and outlook.

In PortaMetrics, the definition of rock sizes is the longest dimension of the rock's 2D solution.

3.2.3 Algorithm comparison of WipFrag and PortaMetrics

Since WipFrag and PortaMetrics use different algorithms to measure rock size, it is necessary to clarify the difference of the definition of rock size within these two image processing tools. WipFrag regards the equivalent diameter to the measured rock's area as the rock size while PortaMetrics treats the rock size as the longest dimension of the rock. The differences of the definition of rock size in WipFrag and PortaMetrics are shown in Figure 3.4.

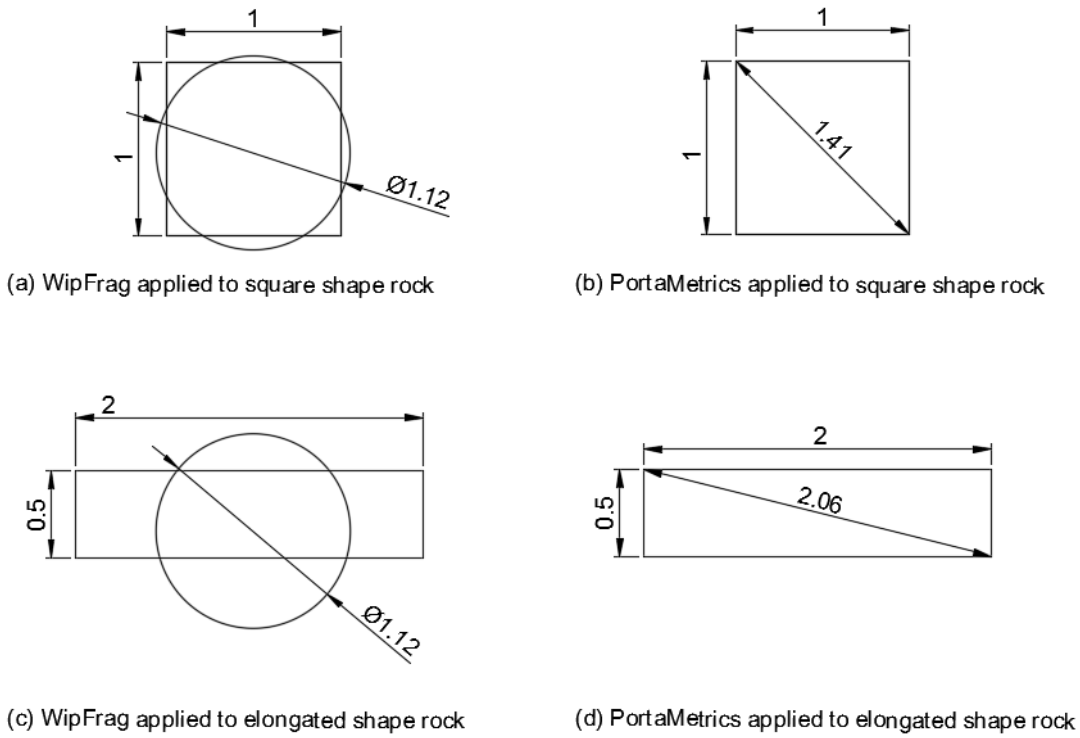

Figure 3.4: Definition of rock size in WipFrag and PortaMetrics

According to Figure 3.4, for the rocks of unit size (area), WipFrag gives the same results of 1.12 while PortaMetrics generates results of 1.41 for the square shaped rock and 2.06 for the elongated shaped rock. However, it is difficult to generate the real rock size based on a 2D solution. It is argued that shape factor should be considered when considering to obtain an actual rock size.

3.3 Laboratory based applications of WipFrag and PortaMetrics

3.3.1 Performance of manual processing

WipFrag has long been accepted by industry as a digital image processing tool. In the author's experience, the manual correction function will greatly help the imaging processing results. In this study, another way that was considered to obtain secondary fragmentation distribution is to manually process drawpoint images using WipFrag. In order to test the accuracy of WipFrag's manual correction function, two samples were prepared and tested. Screening tests were implemented with the samples to obtain a PSD curve. The rock samples were placed flat on a brown paper to minimize overlapping, pictures were taken perpendicular to the rock sample's surface, and a rectangular board reference was provided. Figure 3.5 shows a rock sample and corresponding solution of WipFrag through manual processing while Figure 3.6 shows the comparison of actual and generated PSD results. Sample II displays similar results, shown in Figure 3.7.

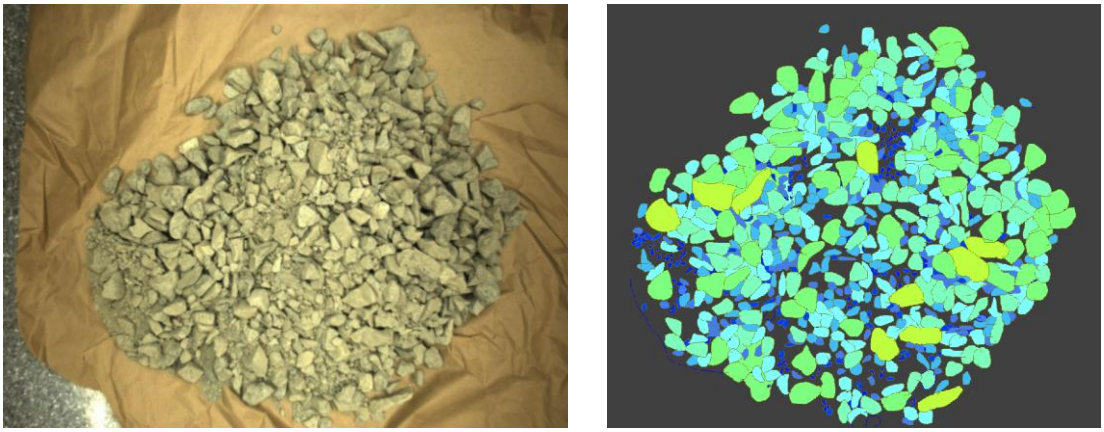

Figure 3.5: Example of a rock sample and WipFrag manual processing solution

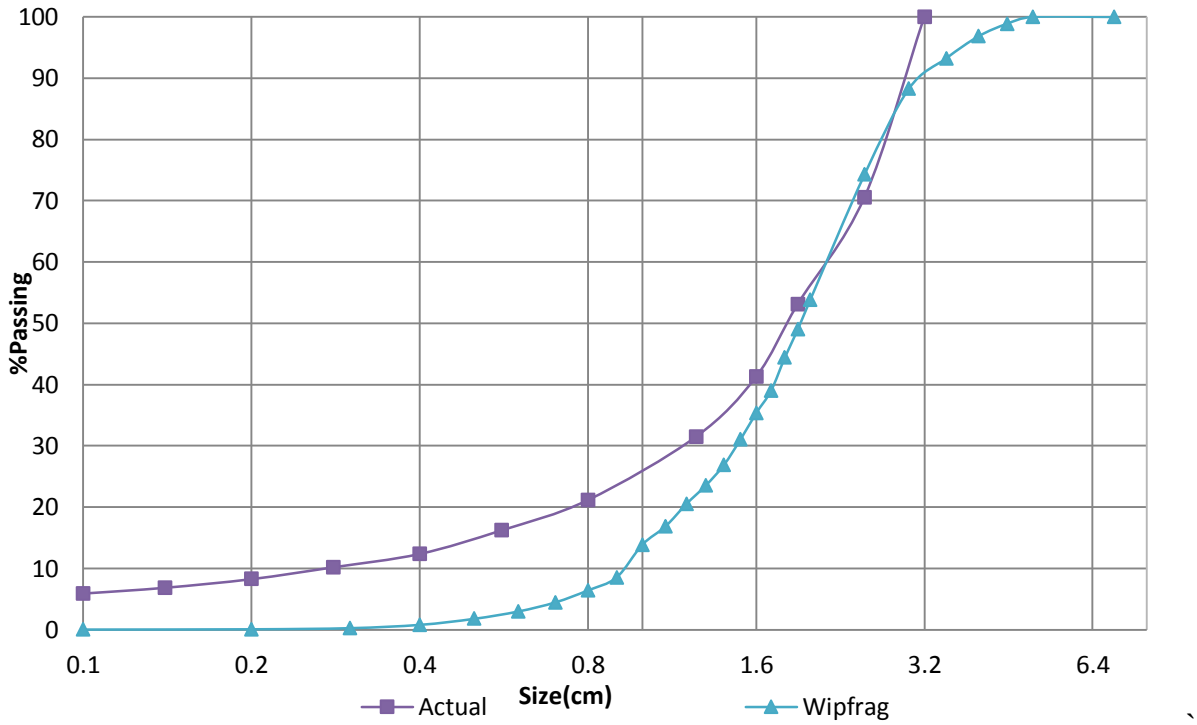

Figure 3.6: Particle size distribution of sample in Figure 3.5.

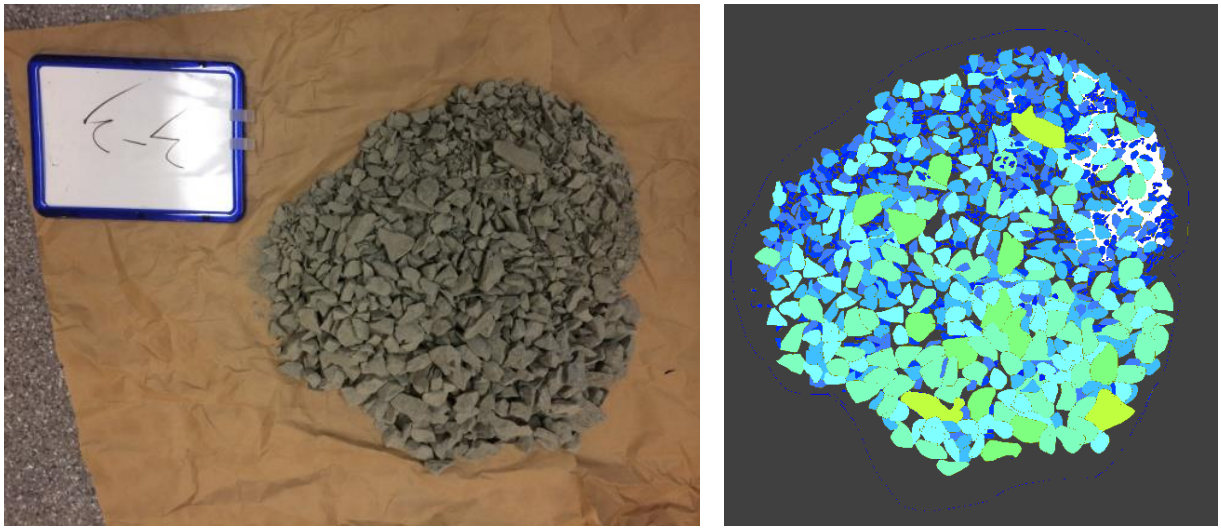

(a)

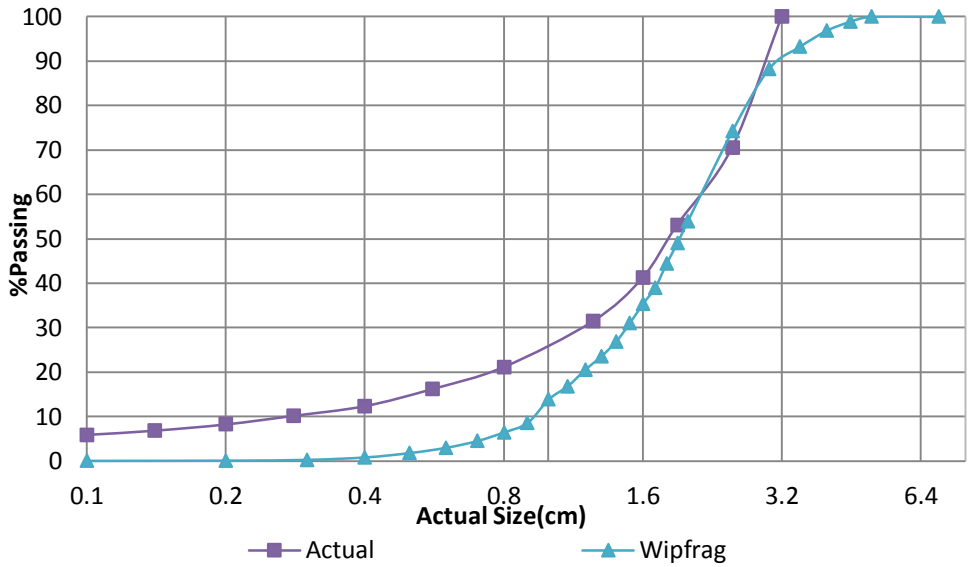

(b)

Figure 3.7: Sample II (a) An example of sample II (left) and WipFrag solution (right). (b) PSD curves of sample II and result from WipFrag.

According to Figure 3.6 and Figure 3.7, differences occur mainly below the P_{30} and over the P_{90} value. Difference of low % passing values is probably because fines of rock samples are not defined. For differences over P_{90}, this is because small rocks overlap over big ones and make the bigger rocks' sizes appear in WipFrag.

Generally, manual processing rock sample images provides reliable results with % passing values from P_{50} to P_{80}. Though the WipFrag manual processing function has been proven to be reliable for secondary fragmentation measurement, the considerable time for manual processing makes it impractical for a large amount of images to be processed. Based on the author's experience, it takes more than two hours to process one drawpoint image.

It is necessary to conduct laboratory validations of the performance of PortaMetrics (as it is a newly introduced tool) before applying it to the study of caving fragmentation measured in the field at the drawpoints. The recent version of PortaMetrics provides a manual fixing tool which allow users to define rocks based on processed images by splitting one large rock into multiple or by merging multiple small rocks into a large one. However, to manually processing a drawpoint image using PortaMetrics is considered impractical, as this would require too much time and labor.

3.3.2 Performance of edge detection system

It is assumed that both WipFrag and PortaMetrics would accurately calculate the size of rock fragments if proper manual correction was used. However, since large amounts of drawpoints are anticipated to be measured and analysed, it is suggested to conduct tests using only an automatic analysis system. Based on this point of view, experiments were arranged for the purpose of evaluating the performance of the edge detection systems of both WipFrag and PortaMetrics.

In order to assess the performance of edge detection system, tests of two different samples were prepared. Screening tests were conducted to obtain the PSD of the two samples. The experiments were arranged as following (see also Figure 3.8):

i. The size of samples were between 0.1cm to 6cm.
ii. The rocks were placed flat to avoid overlapping.
iii. The tests were arranged in the laboratory with comprehensive lighting to minimize the shadows of the rocks and the operator.
iv. The rocks were placed on brown paper so the colour of background did not disturb the analysis.

v. The cameras of the PortaMetrics tablet were oriented perpendicularly to the surface of rocks.

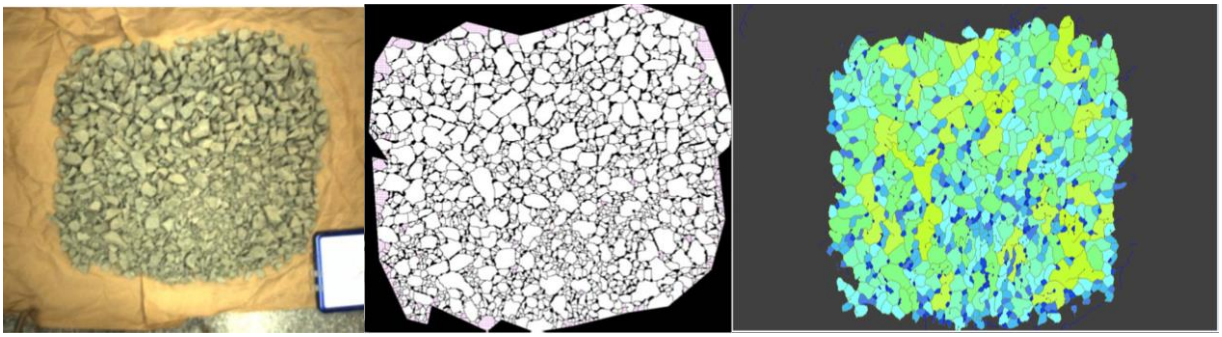

Figure 3.8: Example of rock sample (left) and corresponding solution in PortaMetrics (middle) and WipFrag (Right)

According to Figure 3.8, both WipFrag and PortaMetrics were able to identify the coarser (upper left in the figure) and finer (lower right in the figure) rocks. However, PortaMetrics interpreted some parts of the edges of the rocks as fines (noted as pink). In order to quantitatively describe the performance, the particle distribution curve generated by WipFrag and PortaMetrics were compared against the real particle size curve, shown in Figure 3.9.

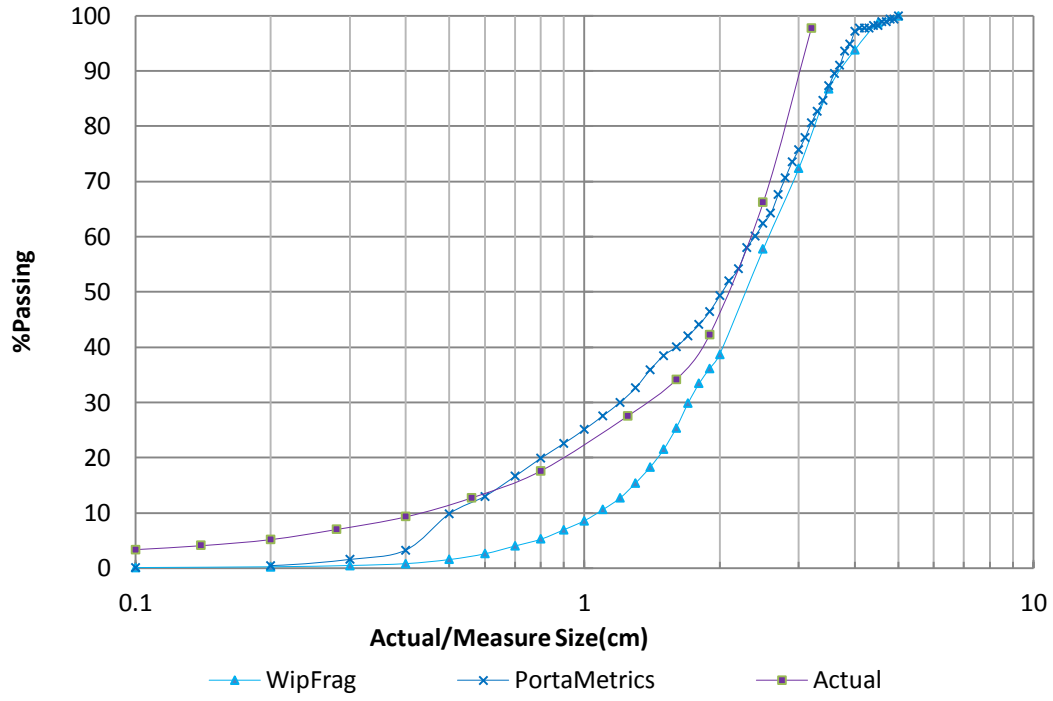

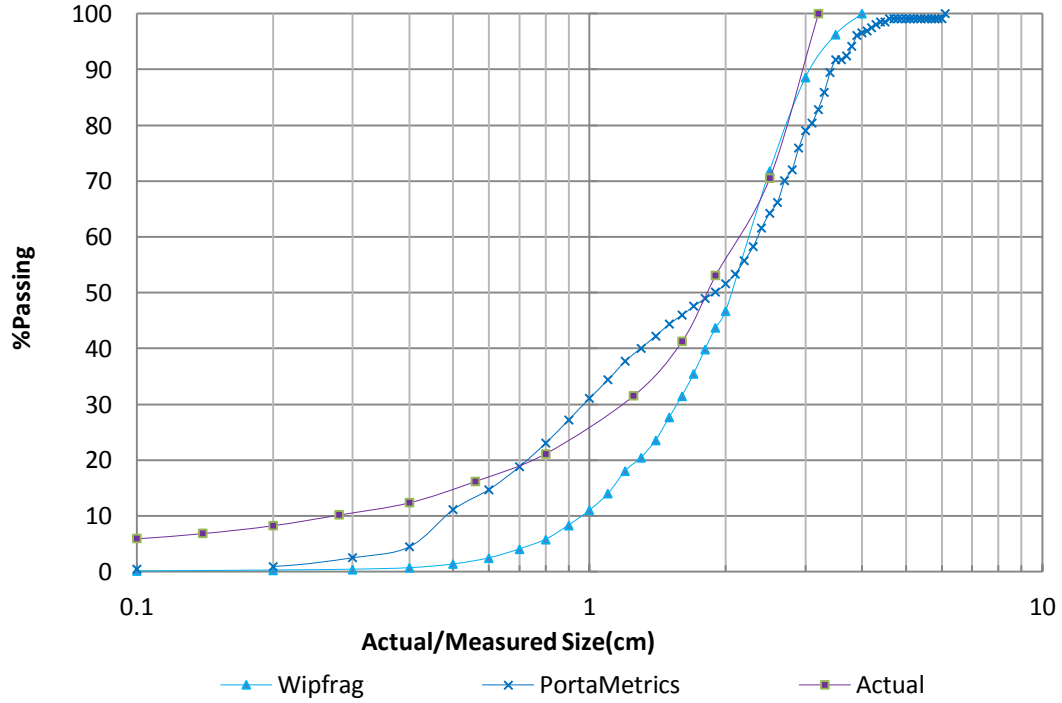

Figure 3.9: Size distribution of the two samples generated by WipFrag and PortaMetrics.

According to Figure 3.9, most of the differences occurred with under P_{40} and over P_{80} values. It is noticeable that PortaMetrics generates fewer differences under P_{30} values than did WipFrag; this is because PortaMetrics is able to define fines in the image while WipFrag's fine definition requires manual editing, which was not applied in the tests.

Generally, in the lab environment, both WipFrag and PortaMetrics provide reliable results with values ranging from P_{50} to P_{80}. However, % passing values of under P_{40} and over P_{90} should not be used for any purpose as they did not appear to be representative of the measured samples. It is worth mentioning that the results of using WipFrag to manually process images should not be very different applied in either good or extreme environments, as long as the particles can be recognised by the human eye and proper references can be set.

3.4 Digital image processing applied to underground secondary fragmentation measurement

Section 3.3 has proven that both WipFrag and PortaMetrics generate reliable values from P_{50} to P_{80}, using their own edge detection system. However, in underground applications, due to such environmental limits as illumination, shadow and dust, the results of any digital image processing may be significantly affected. This section presents the performance of WipFrag and PortaMetrics as applied to actual underground drawpoints. As there are more fines at drawpoints, the previous sections show that low % passing values are difficult to measure, this section mainly focuses on % passing values between P_{50} to P_{90}; particles under 15mm are defined as fines (white colour in WipFrag).

Since it is extremely difficult to obtain the particle size distribution of a drawpoint using physical screening, whereas, the PSD curves generated by manually drawing the edges of the rocks provide relatively reliable results, it is considered that the manual process by WipFrag is able to represent the particle size distribution of drawpoints. In this section, the automatic analysis results from WipFrag and PotaMetrics are compared with the manual process by WipFrag.

3.4.1 Methodology

The procedure of capturing images of drawpoints should be well planned to improve underground working efficiency, e.g. the cameras of PortaMetrics and lighting equipment should be fully utilised during their battery lifetimes. The size of the drawpoints examined in this procedure was 3.4m wide by 3.4m high, according to Scott Wilson Mining (2009). It is suggested that two lights be used to illuminate both sides of the drawpoints, as one light may not be able to light up the whole drawpoint area. The choice of lighting equipment should be based on concerns such as:

i. Lighting intensity - Lighting equipment should be able to light up the whole drawpoint area;
ii. Lighting uniformity - The light should be uniformly distributed on the rock piles, otherwise there will be sharp changes of contrast between degrees of brightness and will affect the imaging processing results;
iii. Battery lifetime - It is not convenient to charge light equipment in underground areas, thus the light battery lifetime should be guaranteed to be sufficient for the underground trip; and
iv. Portability - Lighting equipment should be easy to carry between drawpoints.

The choice of the lighting equipment for the underground image capturing of this research was Workstar NightSearcher; specifications are shown in Figure 3.10 (Nightsearcher, 2015).

Power Type: **Rechargeable**

Light Output: **2200 High**

Running Time: **7h Low | 3h High**

Battery: **Li-ion**

Light Source: **Cree LED**

Max Beam: **20 Metre Beam Distance**

Light Modes: **2 Light Modes: High and Low**

Colour: **Green**

Figure 3.10: Specifications of underground image capturing lighting equipment (Nightsearcher, 2015).

The positioning of the light equipment and cameras were designed as follows (WipFrag Sampling and Analysis Guide, 2014):

- Position lights equal distances to left and right of camera position and as far apart as possible.
- Position lights as high as possible.
- Aim light on right towards left edge of drift (approx. 45 degrees from lens axis).
- Aim light on left towards right edge of drift (approx. 45 degrees from lens axis)

Figure 3.11 shows the focus position of lighting equipment and cameras

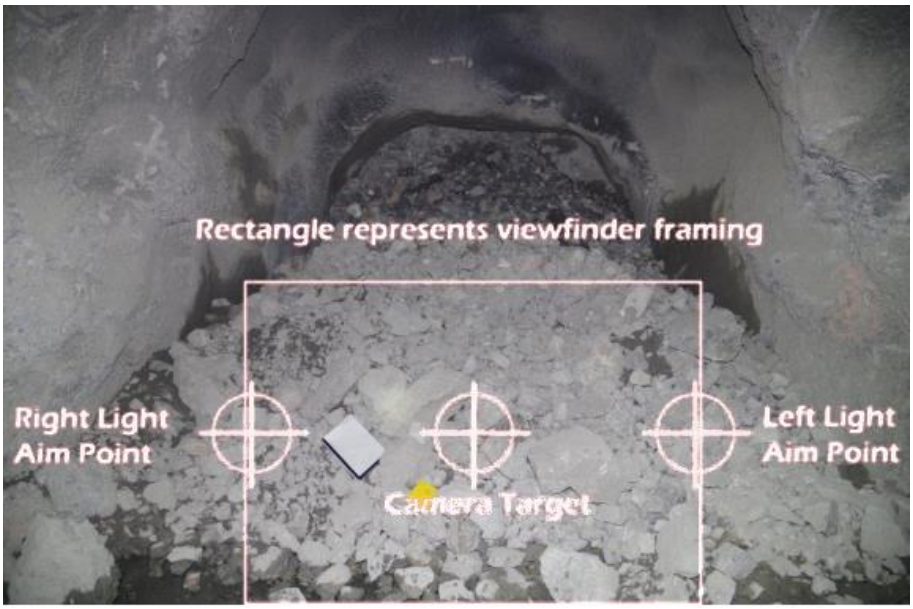

Figure 3.11: Diagram of lighting and camera target. (WipFrag Sampling and Analysis Guide, 2014).

3.4.2 WipFrag

For WipFrag, two references were placed both at bottom and top locations in drawpoints. As WipFrag's manual processing provides, the most accurate result to the actual PSD and is not affected by environment factors, it is assumed that the curve generated by manual processing can legitimately represent the drawpoint size distribution.

Four drawpoint images were taken and analysed by WipFrag using both the edge detection function and manual processing approaches. An example of one image captured at drawpoint D11N (taken on November 12th, 2015) in West Cave and corresponding manual processing solution is shown in Figure 3.12.

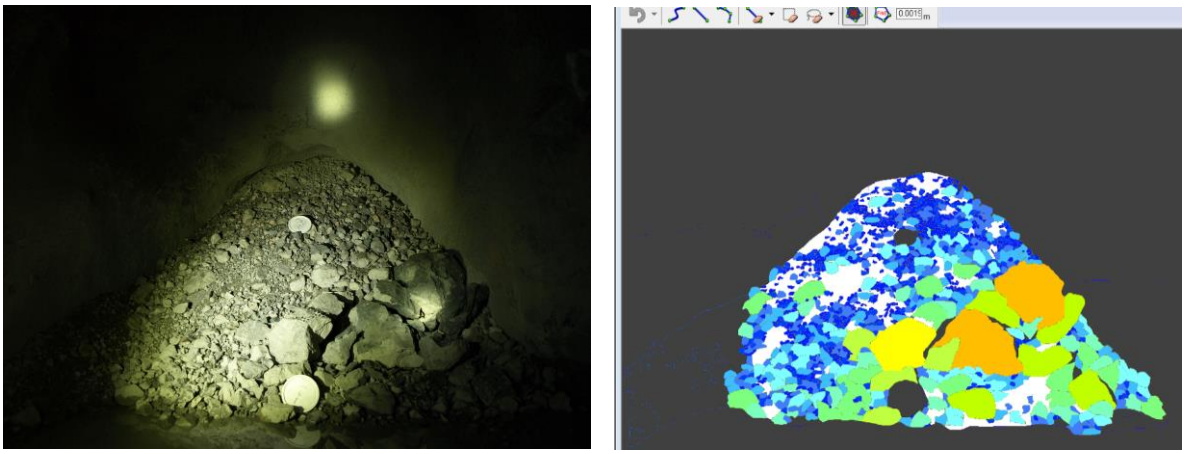

Figure 3.12: Drawpoint image and solutions manually processed using WipFrag

The drawpoint photo was then analysed using edge detection system; the result is shown below.

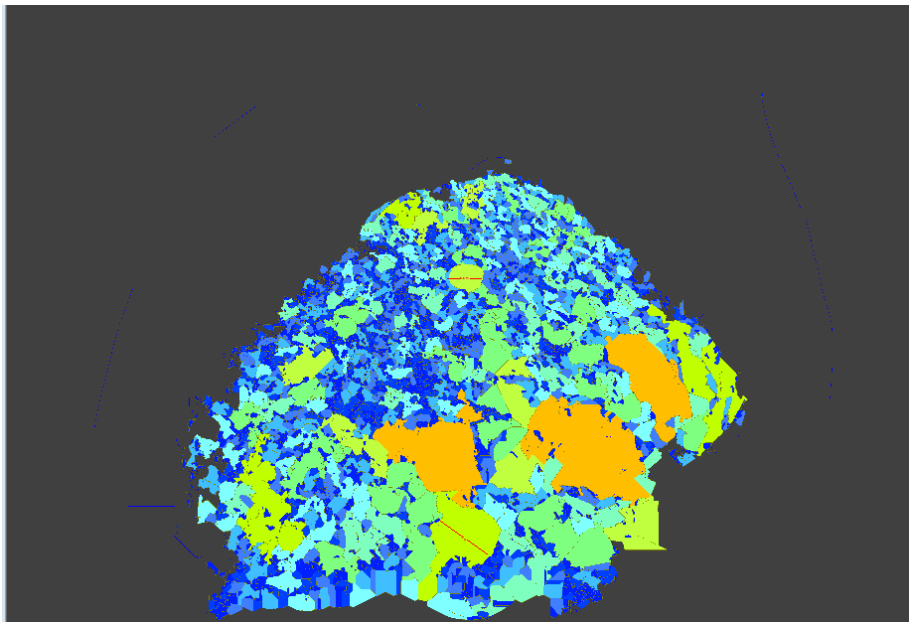

Figure 3.13: Automatic solution of Drawpoint D11N (image was taken on November 12th, 2015)

Optically, the illuminated area was well defined using automatic solution, the result was similar to manual solution. The dark area at the bottom right corner of the picture was not detected.

The PSD curves from both manual and automatic analysis are generated and shown in Figure 3.14.

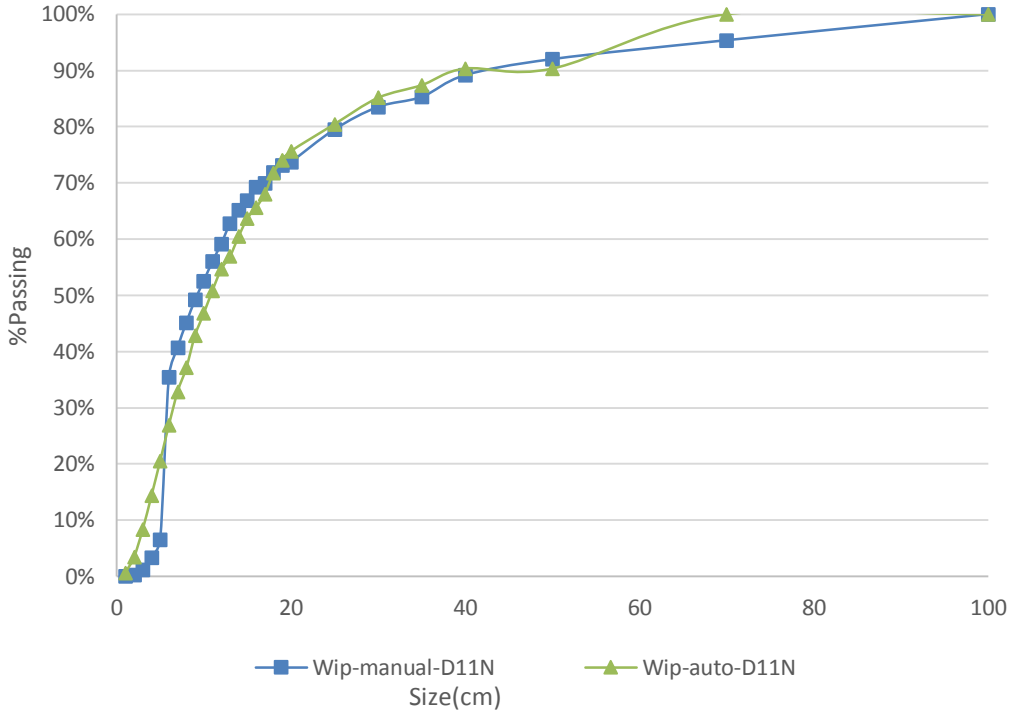

Figure 3.14: PSD curves generated by manual and automatic processing.

The relative differences of P_{50}, P_{60}, P_{70}, P_{80} and P_{90} are describe using equation:

$$\text{RD\%} = \frac{P_a - P_m}{P_m} \times 100\%$$

Where, P_a is the %Passing of automatic edge detection, while P_m is the %Passing value of manual processing. The calculation of RD% for P_{50}, P_{60}, P_{70}, P_{80} and P_{90} is shown in Table 3.1.

	Wip-Manual	**Wip-Auto**	**RD%**
P_{90}	52.77	39.44	-25%
P_{80}	25.64	24.54	-4%
P_{70}	17.02	17.53	3%
P_{60}	12.25	13.88	13%
P_{50}	9.25	10.80	17%

Table 3.1: Wip-Auto RD% values for P_{50}, P_{60}, P_{70}, P_{80} and P_{90}

According to Table 3.1, P_{70} and P_{80} values are most accurately captured by edge detection system while as %Passing diffuses to P_{50} and P_{90}, more differences were generated. It is worth mentioning that a well-processed image requires a sound understanding of the searching parameters shown in Figure 3.3. Inappropriate choices of those parameters may lead to incorrect results. For results of the other images, see Figure 3.15, 3.16 and 3.17 (all images were taken on November 12th, 2015).

(a)

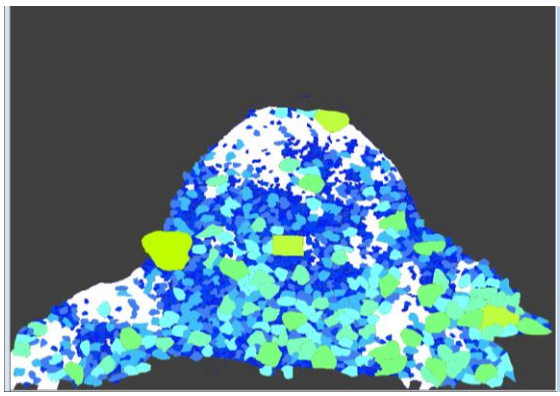

(b)

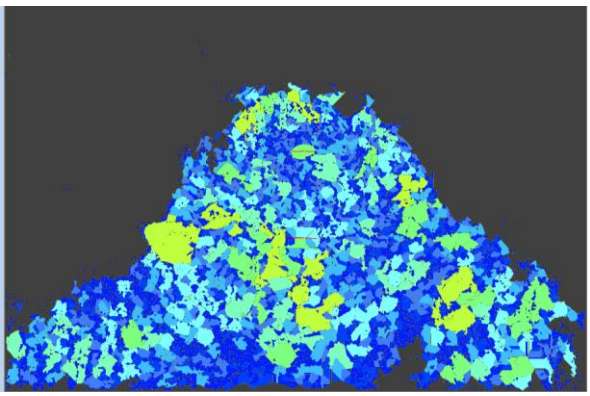

(c)

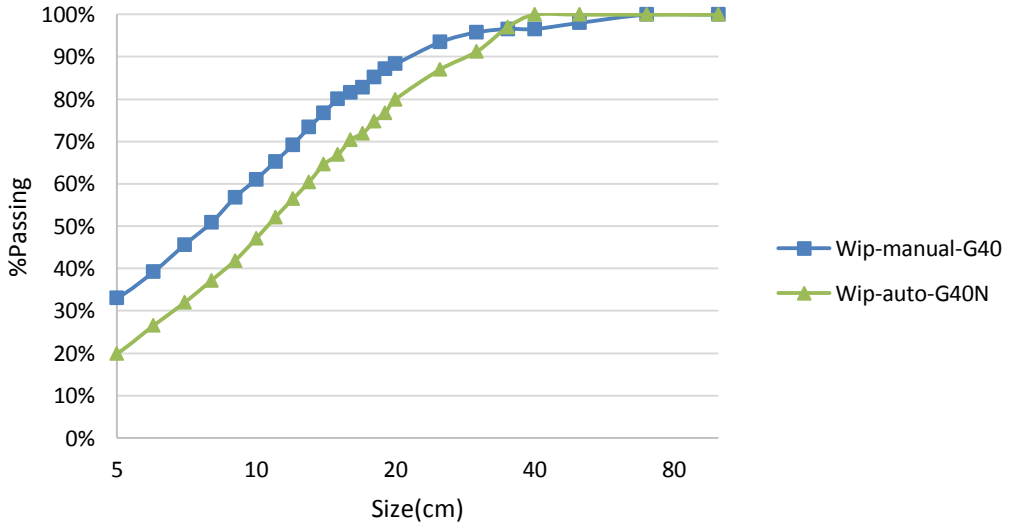

(d)

Figure 3.15: Image processing results of drawpoint G40N: a) Drawpoint image; b) WipFrag manual processing; c) WipFrag automatic edge detection processing; and d) Particle size distribution curve comparison.

(a)

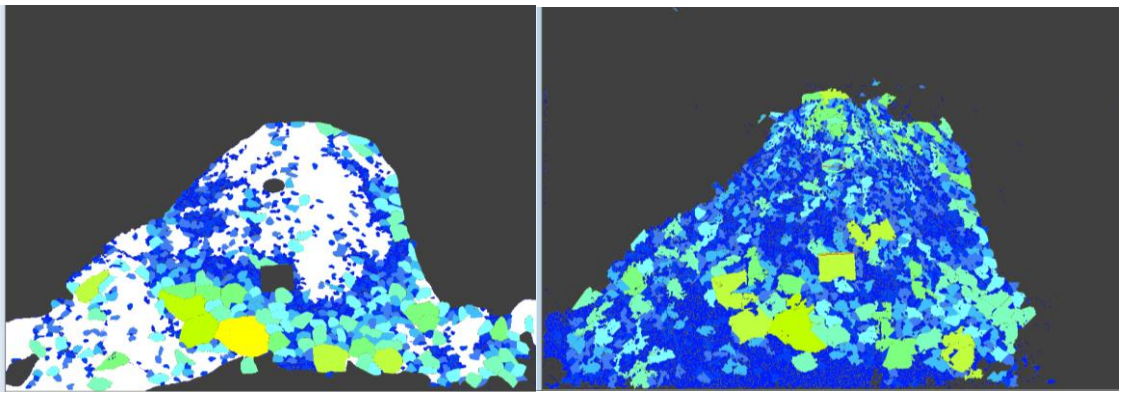

(b) **(c)**

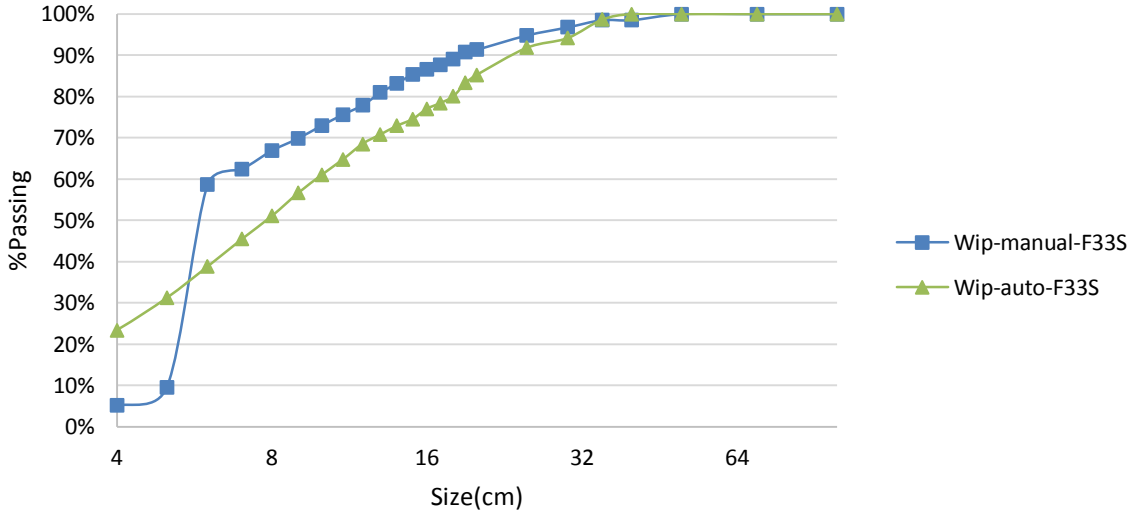

(d)

Figure 3.16: Image processing results of drawpoint F33S: a) Drawpoint image; b) WipFrag manual processing; c) WipFrag automatic edge detection processing; and d) Particle size distribution curve comparison.

(a)

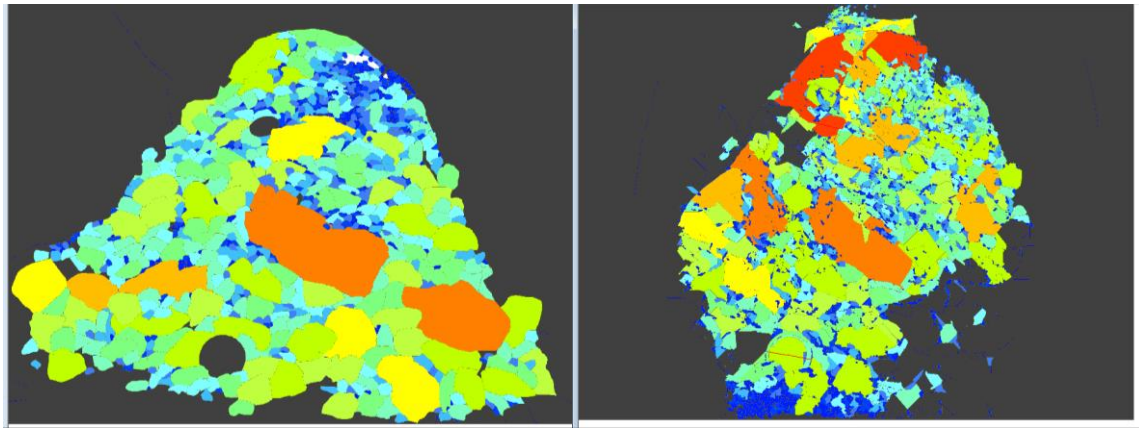

(b) **(c)**

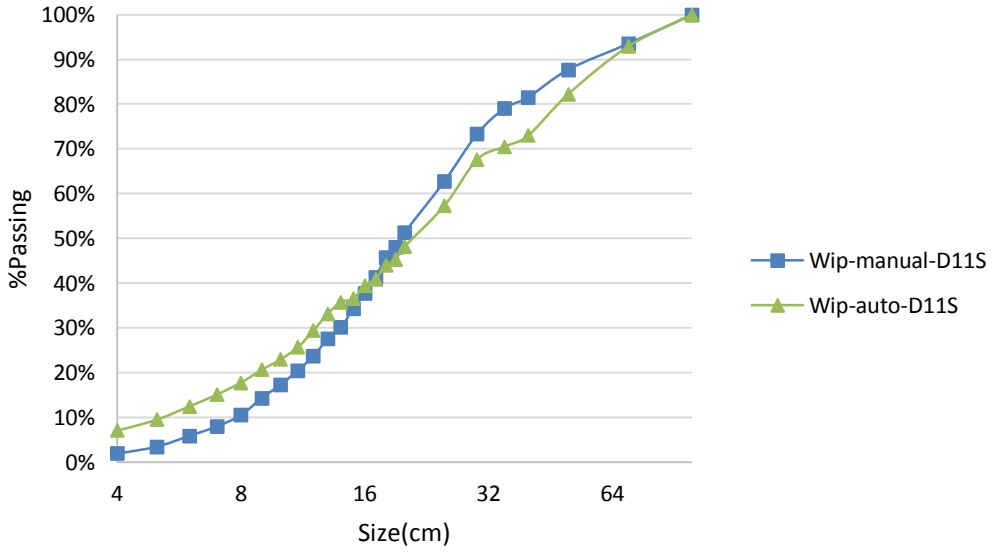

(d)

Figure 3.17: Image processing results of drawpoint D11S: a) Drawpoint image; b) WipFrag manual processing; c) WipFrag automatic edge detection processing; d) Particle size distribution curve comparison.

3.4.3 PortaMetrics

The PortaMetrics analysis required that three images from different angles were taken at each drawpoint and that an overall representation of three curves was generated. An example of PortaMetrics images taken from four different drawpoints and corresponding solutions are shown in Figure 3.18. 3.19, 3.20 and 3.21. All images were taken on November 12th, 2015. The results from PortaMetrics were also compared to the images manually processed by WipFrag.

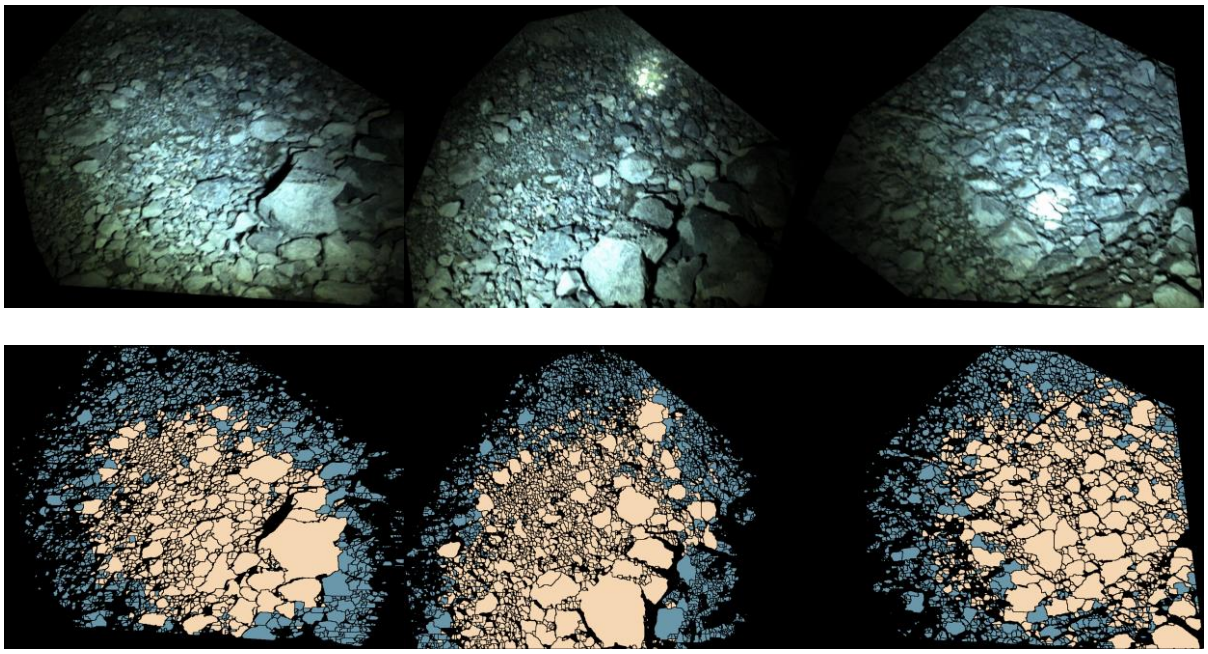

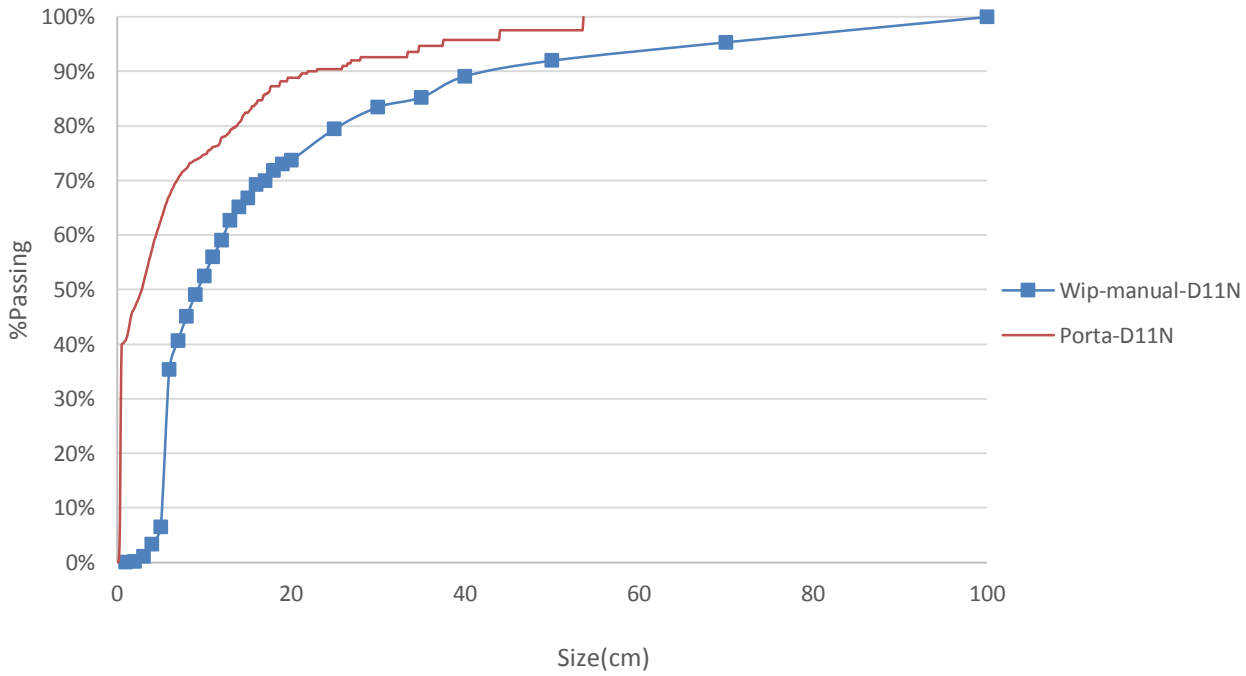

Figure 3.18: Image of drawpoint D11N and corresponding solution in PortaMetrics (images were taken on November 12th, 2015)

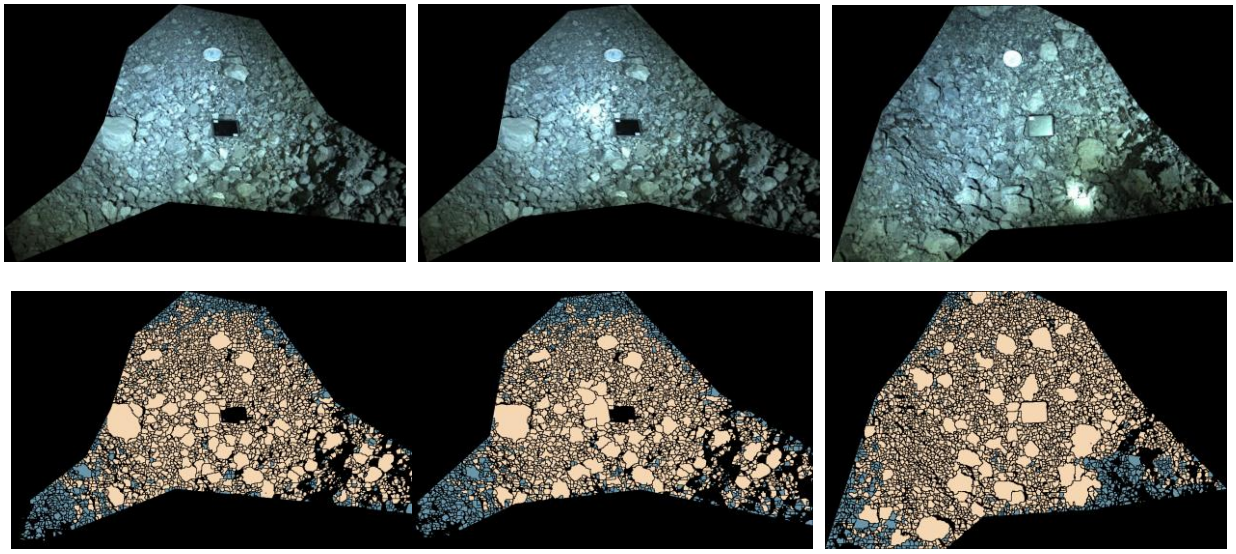

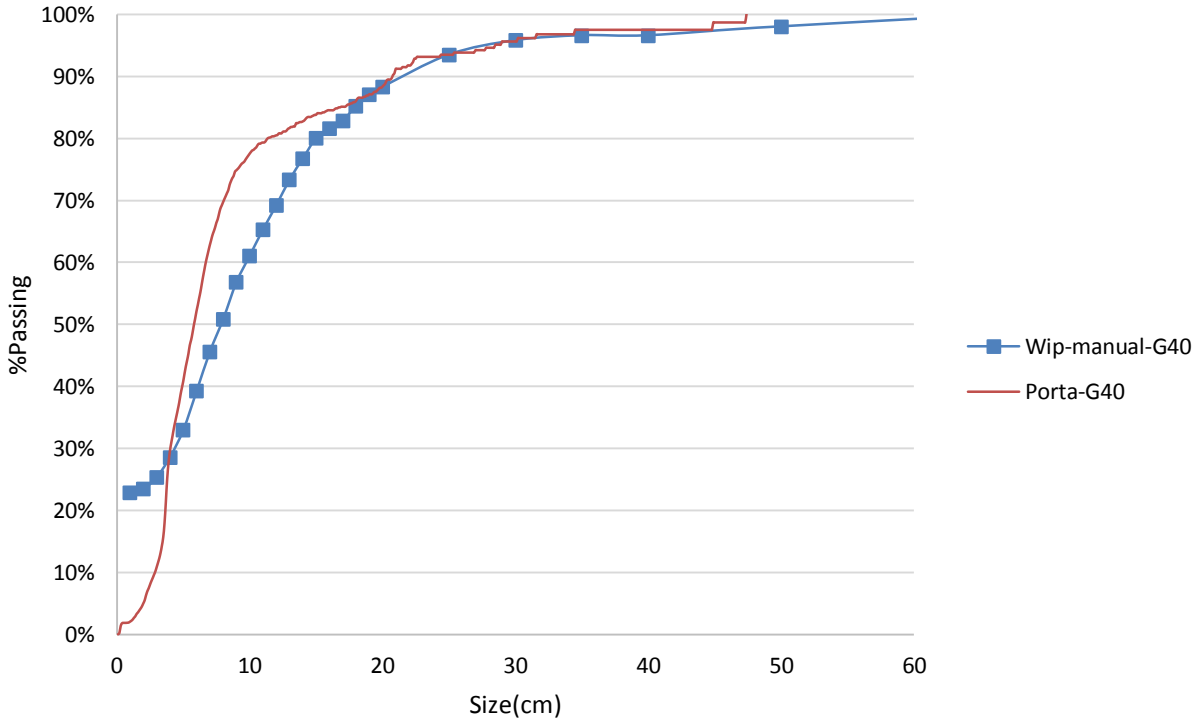

Figure 3.19: PortaMetrics automatic processing solution of drawpoint G40N and particle size distribution comparison to WipFrag's manual processing.

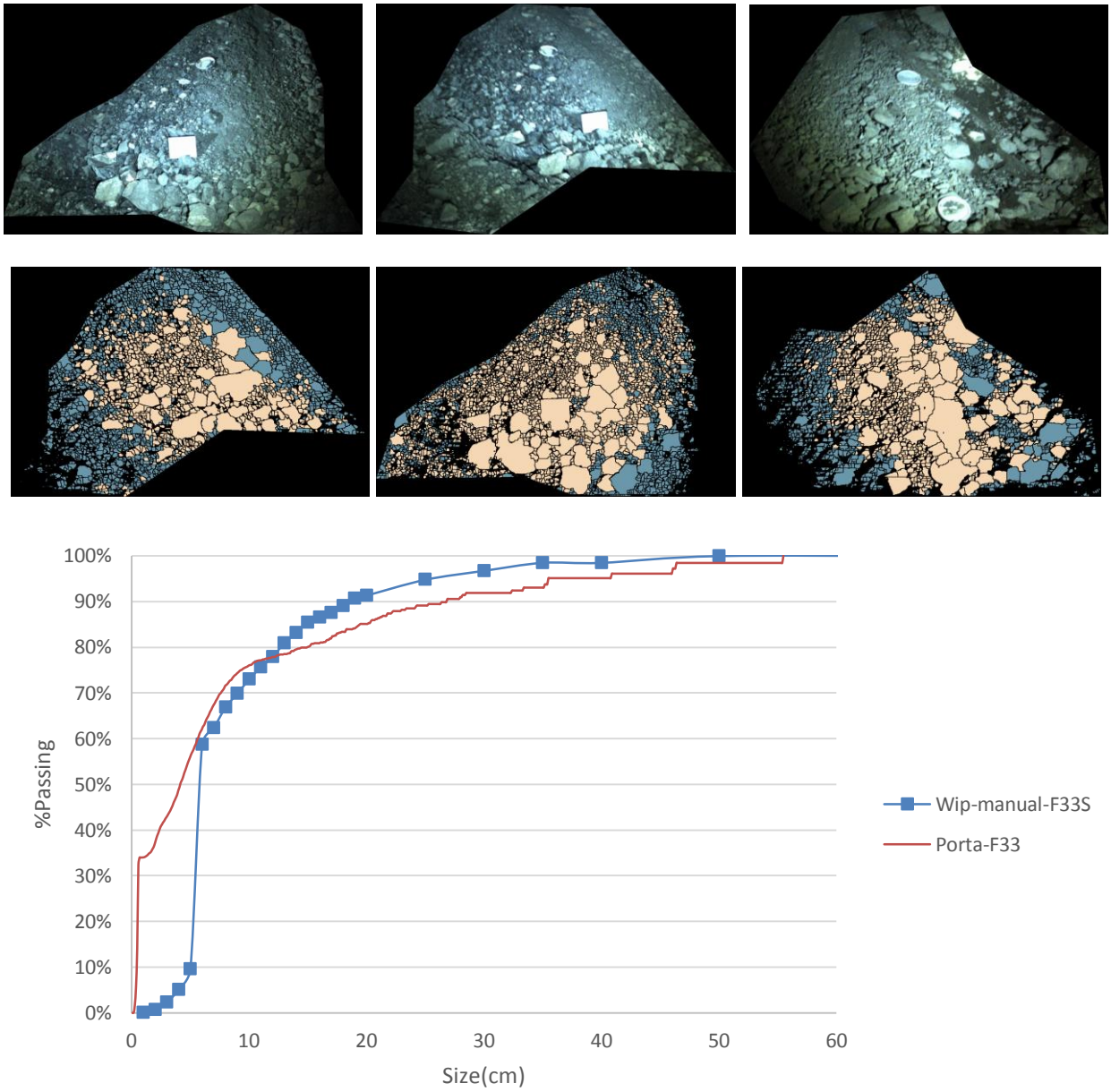

Figure 3.20: PortaMetrics automatic processing solution of drawpoint F33S and particle size distribution comparison to WipFrag's manual processing.

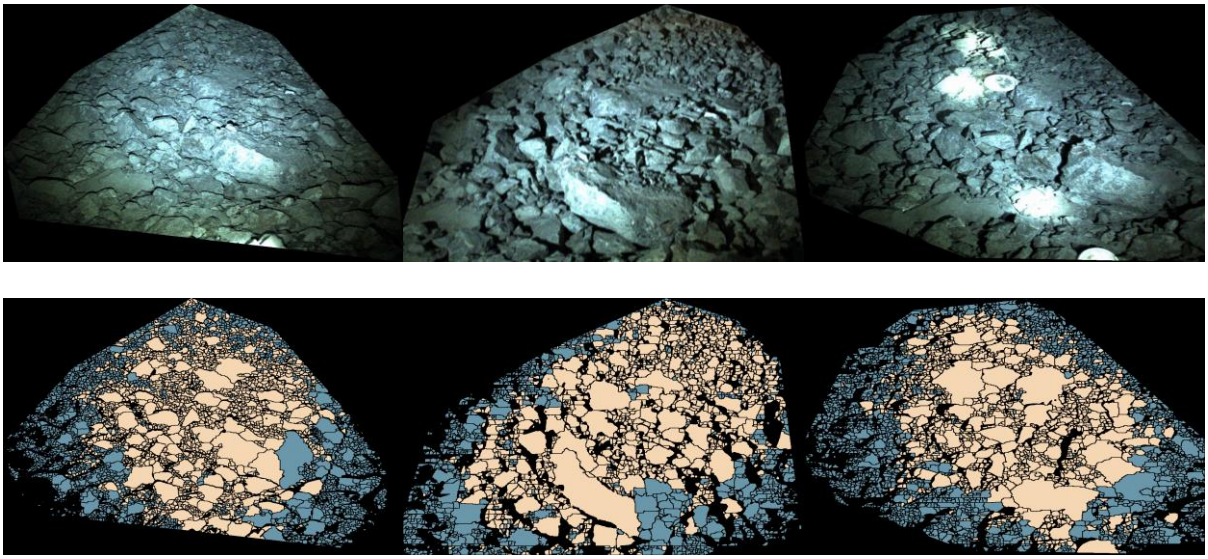

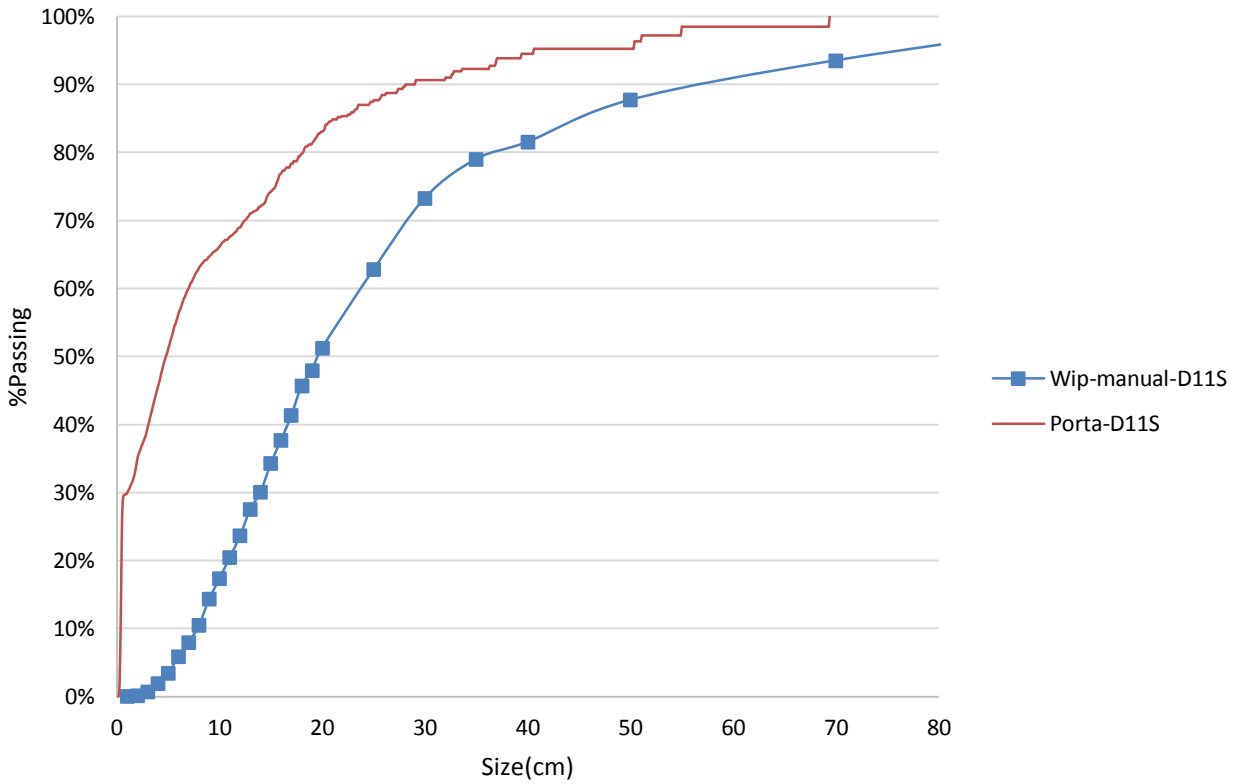

Figure 3.21: PortaMetrics automatic processing solution of drawpoint D11S and particle size distribution comparison to WipFrag's manual processing.

According to Figure 3.18, 3.19, 3.20 and 3.21, %Passing values of under P_{50} generate significant difference than values over P_{50}. Generally, P_{80} was considered as the most accurately captured value by PortaMetrics. It is argued that lighting is one of the main factors that affect PortaMetrics' performance; the question being whether the big rocks in the image are illuminated and captured or covered by shadow and defined as fines or an invalid area, which can generate significant differences; an indicator of this point of view is that the big rocks in Figure 3.19 and 3.20 are better distinguished than those in Figure 3.18 and Figure 3.21 and lead to less of a size difference in the final PSD curves.

3.5 Conclusion

Both WipFrag and PortaMetrics showed acceptable performance in the lab environment with %Passing values from P_{50} to P_{80}. However, it became a challenge for both WipFrag and PortaMetrics when dealing with more extreme environments. Due to such limits as insufficient lighting and dust, both WipFrag and PortaMetrics showed their limitations when applied to underground drawpoints.

For WipFrag, the results relied heavily on the choice of analysis parameters shown in Figure 3.3, where the % passing values around P_{70} and P_{80} were relatively accurately detected. However, for PortaMetrics, more study is needed to improve its performance before being applied to real drawpoint cases.

However, for the purpose of generating reliable results for the preliminary stage of this research, images were analysed manually using WipFrag. It is argued that automatic analysis should be the most employed means when there is an abundance of images that need to be analysed.

Chapter 4: A Discrete Fracture Networks model for the New Afton block caving mine West Cave in-situ fragmentation

4.1 Introduction

This chapter introduces the approach of constructing a DFN model with respect to New Afton West Cave orebody to obtain the in-situ fragmentation. The coordinates of the New Afton mine are based on the Universal Transverse Mercator (UTM) system, specifically in Zone 10. The coordinates of the West Cave fall generally within 3244 - 3520 x-axis, 1955-2014 y-axis and the elevation of the extraction level is around 5070 z-axis. Figure 4.1 shows a plan view of New Afton's West Cave drawpoints.

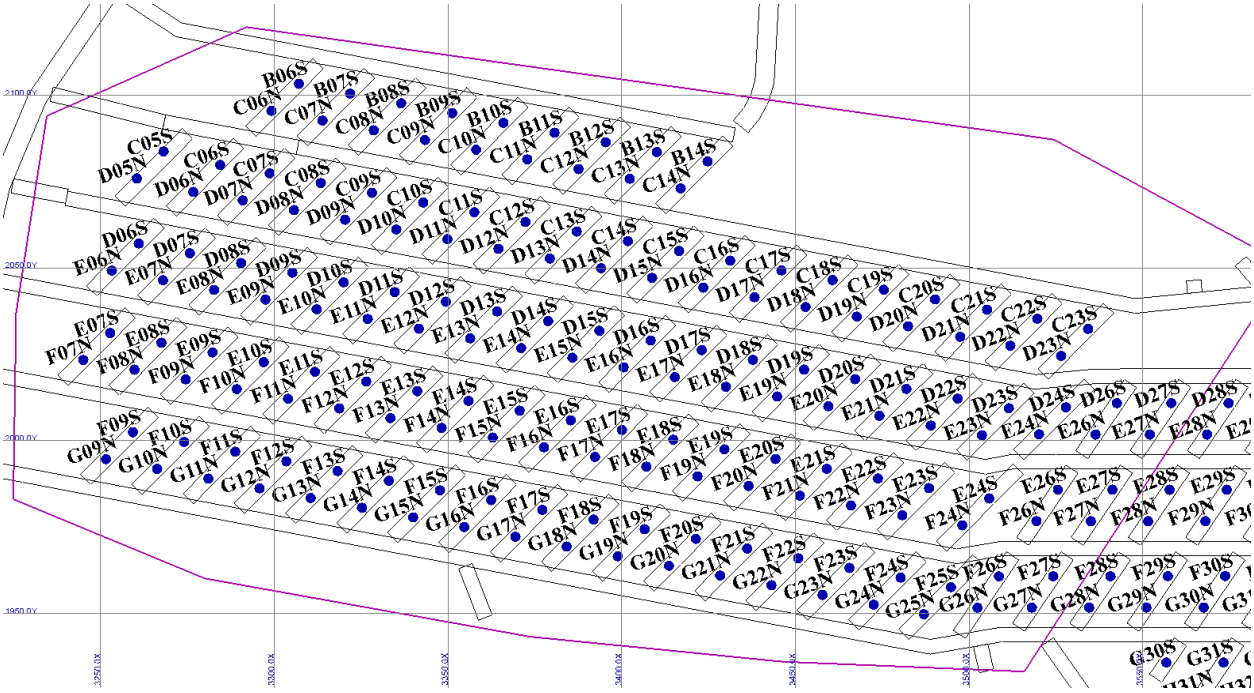

Figure 4.1: Plan view of West Cave drawpoints (provided for draft purposes only)

4.1.1 Block model assessment

The geological survey indicated a considerable amount of faults in the cave zones. They are: Hanging Wall Faults, Footwall Faults, Northeast Faults, Northwest Faults and North Faults. The

previous record of hang-ups indicated that oversizes mainly occurred at the boundary of the cave zone where few faults are located. It was anticipated that the DFN model would show coarser fragmentation at the boundary of the cave zone than in the fault zones.

4.2 Site data analysis

The construction of a volumetrically simple DFN model requires the definition of:

- Fracture spatial model
- Fracture intensity distribution
- Fracture size distribution
- Fracture orientation distribution
- Fracture termination

The data collected from New Afton West Cave zone was applied to simulate the DFN model, as follows:

- Geological core information: this was used to calculate the fracture frequency P_{10} values. It was noted that the drill cores that were used in New Afton are non-oriented and the dip direction of fractures was not captured, thus geological cores were not used to estimate fracture orientation distribution.
- Drift mapping data at apex level: this was used to estimate fracture orientation distribution and fracture length distribution. The drift mapping data were limited by the apex level, problems caused by this issue is explained in the following paragraphs

In this research, since information on fracture orientations along boreholes was not available, the fracture orientation distribution estimated from the drift mapping data in the apex level might not have represented the orientation distribution of the whole cave zone. However, the data from the drift mapping provided reasonable assumptions for the fracture orientation distribution.

The lack of fracture orientation data along boreholes also impedes directly generating a fracture block model and further, a calculating P_{32} distribution of the block model. It is argued that the quality of input data is vital for DFN model simulation and that the geological survey should fully consider its further application when conducted. Based on such background, in this chapter, P_{32} values that are close to boreholes are shown to have been calculated utilizing the fracture frequency P_{10} values along boreholes as well as having used a C_{31} conversion process.

The general procedure of constructing a DFN model with respect to New Afton West Cave is schematically shown in Figure 4.2.

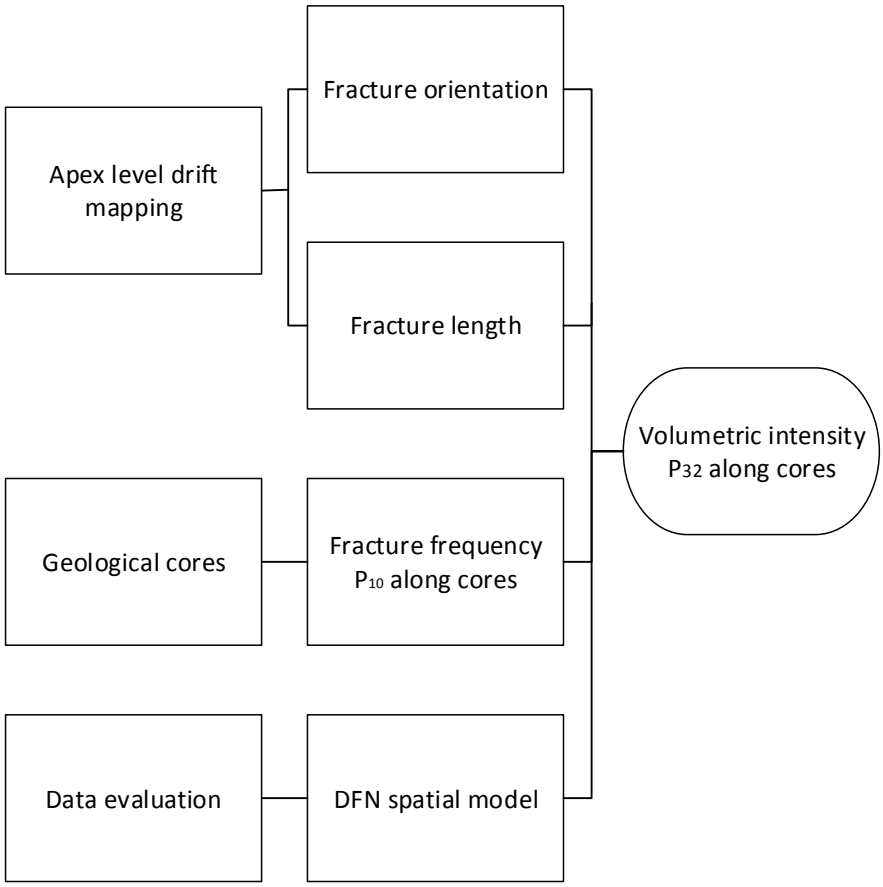

Figure 4.2: Schematic procedure for New Afton West Cave P_{32} value acquisition.

4.3 Fracture spatial model

The choice of a DFN spatial model is normally based on assumptions made from geological survey and field data. FracMan provides three types of the most commonly used spatial model: Enhanced-Baecher, Nearest Neighbour and Fractal Levy-lee. Enhanced-Baecher is a stationary model that is normally used to generate randomly distributed fractures and is generally appropriate for different applications. (Elmo, 2006) As no significant data indicated that fractures follow a nearest neighbour or fractal levy-lee distribution, the Enhanced-Baecher model was considered to be an appropriate fracture spatial model.

4.4 Fracture orientation distribution

Fracture orientations were obtained from apex level mapping, and lower hemisphere stereonet plots in Dips 7.0 (Rocscience, 2015) is shown in Figure 4.3. As the mapped orientation data were highly dispersed and did not show significant distribution types, it was decided to use a bootstrapping approach for fracture orientation (Rogers et al., 2009). The bootstrapping approach in FracMan generates fracture orientation distribution based on the original orientation distribution. For validation purposes, a realization of 5000 fractures generated through the bootstrapping approach was conducted (fracture orientation results are shown in Figure 4.3).

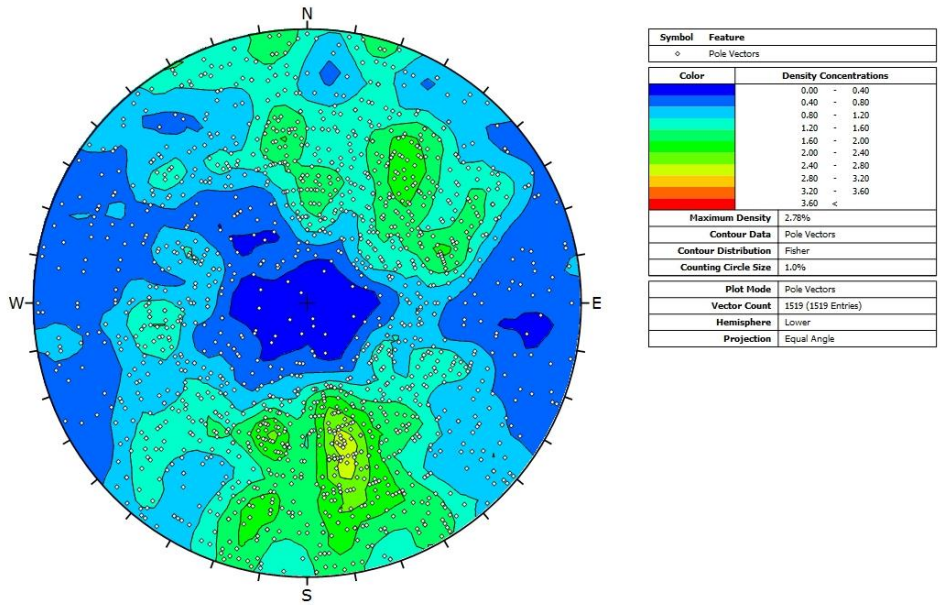

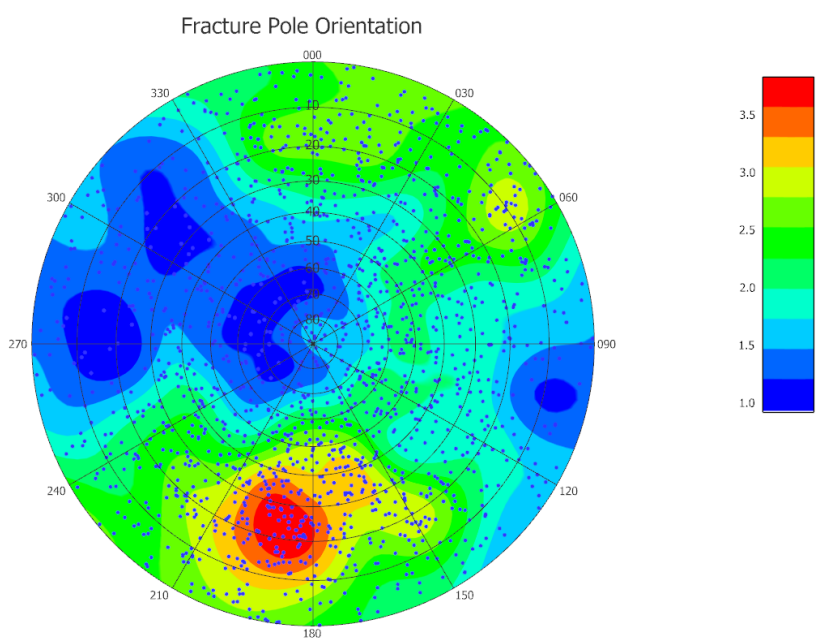

Figure 4.3: Lower hemisphere stereonet plot of fracture orientation mapped at apex level (Upper). Simulated fracture orientation in FracMan (Lower).

4.5 Fracture size distribution

Fracture size distribution was estimated from apex level drift mapping data. Drifts sizes and orientations and mapped fracture properties on the walls of drifts were simulated in FracMan. The procedure of estimating fracture size distribution is illustrated as following:

A region box (regionbox1) of the same size as the apex level was generated, firstly to represent drift area. The size of regionbox1 was 570m (west to east length) by 177m (north to south length) by 4.2m (height of the apex drifts). To account for potential boundary effects, another region box (regionbox 2), of a size of 580m x 187m x 14.2m was generated outside regionbox1, fractures were generated in regionbox2 and clipped by regionbox1.

Apex level drifts and mapped fractures were simulated in regionbox1, the drifts were generally oriented E10°N and south to east. As fractures were mapped on both walls of drifts, FracMan treated imported drift walls as "wells" (boreholes) and all fractures mapped in drift walls were along such "wells". Figure 4.4 shows the simulated drifts and fractures.

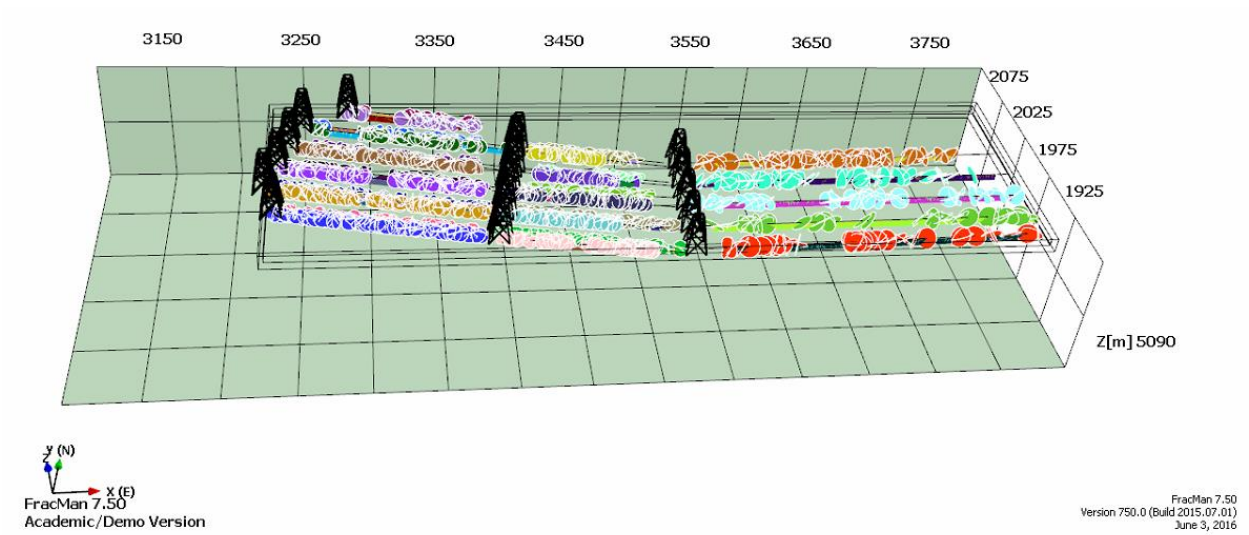

Figure 4.4: Simulation of drifts and mapped fractures in FracMan

To estimate a fracture size distribution, the input parameters, including fracture spatial model, fracture intensity and fracture orientation were determined as following:

- Enhanced-Baecher was chosen to be the fracture spatial model to generate randomly distributed fractures.
- For fracture orientation distribution, the mapped fracture orientation was employed, with the bootstrapping method used.
- For fracture intensity, an approach of estimating the P_{32} value using P_{21} values was employed. This procedure is illustrated in the following:

Eight of the drifts with different P_{21} values (low, medium, high values) were used to estimate the P_{32} value of mapped drifts area, the procedure of estimating fracture intensity of apex level is shown in Figure 4.5.

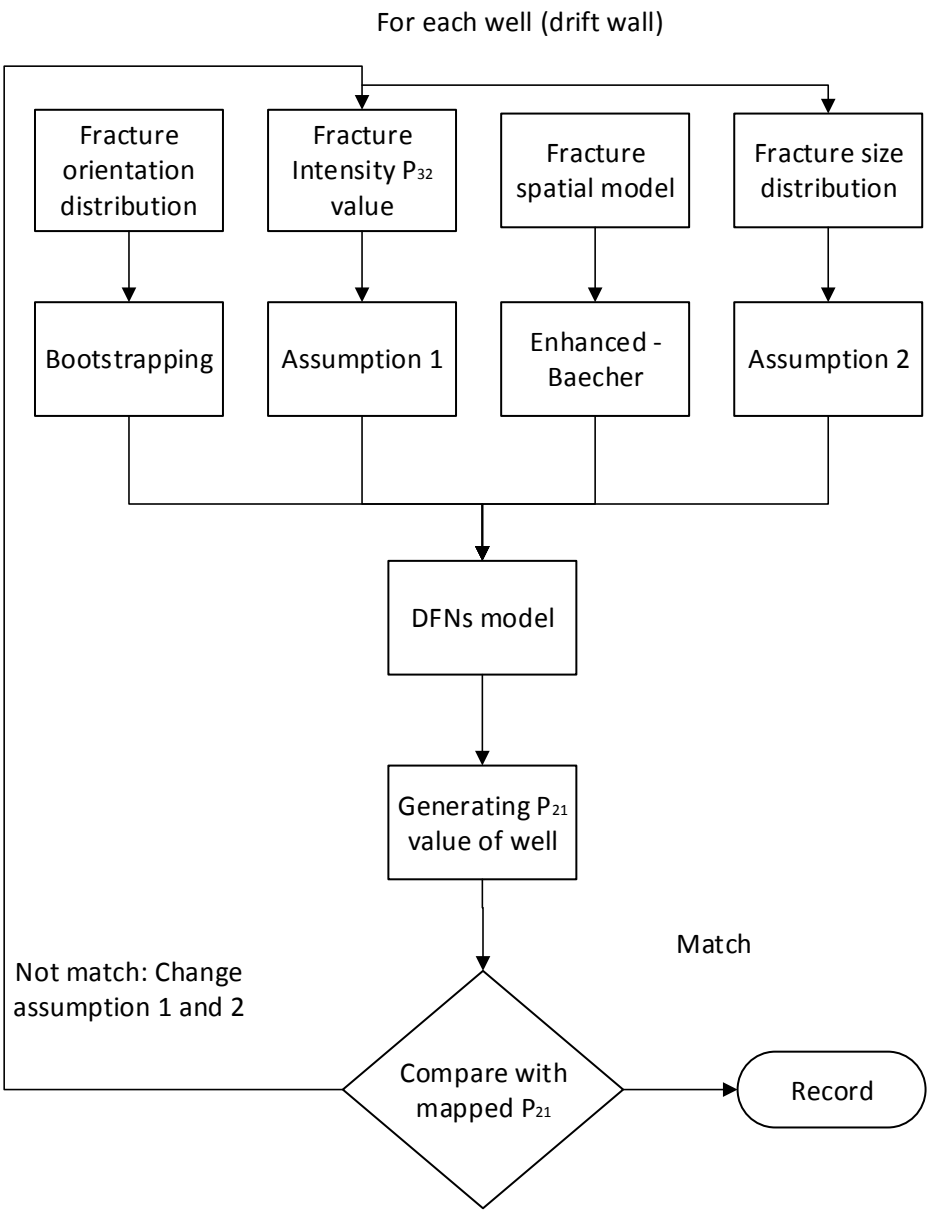

Figure 4.5: Schematic diagram of procedure for P_{32} determination

The P_{21} value for the eight drift walls are shown in Table 4.1 and the P_{32} and radius distribution results are shown in Table 4.2

ID	Area(m^2)	Trace length(m)	Calculated P_{21}(m^{-1})
ASD-1BNorth	536.23	59.90	0.11
ASD-1BSouth	538.00	98.00	0.18
ASD-1FNorth	885.59	273.45	0.31
ASD-1FSouth	695.20	129.48	0.19
ASD-2GNorth	580.24	100.90	0.17
ASD-2GSouth	1402.50	81.85	0.06
ASD-3ENorth	1352.43	87.05	0.06
ASD-3GNorth	536.23	59.90	0.11

Table 4.1: P_{21} values of nine mapped drifts and generated P_{32} values,

ID	P_{32} input(m^{-1})	Fracture size distribution input
ASD-1BNorth	0.35	Lognormal(2,2)
ASD-1BSouth	0.42	Lognormal(2,2)
ASD-1FNorth	0.60	Lognormal(2,2)
ASD-1FSouth	0.46	Lognormal(2,2)
ASD-2GNorth	0.40	Lognormal(1,1)
ASD-2GSouth	0.15	Lognormal(1,1)
ASD-3ENorth	0.15	Lognormal(1,1)
ASD-3GNorth	0.35	Lognormal(3,3)

Table 4.2: Appropriate P_{32} input and fracture size distribution input to obtain actual fracture length distribution for each drift wall.

According to Table 4.2, Logormal (1,1), Lognormal (2,2) and Lognormal (3,3) were considered as appropriate fracture radius distributions.

A simulation was conducted to define the most appropriate fracture size distribution:

The first step of the simulation was to define the linear relationship of P_{32} and P_{21} for each lognormal distribution. For P_{32} that equals to 0.5,1,2,3,4,5, a P_{21} value of all drifts was obtained, respectively. The results are shown in Table 4.3.

P_{32}	Lognormal(1,1)	Lognormal(2,2)	Lognormal(3,3)
0.5	0.38	0.38	0.35
1	0.75	0.76	0.72
2	1.54	1.54	1.5
3	2.28	2.28	2.1
4	3.04	3.01	3
5	3.76	3.77	3.5

Table 4.3: P_{21} values for three length distributions

Based on the information stated in Chapter 2, the linear relationship of P_{32} and P_{21} is defined by the equation:

$$P_{32} = C_{32} \times P_{21}$$

where, C_{32} is a constant. The linear relationship of P_{32} and P_{21} of Table 4.3 is shown in Figure 4.6.

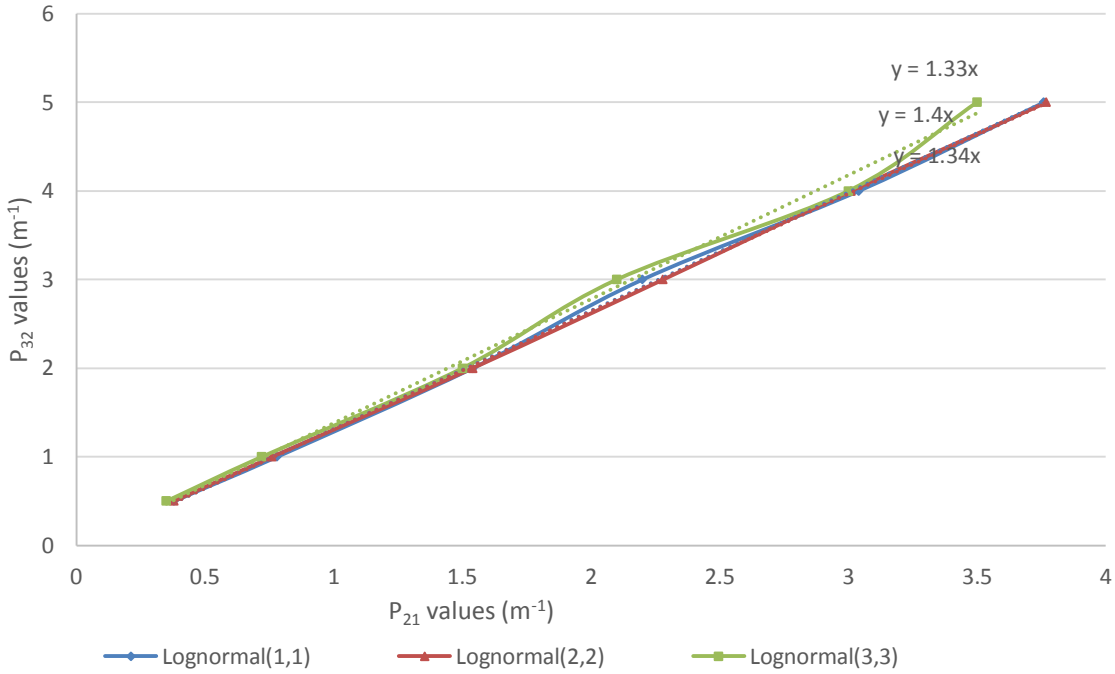

Figure 4.6: Linear relationship of P_{32} and P_{21} values.

The C_{32} values for Lognormal (1, 1), Lognormal (2, 2) and Lognormal (3, 3) are 1.33, 1.39 and 1.33, respectively. The linear relationship of the three lognormal distributions are similar to each other. This is probably because the length distributions do not have much variance. Thus, an average C_{32} value of 1.35 is applied to all length distributions.

Based on site mapping, the P_{21} value of all drifts was calculated to be 0.3, thus, P_{32} of all drifts was 0.3 ×1.35=4.1, which was chosen as an input for fracture size estimation. With the fracture intensity obtained, different fracture radius distributions were generated and the fracture length of all the drifts in the model was calculated to be compared with actual fracture length distribution.

Three fracture radius distributions - LogNormal (1, 1), LogNormal (2, 2) and LogNormal (3, 3) were generated and found to be appropriate. Figure 4.7 shows the curve of each distribution and the actual length distribution (cumulative plot).

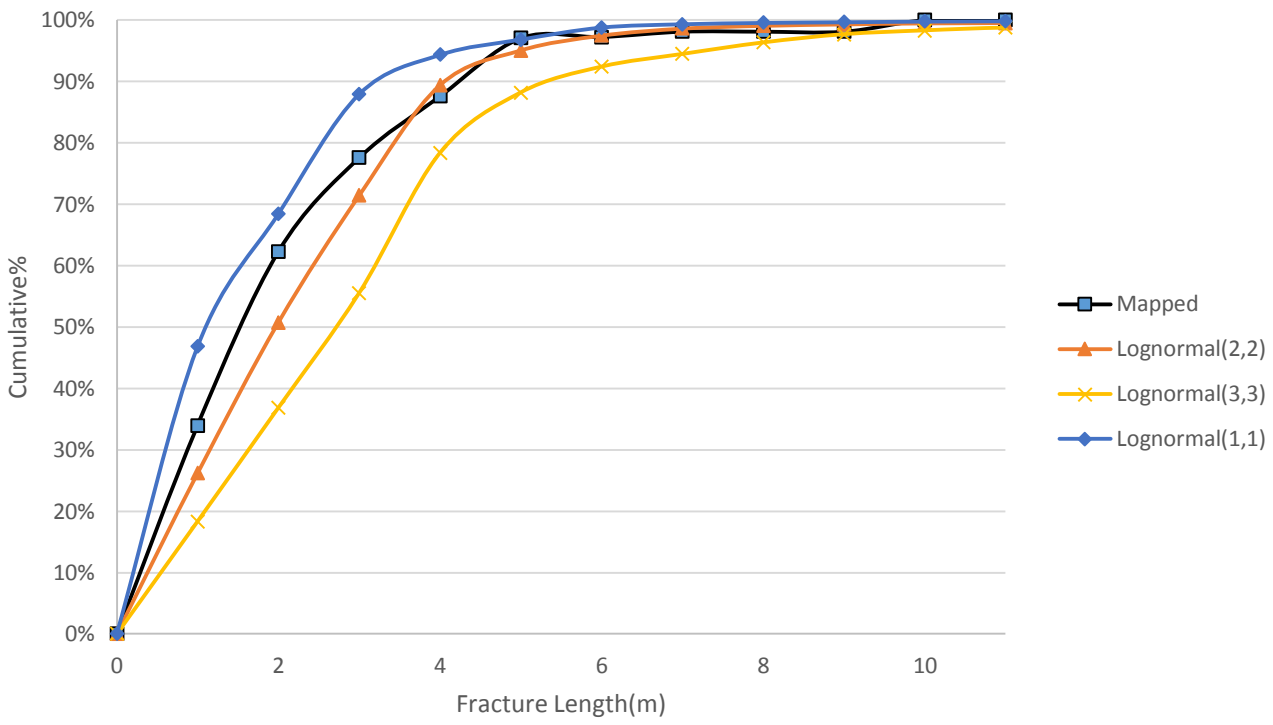

Figure 4.7: Curves of different LogNormal distribution and original data.

To quantitatively describe the difference of the fracture length distribution against the actual mapped data, the variances of the lognormal distributions were calculated, results are shown in Table 4.4.

	LogNormal(1,1)	**LogNormal(2,2)**	**LogNormal(3,3)**
Variance	296.7	244.3	541.2

Table 4.4: Variance values of different LogNormal distribution

According to Figure 4.7 and Table 4.4, LogNormal (2, 2) is recommended to be the fracture length distribution for the apex level and to be used for West Cave DFN model generation.

4.6 Fracture intensity

4.6.1 Problems of generating a P_{32} block model.

Previously, in Chapter 4, the following parameters were defined:

- Fracture spatial model - An Enhanced-Baecher model, was proposed to generate randomly distributed fractures.
- Fracture orientation distribution - This was decided to be obtained by bootstrapping the fracture orientation data mapped in the apex level.
- Fracture size distribution - It was proposed to use LogNormal (2,2) after analysing the exposures (the apex level drifts).
- Fracture intensity – The fracture frequency P_{10} values can be calculated using borehole data.
- Fracture termination - This is not applied in this chapter.

Figure 4.8 shows a schematic picture of the DFN model of West Cave based on these parameters and some main infrastructures (main drifts and faults).

In order to generate a P_{32} block model, FracMan requires that the source of fracture intensity and fracture orientation to be identical. In this case, fracture intensity was calculated from boreholes while fracture orientation was mapped from drift walls, thus caused difficulties to build a complete fracture network. In this chapter, an approach of estimating P_{32} values of blocks that near boreholes using C_{31} conversion process is introduced in Section 4.6.2.

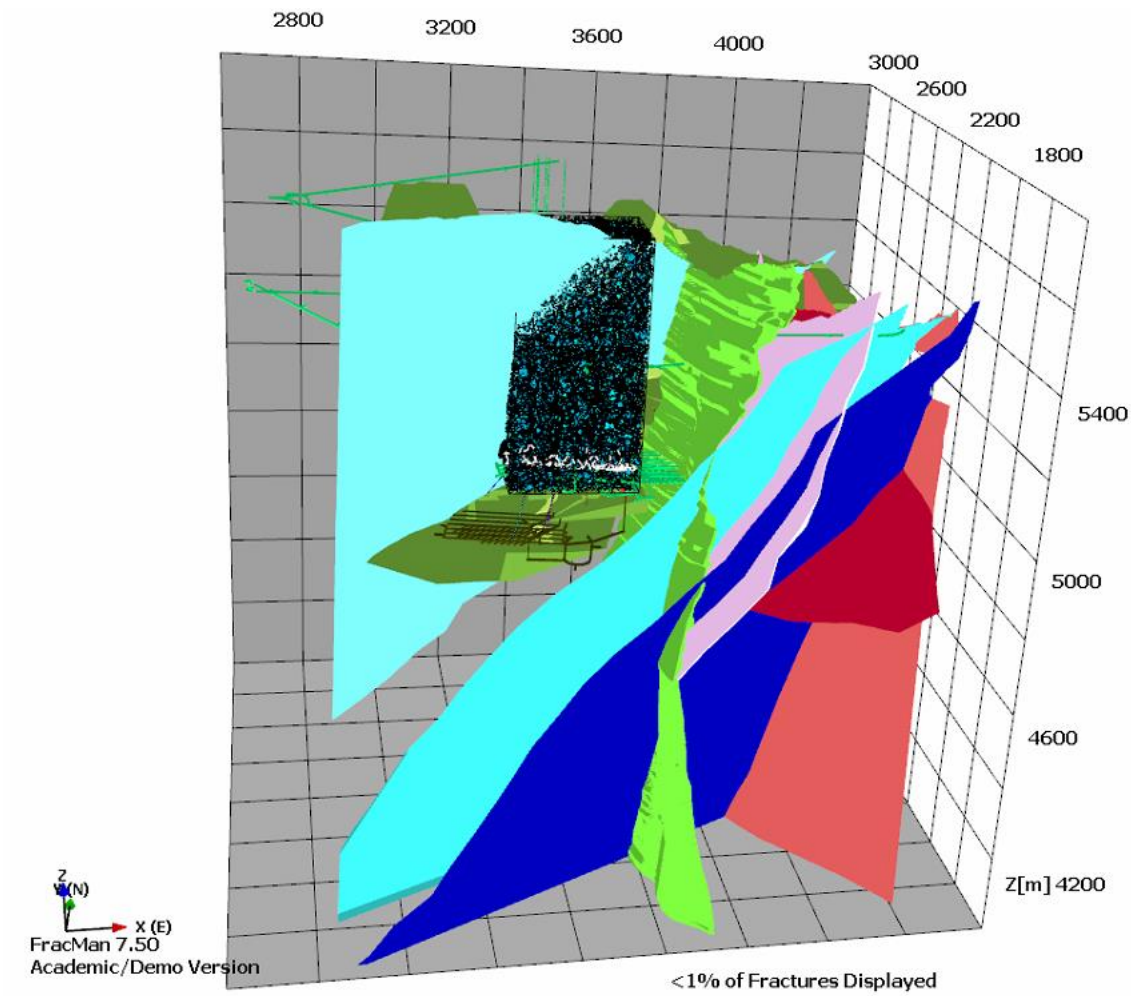

Figure 4.8: Schematic picture of a DFN model for New Afton West Cave.

4.6.2 Obtaining P_{32} values along boreholes

The goal of simulating a fracture block model is to obtain volumetric intensity P_{32} distribution of the generated fracture block and subsequently to calculate block size distribution. In the fracture model, P_{32} is expressed as a variable of other fracture properties. P_{10} values measured along the boreholes were used to generate the P_{32} block model using the relationship proposed by Wang, 2005:

$$P_{32} = C_{31} \times P_{10},$$

where, C_{31} is a constant and is related to fracture radius and orientation, as well as the orientation of sampling boreholes.

In linking in-situ fragmentation to secondary fragmentation, the boreholes that found to be close to significant faults indicated extreme P_{10} and led to extreme P_{32} values; thus boreholes near faults were not considered in this research. The boreholes that were employed in this chapter are shown in Table 4.5

Borehole ID	Dip (°)	Azimuth (°)
AF01-44	62.2	276
AF02-75	76	170
AF02-75	76	170
AF07-138	85	212
UA05-52	54	180
UA05-54	53	166
UA06-79	60	152
UA06-80	63.7	157.3

Table 4.5: Boreholes used for C_{31} conversion

The procedure of calculating C31 for the boreholes is illustrated in the following:

- All boreholes' dip and azimuth property were imported into FracMan, and the starting points of all boreholes were set to be (0, 0, 0). A regionbox1 of 50m x 50m x 50 was generated to be the region that fractures were to be generated. Another outerbox regionbox 2 of 100m × 100m ×100m was generated out of regionbox1 to account for boundary effects. The boreholes were initially set to be 50m long in regionbox1.

All the fracture parameters are defined following the previous discussion:

- Enhanced-Baecher model was chosen to be the spatial model to generate randomly distributed fractures
- Following the decision made in Section 4.5, fracture length distribution was defined to be LogNormal (2,2)
- Fracture orientation distribution was obtained by bootstrapping fracture dip/dip direction mapped at apex level.

- Fracture termination was not applied, as no fracture termination data was provided.

An example of the linear relationship of P_{32} and P_{10} for borehole AF01- 44 is shown in Figure 4.9.

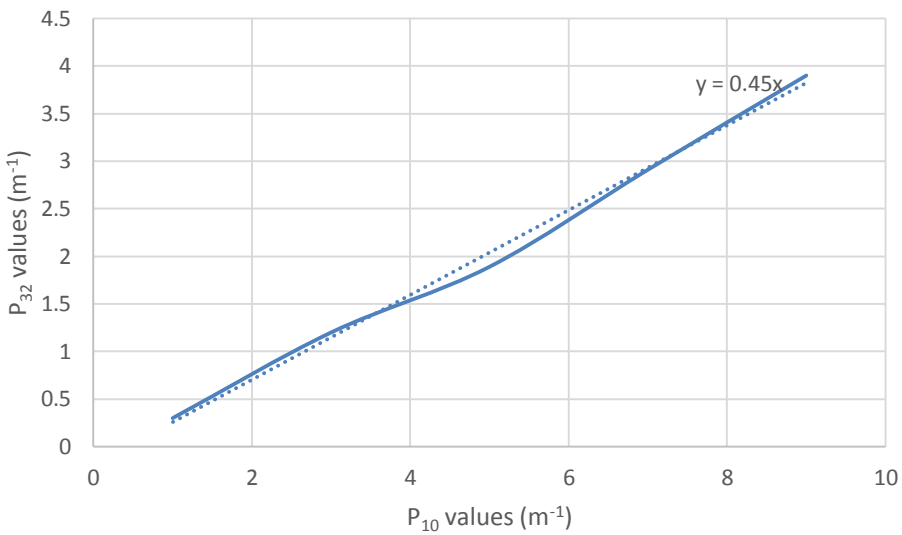

Figure 4.9: Linear relationship of P_{32} values and P_{10} values of borehole AF01-44

According to Figure 4.9, C_{31} value for borehole AF01 – 44 is 0.45. The C_{31} values for all the boreholes are shown in Table 4.6

Borehole ID	Dip(°)	Azimuth(°)	C_{31}
AF01-44	62.2	276	0.45
AF02-75	76	170	0.39
AF02-75	76	170	0.39
AF07-138	85	212	0.39
UA05-52	54	180	0.48
UA05-54	53	166	0.48
UA06-79	60	152	0.36
UA06-80	63.7	157.3	0.48

Table 4.6: C_{31} values of each borehole

4.7 Summary

This chapter has illustrated the choice of input parameters for the generation of a preliminary DFN model for New Afton West Cave, as summarised below:

- Enhanced-Baecher model was is employed to be the spatial model to generate randomly distributed fractures.
- Fracture length distribution is defined as lognormal distribution with a mean of 2 and a deviation of 2.
- Considering the large dispersion of fracture orientation distribution, it was is decided to use bootstrap orientation distribution mapped from the apex level.
- Due to the incomplete core log orientation data, fracture intensity P_{32} was calculated from borehole fracture frequency P_{10} values using a C31 conversion process with respect to eight boreholes in the West Cave zone.

Chapter 5: Investigation of the relationship between secondary fragmentation and in-situ fragmentation

5.1 Introduction

This chapter firstly introduced the effects of P_{32} on block sizes and calculated the weighted average P_{32} value of the New Afton West Cave. Subsequently, it explored the relationship between in-situ fragmentation and secondary fragmentation of the West Cave, specifically by comparing in-situ P_{80} and secondary fragmentation P_{80} of drawpoints.

5.2 Relationship between P_{32} values and block size distribution

Volumetric intensity P_{32} represents the total fracture area per unit volume. Larger values of P_{32} would generally represent a more blocky rock mass. Figure 5.1 shows examples of DFN models with increasing P_{10} (P_{32}) values.

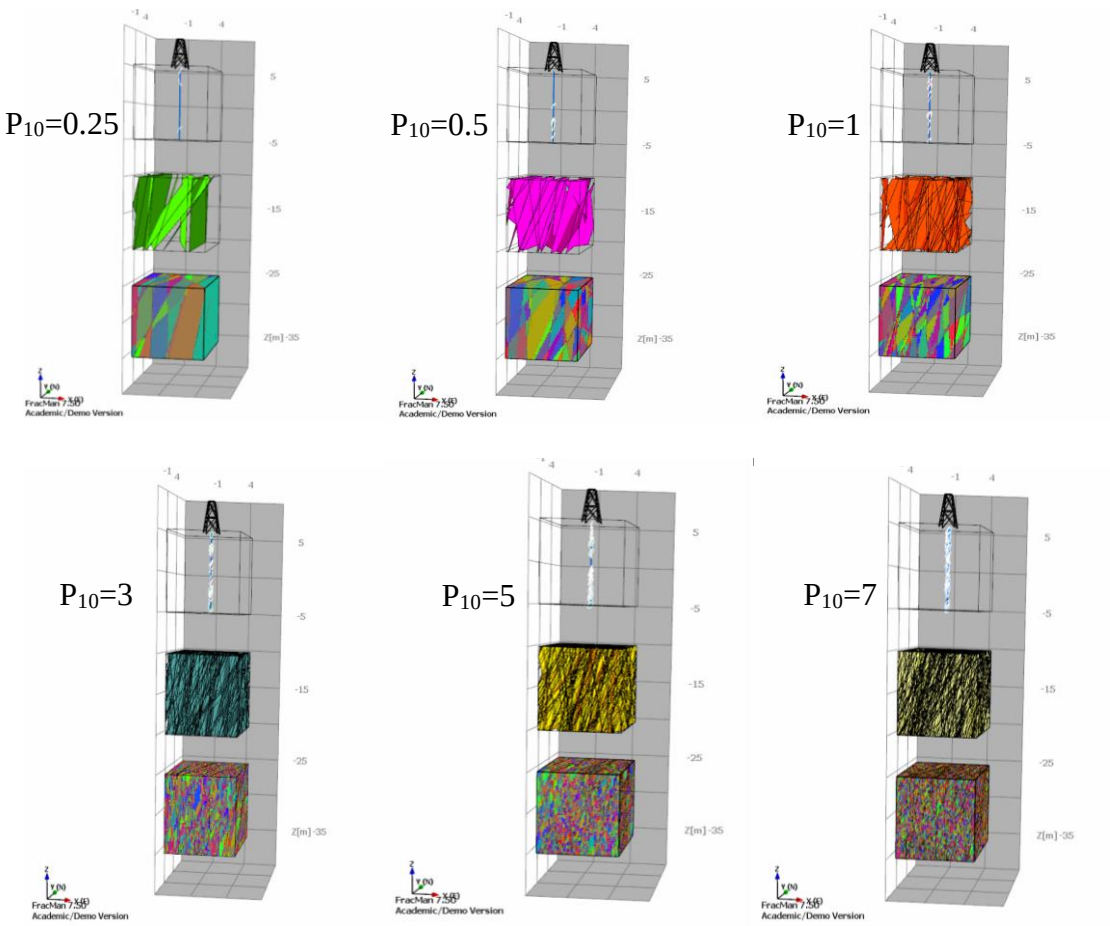

Figure 5.1: Different P_{32} values and corresponding P_{10} values in a vertical boreholes and block sizes, P_{10} equals to 0.25, 0.5, 1, 3, 5 and 7, respectively.

In order to define the relationship between P_{32} and in-situ block size distribution, DFN models with constant fracture orientation, length and variable P_{32} values (from 1 to 10) were generated. Fracture orientation distribution was defined, based on the mapped fracture orientation in the apex level at the New Afton mine, while the fracture length was assumed to be described by a lognormal distribution with a mean of 2 m and a standard deviation of 2 m (see Chapter 4).

A region box (named regionbox1) with dimensions of 10m x 10m x 10m was generated in FracMan for block size calculation. To account for boundary effects, an outer region (named regionbox2) of dimensions of 20m x 20m x 20m was generated to include regionbox1. Fractures were initially generated inside regionbox2 and then clipped to regionbox1.

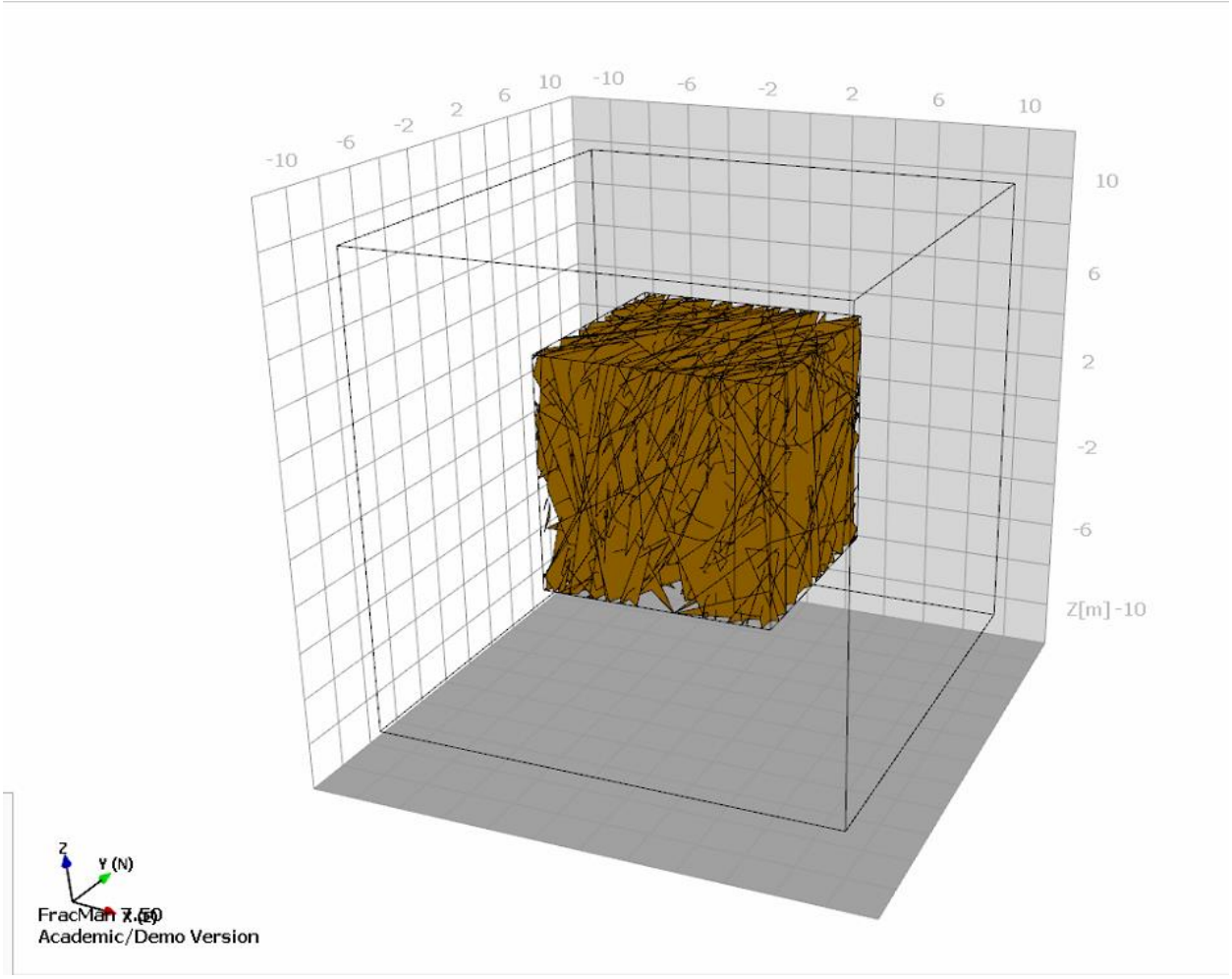

Figure 5.2: Schematic diagram of fractures generated in regionbox1.

In order to save computational time, models with P_{32} values of 1 to 5 include five realisations to account for the intrinsic stochastic variability of the models. For P_{32} of 6 to 7, three realizations were generated, while for P_{32} of 8 to 10, two realizations were generated. The P_{32} values

representing the weighted average volumetric intensity for the West Cave at New Afton were calculated as follows:

1. P_{32} values were calculated for every interval along the boreholes using the mapped P_{10} intensity and the calculated C_{31} coefficient (see Table 4.5 in Chapter 4).
2. The weight of each of the calculated P_{32} values was then derived and denoted here as W_i%.
3. The weighted average P_{32} was then calculated as:

   $P_{32} = \sum W_i \, P_{32i}$

   where, W_i is the weight (%) of a given P_{32} value.

The W_i values are shown in Table 5.1 below; accordingly, the weighted average P_{32} value is calculated to be 3.7.

P_{32} (m^{-1})	**Weight %**
1	5.29%
2	8.60%
3	28.57%
4	33.70%
5	19.67%
6	3.96%
7	0.20%
8	0.00%

Table 5.1: P_{32} values and corresponding weight along West Cave boreholes.

Using the implicit block search algorithm in FracMan, the fragmentation curves corresponding to P_{32} values of 1 to 10 were calculated. These are shown in Figures 5.3 to Figure 5.12. Those include the curves for each DFN realisation and the average curve for the assumed P_{32}. Finally, Figure 5.13 shows the average curve for all P_{32} models and the weighted average. Figure 5.3 to Figure 5.12 shows the PSD curves of each realisation (denoted as R1, R2….) and the average PSD curve for each P_{32} value. Note that FracMan allows a smallest cell size of 0.001 m^3, thus all the curves starts from 0.001 m^3.

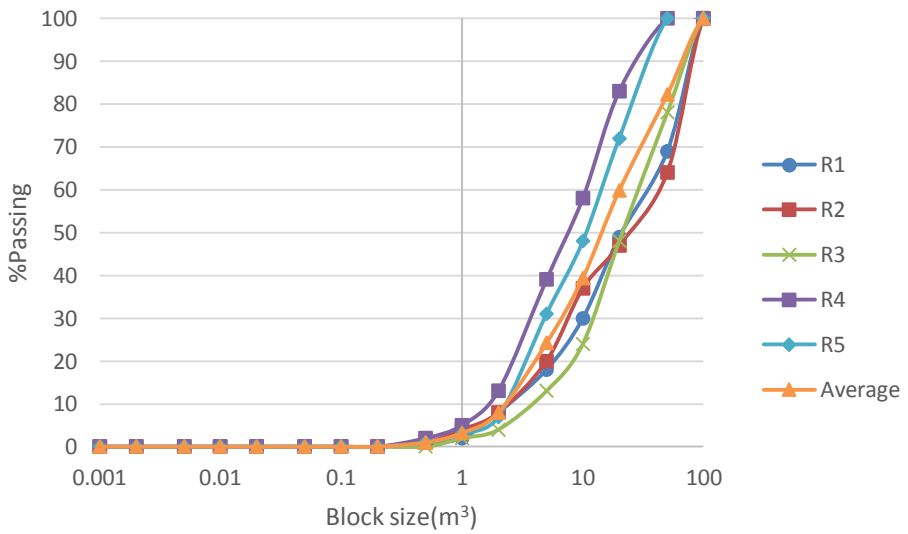

Figure 5.3: PSD curves for P_{32} equals to 1

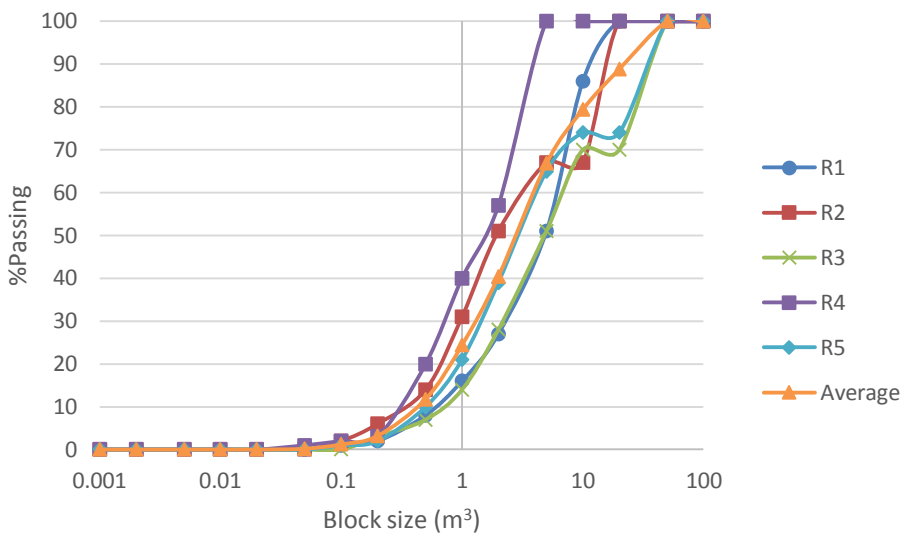

Figure 5.4: PSD curves for P_{32} equals to 2

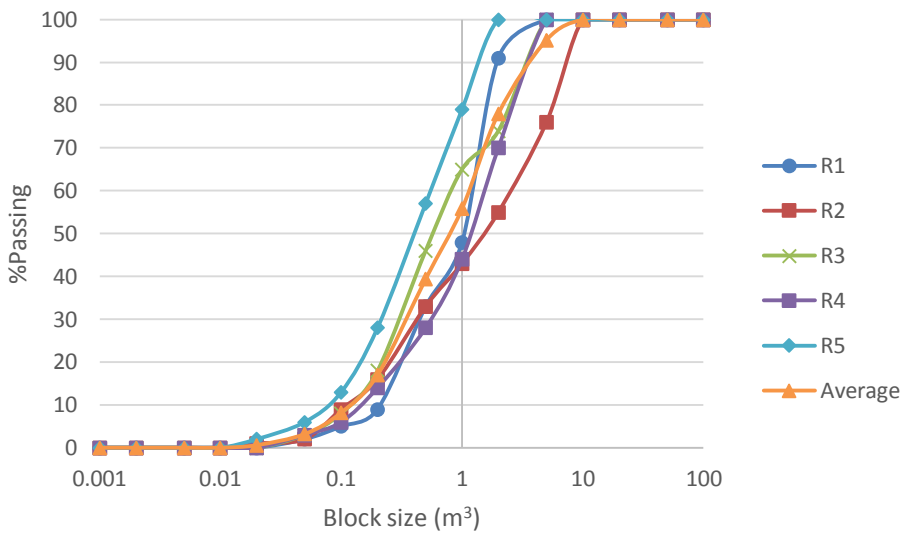

Figure 5.5: PSD curves for P_{32} equals to 3

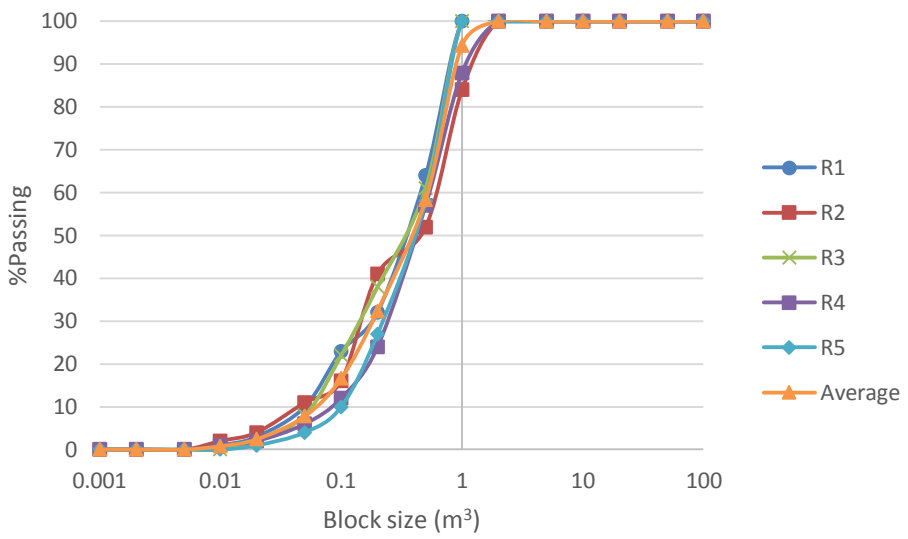

Figure 5.6: PSD curves for P_{32} equals to 4

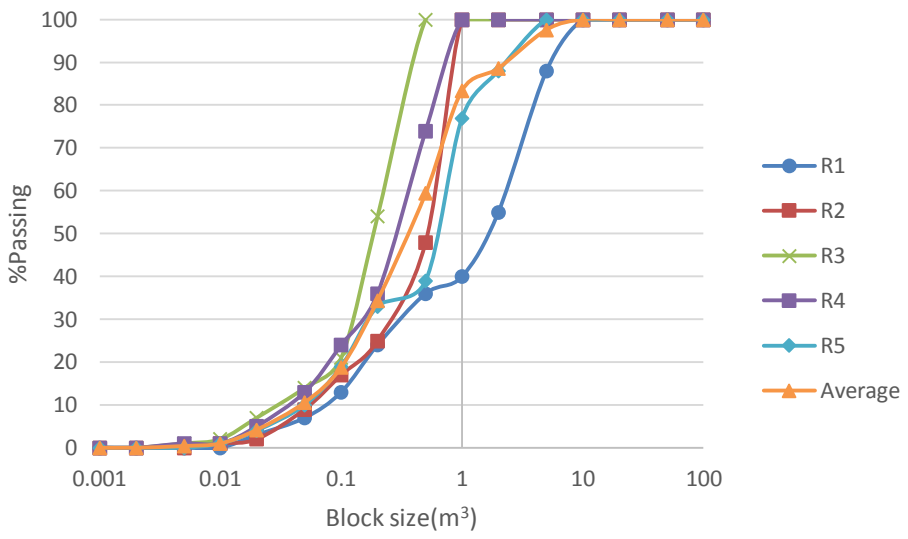

Figure 5.7: PSD curves for P_{32} equals to 5

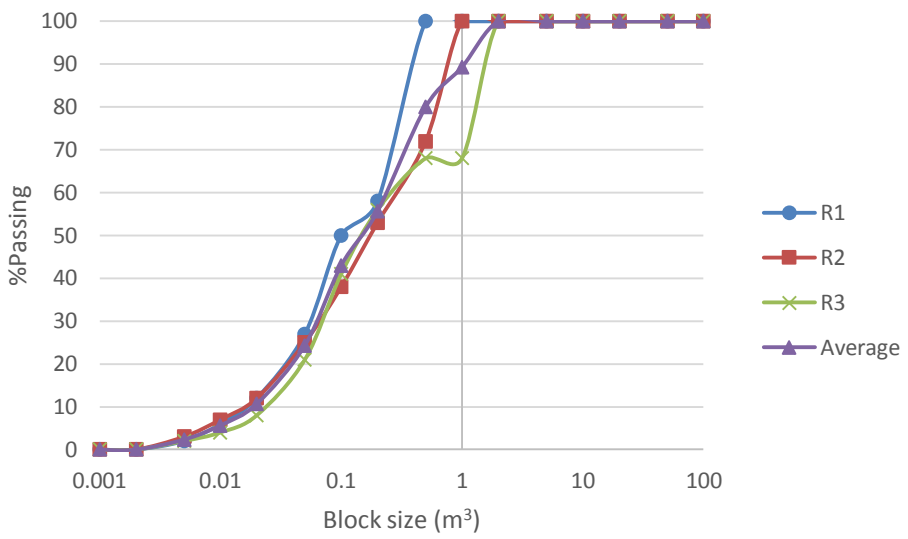

Figure 5.8: PSD curves for P_{32} equals to 6

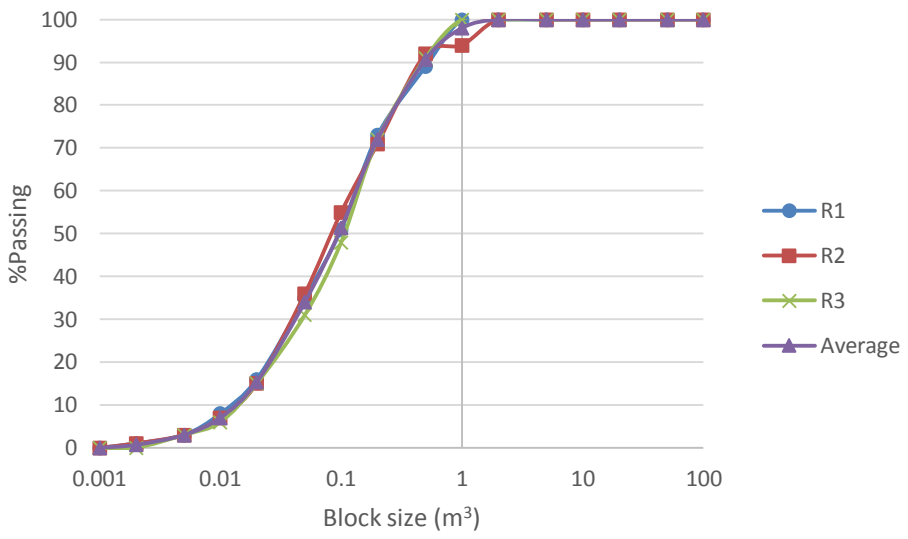

Figure 5.9: PSD curves for P_{32} equals to 7

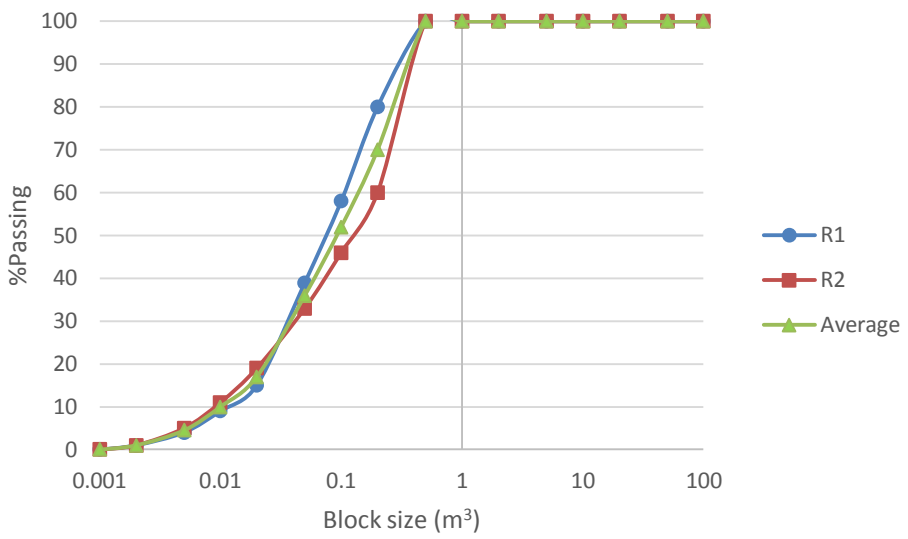

Figure 5.10: PSD curves for P_{32} equals to 8

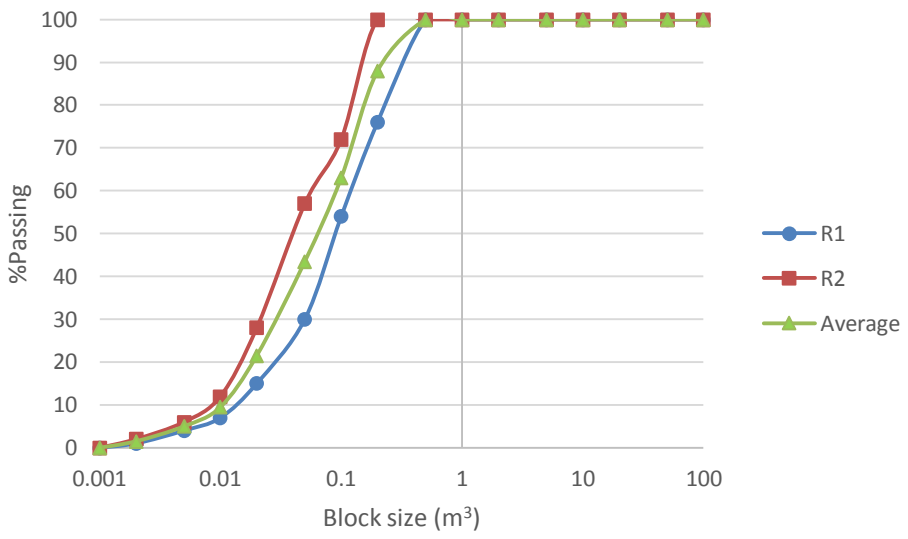

Figure 5.11: PSD curves for P_{32} equals to 9

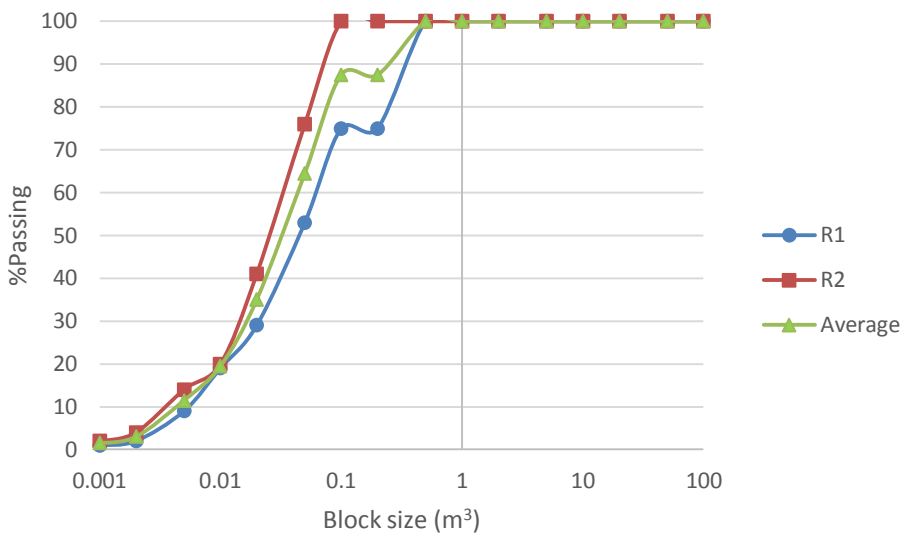

Figure 5.12: PSD curves for P_{32} equals to 10

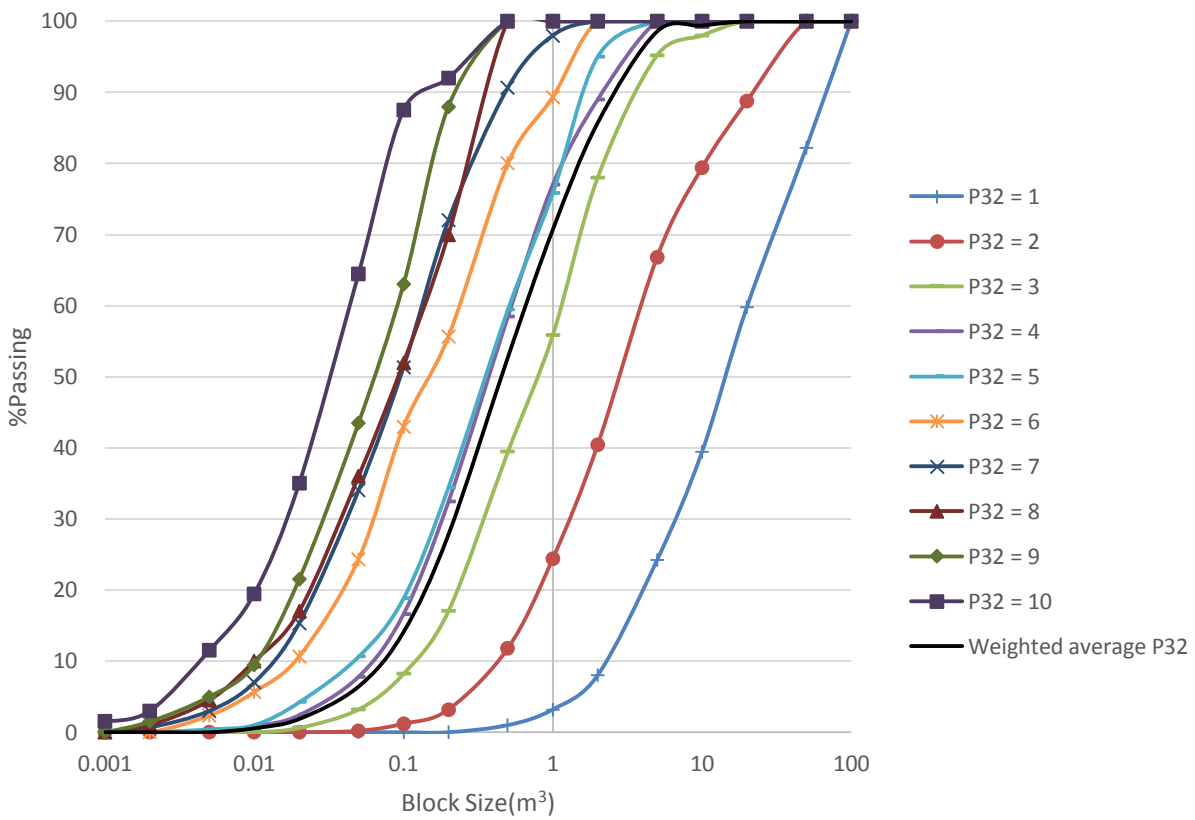

Figure 5.13: Block size analysis of P_{32} values from 1 to 10 and the weighted average P_{32} value (3.7)

5.3 Image processing of fragmentation at the New Afton mine

Chapter 3 illustrates the performance of two digital image processing tools - WipFrag and PotaMetrics, as well as their application, to estimate fragmentation size curves for broken material at the drawpoints of a block cave mine. Images were processed manually to limit the errors associated with edge detection functions. In total, 61 images were processed and the P_{80} passing % was estimated according to the generated PSD curves. According to visual observations following the site visit carried out in November, 2015, the secondary fragmentation material reporting at the drawpoints was found to be generally cubic in shape; accordingly, the size (in millimetres) for each rock fragment was defined using the following equation:

Particle size (mm) = $\sqrt[3]{Block\ size}$

Table 5.2 shows three groups of adjacent drawpoints' images that were used and subsequently compared in this chapter as well as their estimated secondary fragmentation P_{80} values (in mm).

Group	Drawpoint	Date	P_{80} of secondary fragmentation (mm)
A	B11S	2012, Nov 16	481
	B11S	2012, Dec 11	275
	B11S	2012, Oct 31	275
	B12S	2013, Nov 4	256
	B12S	2012, Dec 11	142
B	F10N	2013, Nov 4	350
	F10N	2012, Apr 19	293
	F10N	2012, Oct 31	278
	F10S	2012, June 27	269
	F8N	2013, Nov 4	430
C	C5S	2012, Feb 24	391
	C5S	2012, May 3	344
	C6S	2012, Dec 11	346
	C7S	2014, Mar 27	236.1
	C5S	2012, June 27	486
	C5S	2012, May 31	703
	C5S	2012, July 11	599
	C5S	2013, Nov 4	589

Table 5.2 Useful drawpoint images and corresponding P_{80} values

5.3.1 Relationship between secondary fragmentation and HOD

In a block cave mine, broken ore flows into the production level through the drawpoints. As the ore is removed, the force of gravity causes the ore above to continue to break and cave. This model

assumes a continuous flow of ore within columns connected to the drawpoints. However, the drawpoint materials may have not necessarily moved vertically down from within the ore body and reeling and mixing between adjacent ore columns is possible. The code PCBC (Dassault Systems, 2015) is employed in the current research for the purpose of relating the secondary fragmentation observed at the drawpoints to the in-situ conditions of the rock mass, by considering the vertical movement of the ore material and the Height of Draw (HOD) estimate based on the assumed production schedule. Note that the mixing model provided in PCBC considers materials moving along both vertical and horizontal directions, see Figure 5.14.

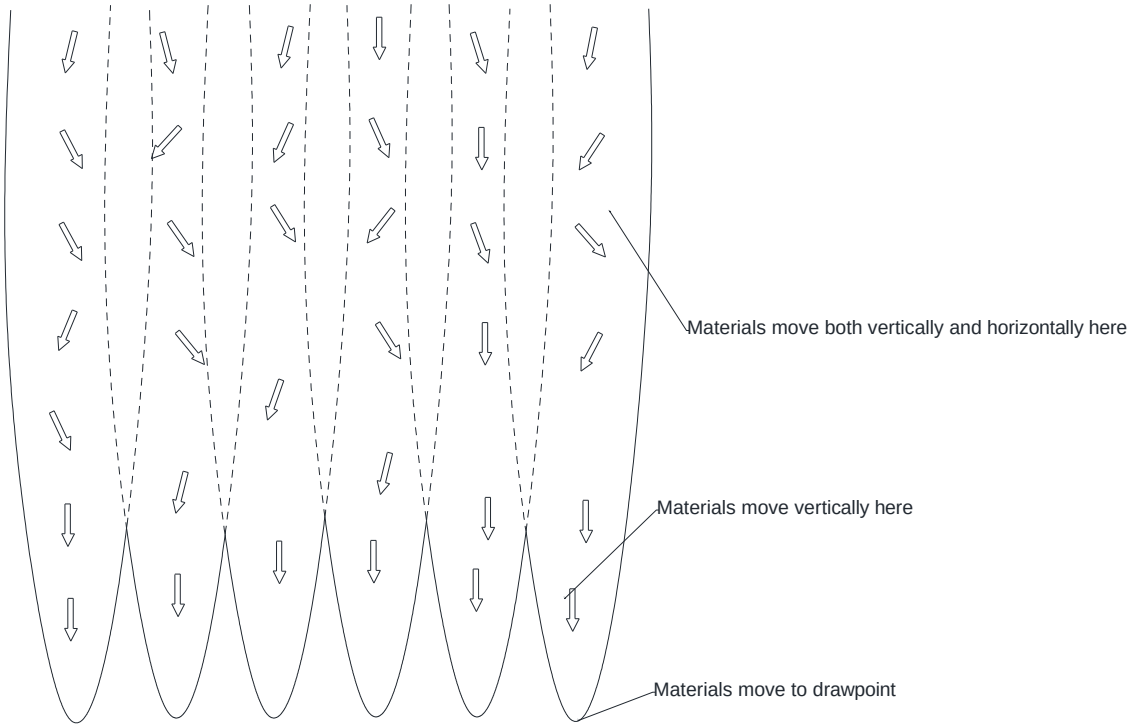

Figure 5.14: Diagram of materials' moving in PCBC modelling

The HOD property in PCBC's production schedule provides a method to estimate the original elevation from where the secondary broken material has potentially originated from. Table 5.3

shows a hypothetical example of a HOD sheet of a specific date in PCBC, the height of draw can be read from the sheet. For instance, the HOD of drawpoint B03 is 8m in this example.

HOD(m)	01	02	03	04	05	06	07
A	78	28	96	32			
B	85	70	8	79			
C	77	74	13	50	79	93	67
D	3	76	21	51	13	17	10
E	45	32	3	71	63	16	53
F					50	28	37
G					52	2	86

Table 5.3: An example of HOD sheet in PCBC

5.4 Linking in-situ fragmentation and secondary fragmentation

After the PSD curve of a particular drawpoint is obtained, it is possible to read the x, y coordinates from the drawpoint location; the z coordinate can be calculated using HOD data. The P_{80} values obtained from the DFN model (in-situ fragmentation) and from digital image processing (secondary fragmentation) are compared. Three groups of adjacent drawpoints (shown in Table 5.4) were analysed. Comparison results are shown in Figure 5.15, 5.16 and 5.17.

Group	Drawpoint	Date	Secondary P_{80} (mm)	DFN model P_{32} (m^2/m^3)	Estimated in-situ P_{80} (mm)
A	B11S	2012, Nov 16th	481	0.66	1,776
	B11S	2012, Dec 11th	275	0.66	1,776
	B11S	2012, Oct 31st	275	0.66	1,776
	B12S	2013, Nov 4th	256	0.62	1,694
	B12S	2012, Dec 11th	142	0.60	1,641
B	F10N	2013, Nov 4th	350	0.99	2,586
	F10N	2012, Apr 19th	293	0.72	1,927
	F10N	2012, Oct 31st	278	0.52	1,446
	F10S	2012, June 27th	269	0.69	1,852
	F8N	2013, Nov 4th	430	0.94	2,473
C	C5S	2012, Feb 24th	391	2.91	6,964
	C5S	2012, May 3rd	344	3.53	8,333
	C6S	2012, Dec 11th	346	3.69	8,667
	C7S	2014, Mar 27th	236.1	3.48	8,221
	C5S	2012, June 27th	486	4.58	10,559
	C5S	2012, May 31st	703	3.97	9,276
	C5S	2012, July 11th	599	4.68	10,777
	C5S	2013, Nov 4th	589	5.39	12,275

Table 5.4: P_{80} values of in-situ fragmentation and secondary fragmentation for the three analysed groups of drawpoints. Materials that came from nearby locations may have had the same borehole pass through, e.g. drawpoint B11S 2012 Dec 11th and 2012 Oct 31st share the same borehole.

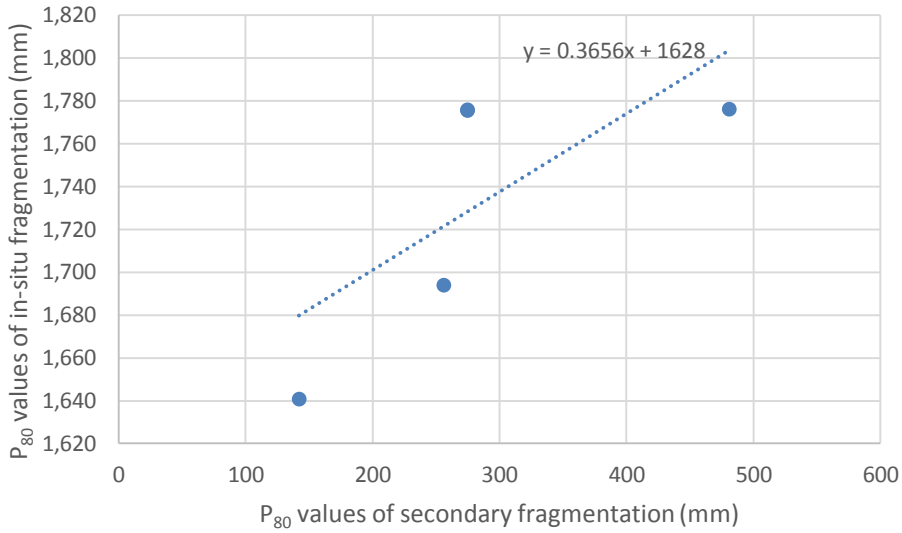

Figure 5.15 Group A: In-situ fragmentation P_{80} vs secondary fragmentation P_{80}.

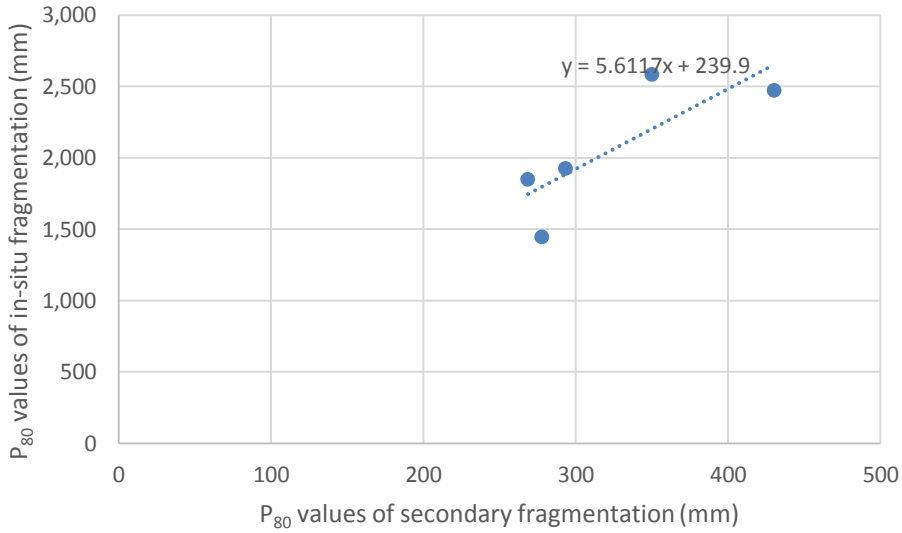

Figure 5.16 Group B: In-situ fragmentation P_{80} vs secondary fragmentation P_{80}.

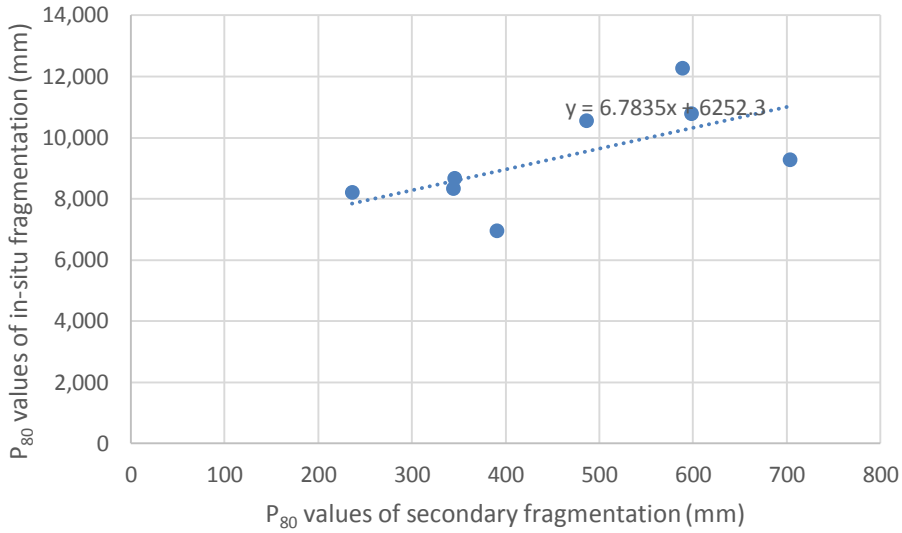

Figure 5.17: Group C: In-situ fragmentation P_{80} vs secondary fragmentation P_{80}.

According to Figure 5.14, 5.15 and 5.16, the equation of in-situ fragmentation and secondary fragmentation for Group A has a small multiplier (0.37). Group B and C have large multipliers (5.6 and 6.8, respectively), this indicates that for fragmentation in Group A's region, in situ fragmentation does not influence the size of secondary fragmentation very much while for Group B and C's region, in situ fragmentation plays a more important role. Group A has an addend of 1628, Group B has an addend of 239.9 while for Group C, the addend is 6252.3; this indicates that for different regions, the initial size of fragments (in-situ fragmentation) can be very different.

Because the relationship between in-situ fragmentation and secondary fragmentation is affected by a complex of factors such as rock types, fracture properties, ground stress, etc., the conclusion made should be based on analysing a large amount of data including, among others, such variables as different drawpoint locations, rock strength and fracture intensities.

5.5 Summary

This chapter introduced a procedure adopted for comparing measured secondary fragmentation P_{80} values to simulated in-situ fragmentation P_{80} values. A methodology for using PCBC to estimate the elevation of drawpoint materials was applied. Three groups of adjacent drawpoint images were analysed, the results indicated that for drawpoints of different location, the relationship of in-situ fragmentation and secondary fragmentation could be very different. To define such a relationship, more drawpoint images should be analysed. Moreover, other factors such as rock type and rock strength should be considered for future analysis.

Chapter 6: Conclusions and recommendations

6.1 Contributions

This thesis has introduced an approach that attempts to relate secondary fragmentation to in-situ fragmentation. Secondary fragmentation data were collected at the New Afton mine West Cave, and geotechnical data were used to generate a preliminary DFN based in-situ fragmentation model. The main contributions of this thesis are:

- Comparison of two image processing tools for fragmentation analysis, WipFrag and PortaMetrics. These techniques were initially tested using controlled laboratory conditions; the results indicated that both WipFrag and PortaMetrics would provide reliable results in good agreement with the physical data. However, both techniques had some limitations when applied to actual field conditions. It was found that these effects could be minimised by using a manual processing approach to obtain the PSD of every drawpoint.
- A preliminary DFN model was generated using fracture data collected along both boreholes and drift mapping. Using an implicit block search algorithm, size distribution curves representing the in-situ fragmentation of the West Cave at New Afton were generated for a range of volumetric intensity values in the range of 1 to 10.
- In-situ fragmentation curves were compared to secondary fragmentation curves using the P_{80} % passing as reference value. Three sets of adjacent drawpoints were used for comparison purposes.

6.2 Deviation analysis

Deviation mostly occured with secondary fragmentation measurement and in-situ fragmentation simulation, illustrated as follows:

- The surface of drawpoints was measured by WipFrag, though manual processing was applied, the rocks hidden by the surface were not considered. Another challenge faced the performance of image processing was lightness, it was anticipated that with good lighting equipment, the accuracy of image processing should be improved.
- The quality of input data could significantly affect the quality of simulated DFN model. In this research, only apex level mapping provided information for fracture orientation distribution. This distribution might not have represented the orientation distribution of the whole cave. Deviation caused by this issue might significantly affect the quality of DFN model, thus affect such further results as P_{32} values and rock size distribution.
- For current stage of the research, only P_{10} values along boreholes (P_{10} values that can be directly calculated from borehole data) were employed to estimate P_{32} values, thus the P_{32} values without boreholes passing through were not considered.

6.3 Recommendations

As an ongoing research project conducted at UBC Mining, further study can be done with respect to:

- The measurement of secondary fragmentation. Current digital image processing has two main disadvantages: i) 2D digital image processing can only capture the rocks of the drawpoint surface, thus materials behind the surface are invisible, which can greatly cause measure deviation especially when huge rocks are hidden. ii) Since manual processing takes a significant amount of time to obtain the PSD of drawpoints, it is believed that optimising underground lighting conditions can improve the accuracy of automatic processing, which will greatly improve the efficiency of image processing.

- As discussed in the previous section, DFN modelling relies heavily on the quality of input data. The only fracture orientation data available in this research were from apex level mapping, the fracture orientation of other elevations was still missing. The current approach of calculating P_{10} values along boreholes and then converting to P_{32} values is only effective with areas close to boreholes, P_{32} of blocks that are far away to a borehole were not calculated in this research, which greatly limits the amount of data that can be analysed. It is suggested that further study be focused on seeking fracture orientation data from different depths to improve the DFN model.
- This research considered only the fracture network and particle size distribution. However, for different types of rocks, their possibility to be broken during fragmentation process can be very different. It is recommended that secondary fragmentation should also be influenced by rock strength. Further study should consider rock strength indices such as PLI and UCS.
- In this research, only P_{32} values of analysed images were obtained. It is recommended to calculate all P_{32} values of the whole cave and import the P_{32} block into PCBC to generate a production schedule of P_{32} values. This would be a more straightforward way to obtain P_{32} values of certain drawpoint materials, schematically shown in Figure 6.1

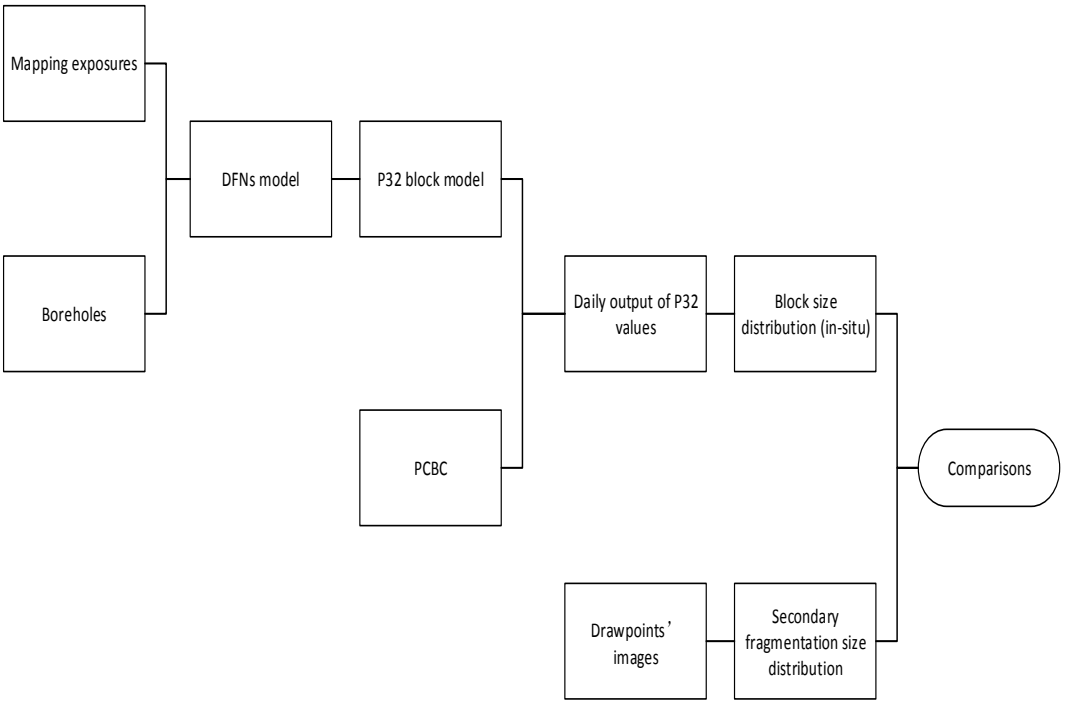

Figure 6.1: Schematically diagram of using DFN and PCBC to compare in-situ fragmentation and secondary fragmentation

- This research was done at New Afton West Cave, the geological survey indicates that New Afton East Cave has more fault structures. The study of the East Cave would provide an opportunity to assess this approach applied to a more fractured ore body.
- The PSD curve obtained by using the weighted average P_{32} value calculated in Section 5.2 is considered to be representative of size distribution in the West Cave region. Once the secondary fragmentation of the whole cave could potentially be obtained (this could be accomplished by analysing a large amount of drawpoint images), it should be possible to compare the weighted average PSD curve to the overall secondary fragmentation curve.
- This research is considered to be a part of the Cave-to-Mill research conducted at UBC Mining. The results of this research shall feed into the Cave-to-Mill approach to estimate the output of mills at the New Afton mine.

References

Bhandari, S., & Tanwar, D. (1993). Production of large sized fragmentation with pre-fixed size distribution. *Proc. 4th Int. Symp. Rock Frag by Blasting*, (pp. 369-376). Vienna.

Brown, E. (2005). *De Beers short course on block caving mechanics.* University of Queensland and Golder Associates.

Brown, E. T. (2003). *Block Caving Geomechanics.* Julius Kruttschnitt Mineral Research Centre, Brisbane, Australia.

Carlsson, O., & Nyberg, L. (1983). A Method for Estimation of Fragment Size Distribution with Automatic Image Processing. *1st International Symposium on Rock Fragmentation by Blasting*, *1*, pp. 333-345.

Dershowitz, W., & Einstein, H. (1988, January). Characterizing Rock Joint Geometry with Joint System Model. *Rock Mechanics and Rock Engineering, 21*, pp. 21-51.

Dershowitz, W., & Herda, H. (1992). Interpretation of Fracture Spacing and Intensity. *32nd U.S. Rock Mechanics Symposium.* Santa Fe, New Mexico.

Dershowitz, W., La Pointe, P., & Cladouhos, , T. (1998). Derivation of Fracture Spatial Pattern Parameters from Borehole Data. *International Journal of Rock Mechanics and Mining Sciences, 4/5*, p. 508.

Dassault Systems. (2015). Retrieved May 2016, from http://www.geovia.com/products/pcbc.

Elmo , D., Rogers , S., & Beddoes, R. (2011). Numerical analysis of caving mechanism using a hybrid FEM/DEM approach: experience gained and lessons learned. *Proc. 45th US Rock Mechanics Symposium.* San Francisco.

Elmo, D. (2006). Evaluation of a hybrid FEM/DEM approach for determination of rock mass strength using a combination of discontinuity mapping and fracture mechanics modelling,

with particular emphasis on modelling of jointed pillars (Doctoral dissertation). *Retrieved from EThOS database(http://ethos.bl.uk/OrderDetails.do?uin=uk.bl.ethos.439831).*

Elmo, D., Liu, Y., & Rogers, S. (2014). Principles of Discrete Fracture Networks for Geotechnical applications. Proc of the *1st Discrete Fracture Networks Engineering.* Vancouver, B.C., Canada.

Elmo, D., Rogers, S., & Kennard, D. (2009). Characterisation of natural fragmentation using a discrete fracture network approach and implications for current rock mass classification system. *43rd U.S. Rock Mechanics Symposium.* Southampton

Elmo, D., Rogers, S., Stead, S., & Eberhardt, E. (2014). Discrete fracture network approach to characterise rock mass fragmentation and implications for geomechanical upscaling. *Mining Technology, 123*(3), pp. 149-161.

Elmo, D., Schlotfeldt, P., Beddoes , R., & Roberts, D. (2011). Numerical simulations of scale effects under varying loading conditions for naturally fractured rock masses and implications for rock for rock mass strength characterization and the design of overhanging rock slopes. *Proc. 45th US Rock Mechanics Symposium.* San Francisco.

Elmo, D., Vyazmensky, A., Stead, D., & Rance, J. (2008). Numerical analysis of pit wall deformation induced by block-caving mining: a combined FEM/DEM-DFN synthetic rock mass approach. *In Proceedings of the 5th conference and exhibition on mass mining*, (p. 10). Lulea, Sweden.

FracMan. (2014). Retrieved May 2016, from http://www.fracman.com/home/software/fracman-version-history/software-fracman-7-4/

Gao, L., Yan, Y., Lu, G., & Carter, M. R. (2012, October). On-line measurement of particle size and shape distribution of pneumatically conveyed particles through multi-wavelength based digital imaging. *Flow Measurement and Instrumentation, 27*, pp. 20-28.

Golder. (2014). Retrieved May 2016, from *http://www.golder.com/*.

Grant, G. R., & Dutton, A. J. (1983). Development of a fragmentation monitoring system for evaluating open slope blast performance at Mount Isa Mines. *Proc . 1st Int. Symposium on Rock Fragmentation by Blasting*, (pp. 637-652).

Han, J.-H., & Song, J.-J. (2016, February). Block delineation algorithm for rock fragmentation analysis . *International Journal of Rock Mechanics and Mining Sciences, 82*, 48-60.

Harmrin, H. (1982). Underground mining methods and applications. In A. W. Hustrulid, & L. R. Bullock, *Underground Mining Method: Engineering Fundamentals and International Case Studies* (pp. 3-14). Littleton, Colorado: the Society for Mining, Metallurgy and Exploration Inc.

Hunter, G. C., Mc Dermott, C., Miles , N. J., Singh, A., & Scoble, M. J. (1990). A review of image analysis techniques for measuring blast fragmentation. *Mining Science and Technology, 11(1)*, pp. 19-36. doi:10.1016/0167-9031(90)80003-y

Kemeny, J., Devgan, A., Hagaman, R., & Wu, X. (1993, July 1). Analysis of Rock Fragmentation Using Digital Image Processing. *Journal of Geotechnical Engineering, 7*, pp. 1144-1160.

Ko, Y.-D., & Shang, H. (2011, October). A neural network-based soft sensor for particle size distribution using image analysis. *Powder Technology, 212*(2), 359-366.

Laubscher, D. H. (1990). A geomechanics classification system for rating of rock mass in mine design. *Journal of the South African Institute of Mining and Metallurgy, 10*(0038-223X), pp. 257–273.

Laubscher, D. H. (1994, October). Cave mining - the state of the art. *The Journal of The South African Institute of Mining and Metallurgy*, pp. 279-293.

Laubscher, D. H., & Jakubec, J. (2001). The MRMR rock mass classification for jointed rock masses. *Underground Mining Methods: Engineering Fundamentals and International Case Studies* (pp. 475–481). Littleton, Colorado, USA: Society for Mining, Metallurgy, and Exploration (SME).

Maerz, H., & Zhou, W. (1999). Calibration of Optical Digital Fragmentation Measuring Systems. *6th International Symposium for Rock Fragmentation by Blasting.* Johannesburg, South Africa.

Maerz, N. H. (1996). Reconstructing 3-D block size distribution from 2-D measurements on sections. *Fragblast 5 Workshop on Measurement of Blasting Fragmentation.* Montreal, Quebec, Canada.

Maerz, N. H. (1998). Aggregate sizing and shape determination using digital image processing. *Aggregates Research (ICAR) Sixth Annual Symposium Proceedings*, (pp. 195-203). St. Louis, Missouri.

Mauldon, M. (1998, Novermber). Estimating Mean Fracture Trace Length and Density from Observations in Convex Windows. *Roch Mechanics and Rock Engineering, 31*, pp. 201-216.

MotionMetrics. (2015). Retrieved May 2016, from http://www.motionmetrics.com/portable/.

Nightsearcher. (2015). Retrieved May 2016, from http://www.nightsearcher.co.uk/.

Rocscience. (2015). Retrieved May 2016, from https://www.rocscience.com/rocscience/products/dips.

Rogers, S., Kennard, D., Dershowitz, W., & As, A. (2007). Characterising the in situ fragmentation of a fractured rock mass using a discrete fracture network approach. Proceedings of the 1st Canada-US Rock Mechanics Symposium, Vancouver, Canada, 27–31 May 2007 Rock Mechanics: Meeting Society's Challenges and Demands, 137-143. doi:10.1201/noe0415444019-c18

Rogers, S., Elmo, D., Beddoes, R., & Dershowitz, W. (2009). Mine Scale DFN Modelling and Rapid Upscaling in Geomechanical Simulations of Large Open Pits. *International Conference on Large Open Pits.* Santiago, Chile.

Rogers, S., Elmo, D., Webb, D., & Catalan, A. (2010). A discrete fracture network based approach to defining in situ, primary and secondary fragmentation distributions for the Cadia East panel cave project. *The second international seminar on block and sublevel caving*, (pp. 425-440). Perth, Australia.

Rogers, S., Elmo, D., Webb, G., & Catalan, A. (2014, April 29). Volumetric fracture intensity measurement for improved rock mass characterisation and fragmentation assessment in block caving operations. *Rock Mech & Rock Eng*.

Sainsbury, B. (2010). Sensitivities in the numerical assessment of cave propagation. *2010 Australian Centre for Geomechanics.* Perth.

Sainsbury, B., Pierce, M., & Mas Ivars, D. (2008). Analysis of Caving Behaviour Using a Synthetic Rock Mass Ubiquitous Joint Rock Mass Modelling Technique. *2008 Australian Centre for Geomechanics.* Perth.

Schleifer, J., & Tessier, B. (1996). FRAGSCAN: A tool to measure fragmentation of blasted rock. *Proceedings of the FRAGBLAST 5 Workshop on Measurement of Blast Fragmentation*, (pp. 73-78). Montreal, Quebec, Canada.

Schorsch, S., Vetter, T., & Mazzotti, M. (2012, July 30). Measuring multidimensional particle sizd distribution during crystallization. *Chemical Engineering Science, 77*, pp. 130-142.

Scott Wilson Mining. (2009). Technical Report on The New Afton Project, British Columbia, Canada., (p. 19). Retrieved April 2016, from http://s1.q4cdn.com/240714812/files/documents_properties/new_afton/New_Afton_NI_43-101_Technical_Report_FINAL_Feb19.pdf

Staub , I., Fredriksson , A., & Outters , N. (2002). Strategy for a Rock Mechanics Site Descriptive. *Development and testing of the theoretical approach.* Svensk Kärnbränslehantering AB.

Tollenaar, R. N. (2008). Characterization of Discrete Fracture Networks And Their Influence on Caveability And Fragmentation (T), University of British Columbia. R*etrieved from https://open.library.ubc.ca/cIRcle/collections/24/items/1.0067206 (Original work published 2008)*.

Wang, X. (2005). Stereological Interpretation of Rock Fracture Traces on Borehole Walls and Other Cylindrical Surfaces (Doctoral Dissertation) . *Retrived from https://theses.lib.vt.edu/theses/available/etd-09262005-164731/unrestricted/Dissertation_Xiaohai_Wang.pdf.*

WipFrag Sampling and Analysis Guide. (2014). Retrieved May 2016, from http://www.wipware.com/.

WipWare. (2014). Retrieved April 2016, from http://www.wipware.com.

Zhang, L., & Einstein, H. (1998, November). Estimating the Mean Trace Length of Rock Discontinuities. *Roch Mechanics and Rock Engineering, 31*, pp. 217-235.

Zhang, L., & Einstein, H. (2000, July). Estimating the Intensity of Rock Discontinuities. *International Journal of Rock Mechanics and Mining Sciences, 37*, pp. 819-837.